Near-surface temperature changes in the Denmark Strait over a Dansgaard-Oeschger cycle

By

Snorre Birkelund Wille

MASTER THESIS IN QUATERNARY GEOLOGY AND PALEOCLIMATE

Department of Earth Science

University of Bergen

November 2018

Abstract

The Greenland ice core record shows large and abrupt temperature increases that interrupted the cold climate of the last glacial period. These events, known as Dansgaard-Oeschger (D-O) events have been linked with climate records from North Atlantic and Nordic Seas sediments. Mechanisms determining the timing and amplitude of the Greenland temperature signal are thought to comprise variations in oceanic heat transport resulting from freshwater perturbations and variations in the Nordic Seas sea ice extent. While most studies on the near-surface Nordic Seas role in D-O events have been conducted in the south-eastern part of the Nordic Seas, I here present the first near-surface Mg/Ca temperature record over D-O events from the Denmark Strait. The record is coupled with $\delta^{18}O$ and $\delta^{13}C$ records obtained from the shells of the planktonic foraminiferal species *Neogloboquadrina pachyderma* and covers the interval Greenland Interglacial 9 (GI9) to Greenland Interglacial 8 (GI8) with 30-year temporal resolution.

Two different cleaning protocols were applied prior to Mg/Ca measurement: the “Cd-cleaning” method and the “full-cleaning” method. Ratios of Al/Ca and other elemental ratios of potential contaminants decrease to some extent after the “full-cleaning” method compared with the “Cd-cleaning” method, yet the different cleaning methods yield similar results in terms of Mg/Ca. Mg/Ca reconstructed temperatures are largely in agreement with temperature reconstructions in the south-east Nordic Seas indicating that planktonic Mg/Ca temperature reconstruction is feasible during the last glacial period in the Denmark Strait.

Subsurface waters were relatively warm during Heinrich Stadial 4 (HS4) with temperatures at ~4-5°C while $\delta^{18}O_{sw}$ and $\delta^{13}C$ were low. Together, this suggests that the subsurface waters were covered by a lid of fresher surface water and sea ice. Over the transition to GI8, temperatures dropped by ~3°C, $\delta^{18}O_{sw}$ increased by ~1‰, and $\delta^{13}C$ increased by ~0.3‰ indicating a reorganization of the upper water column. The transition took place over centuries, which is slower than expected for this particular site. The site is therefore not likely to be directly involved in the abrupt heat release and sea ice diminution that is thought to cause decade-scale warming on Greenland. Temperature variations with increasing amplitude through GI8 are observed in the record, indicating an instable halocline and variations in local ventilation.

Acknowledgments

I would like to thank my supervisor Eystein Jansen for his advice and guidance though this process. I am grateful to my co-supervisor Amandine A. Tisserand for her patience in TELab and for going to lengths to assist my work, and to my co-supervisor Evangeline Sessford for her help from the beginning to the end. Thank you all for your comments and feedback on the manuscript.

I would also like to thank Ida Synnøve Folkestad Olsen and Jordan Donn Holl for their help during the sampling process, and Anna Kieu-Diem Tran her assistance in FARLAB.

I appreciate everyone in Team Jansen, at UiB, at ICTA, and UB who have spent time discussing data with me, for sharing their insights, and for encouraging feedback.

Special thanks Bendik for sharing his graphical expertise and to Kim for her support and helpful comments.

November 2018

Snorre Birkelund Wille

Table of contents

Abstract

Acknowledgements

1 Introduction

This thesis has been supervised by Professor Dr. Eystein Jansen and PhD Candidate Evangeline Sessford (Department of Earth Sciences, University of Bergen) and researcher Dr. Amandine A. Tisserand, (NORCE) all affiliated with the Bjerknes Centre for Climate Research (BCCR). This work has been accomplished within the funding of European Research Council under the European Community's Seventh Framework Programme/ERC grant as part of the Ice2Ice project.

1.1 The Ice2Ice project

This thesis is a contribution to the research project Arctic Sea Ice and Greenland Ice Sheet Sensitivity (ice2ice) that aims to resolve what caused the abrupt climate changes on Greenland during the past and what these dynamics imply for future climate change. The underlying hypothesis is that sea ice cover in the Arctic and sub-Arctic excerpts important controls on Greenland temperature and ice sheet variations.

The ice2ice project is a collaboration between research institutions in Bergen, Norway and Copenhagen, Denmark. The University of Bergen and NORCE, both partners in the Bjerknes Centre for Climate Research (BCCR), Niels Bohr Institute (NBI) of the Copenhagen University, and the Danish Climate Centre at the Danish Meteorological Institute (DMI).

Arctic sea ice is rapidly retreating, and the Greenland ice sheet is losing mass and experiencing warmer temperatures. To understand what lies ahead it is urgent to clarify the interactions between the Greenland ice sheet and the sea ice cover. The cryosphere has earlier been in fast transition during abrupt climate events, and these transitions can be seen as an analogue to potential near-future scenarios. The ice2ice project aims to better constrain the climatic conditions under time slices of abrupt climate change and warmer than present climatic conditions. A better understanding of the nature of observed events is obtained through empirical data from climate archives in synergy with a suite of models. For more details see: https://ice2ice.w.uib.no/overview/ice2ice-objectives/

1.2 Motivation

Greenland ice cores have revealed rapid climatic changes from cold stadial phases into warm interstadial phases followed by gradual cooling, before temperatures rapidly decrease back to stadial conditions during the last glacial cycle (Dansgaard et al., 1993; Huber et al., 2006). Known as Dansgaard-Oeschger (D-O) events, these are among the most dramatic abrupt climate change events in the geological record (Dokken et al., 2013), yet the processes behind the timing and the amplitude of these events are still debated.

Although the effects of the D-O events are well constrained in Greenland ice cores, there is also evidence of D-O events in marine and continental records in the North Atlantic and across the globe (Voelker, 2002). In association with D-O events, the North Atlantic Ocean is characterized by glacial sediments with layers of abundant ice-rafted debris (IRD) that reflect the releases of huge numbers of icebergs, known as Heinrich layers. These are considered to occur during the same period as the larger and longer-lasting stadials in the Greenland ice cores (Heinrich Stadials) (Bond et al., 1993; Hemming, 2004). Previous and ongoing studies suggest an important role of the Nordic Seas in regulating climate during D-O events (Rasmussen et al., 1996; Dokken and Jansen, 1999; Dokken et al., 2013; Ezat et al., 2017). The majority of these studies have extensively examined the vertical distribution of the water masses flowing into the eastern part of the Nordic Seas across Greenland Stadial (GS) and Greenland Interstadial (GI) periods, and only few studies are constraining the vertical distribution water column conditions during D-O events in the Denmark Strait region (Voelker et al., 2000). The aim of this work is to contribute to fill this gap in the current knowledge.

Significant changes in the upper water column in the Denmark Strait during D-O events were revealed based on planktonic foraminiferal stable isotopes (δ^{18}O and δ^{13}C) and IRD as surface proxies (Voelker et al., 2000). Parallel independent temperature estimations and oxygen isotopic measurements based on planktonic foraminifera can decipher the causes of variations of the oxygen isotope composition of seawater in the Nordic Seas. However, independent planktonic temperature reconstructions have been found to be challenging in this area (Meland et al., 2005). Constraints on Sea Surface Temperature (SST) estimates for the Nordic Seas based on planktonic foraminiferal assemblages is difficult due to the sporadic amount of species other than *Neogloboquadrina pachyderma* under the standard cold conditions (Pflaumann et al., 1996; Pflaumann et al., 2003). Minor/trace element measurements (in particular the ratio Magnesium over Calcium) from core-tops have yielded results too high to reflect near-surface modern temperatures North of Iceland (Meland et al., 2005). At the moment, there are no records of combined Mg/Ca and δ^{18}O existing for the Denmark Strait on the time scale of D-O events. One aspect I would like to address in this work is therefore to test whether Mg/Ca temperature reconstructions are reliable in this region during dramatic climate events of the last glacial period.

The primary objective of this thesis is to investigate the near-surface temperature from Heinrich Stadial 4 (HS4) into Greenland Interstadial 8 (GI8) in a high-resolution sedimentary archive from the Denmark Strait, located in close proximity to the Greenland Ice Sheet (GIS). This is achieved by a geochemical approach, combining planktonic Mg/Ca-temperature reconstruction with stable oxygen isotopes ($\delta^{18}O$) and carbon isotopes ($\delta^{13}C$) providing additional clues of water mass characteristics.

Foraminiferal calcite is susceptible to contamination by phases added to the tests post-mortem, including contamination from clays, organic material or post depositional overgrowths (Boyle, 1981). Such contaminants may produce bias in Mg/Ca analysis. Several cleaning protocols that are applied prior to Mg/Ca analysis have been developed to mitigate such bias. Two different cleaning methods are applied here, one more aggressive than the other, to test whether more the aggressive cleaning method improves the Mg/Ca record.

The main objectives of this study are to answer the following questions:

- Can Mg/Ca analysis reliably reconstruct near-surface temperatures during abrupt climate events in the Denmark Strait?
- Does a more aggressive cleaning of samples in preparation for Mg/Ca analysis aimed at contaminant-removal improve the Mg/Ca based temperature reconstructions in the record?
- What may Mg/Ca temperature reconstructions coupled with stable oxygen and carbon isotope records reveal about the near-surface temperature and water mass evolution in the Denmark Strait through abrupt climate events and particularly at the transition into GI8?

2 Background

2.1 The Climate system

Climate is usually defined as the mean weather commonly confined in 30-year intervals (IPCC, 2013), as exemplified by the variability of different parameters, such as temperature, precipitation and wind velocity. Climate may be understood as the state of the climate system that consists of the atmosphere, the hydrosphere, the cryosphere, the lithosphere, the biosphere, and the complex interactions between the different components (IPCC, 2013). Climate drivers that cause changes in the climate system are referred to as *climate forcings* and mainly include variations in solar radiation, in tectonic processes – such as large volcanic eruptions – and recently by anthropogenic influence. Changes in climate forcings are manifested through the different components of the climate system by physical, chemical, geological, and biological processes and interactions. Climate forcings can also trigger feedbacks that intensify or weaken the initial forcings. The processes wherein initial change in the climate causes secondary change that increases the effects of initial change are called positive climate feedbacks. Sea ice, as an example, has a much higher albedo – i.e. the ability of a surface to reflect solar radiation – than water, leading to a positive feedback where increasing sea ice extent promotes cooling and further expansion of sea ice. On the contrary, initial changes that are weakened by interactions are called negative feedbacks. Variations in forcings are manifested through a series of internal interactions, in which many are feedbacks, and the resulting climate change is a cumulative product of these. Feedbacks often operate until a new equilibrium state is reached, when climatic thresholds are crossed and a new climate state is introduced.

Interactions between different components of the climate system occur on all time scales. Carbon cycling is a good example of this statement: annual variations in the photosynthetic/respiratory balance is superimposed on the multi-million-year volcanic outgassing/weathering rate balance in modulating atmospheric CO_2 concentrations. The climatic response time is fastest for the lower atmosphere, from days to weeks. Ocean response time, due to the higher heat capacity, is slower and typically lag initial forcing by decades to millennia (IPCC, 2013).

Variations in heat distribution and related feedbacks are relevant on timescales discussed in this thesis include ice sheet dynamics and ice sheet modulation of atmospheric systems and atmosphere/sea-surface interactions particularly related to sea ice cover.

2.2 Climate variability

The Quaternary period which spans from 2.58 million years ago (Ma) to the present, is characterized by a re-occurring pattern of gradual ice-sheet growth, known as glacials, and rapid ice cover decay, i.e. interglacials (Hewitt, 2000). Climatic reconstructions for the Quaternary have revealed major climatic variations on global scale, as detected in Greenland and Antarctic ice cores (Dansgaard et al., 1993; Augustin, 2004; Jouzel et al., 2007a; Lüthi et al., 2008) and in marine sediments (Emiliani, 1955; Shackleton, 1967; Lisiecki and Raymo, 2005). There is a strong consensus that the most prominent signal in these records is caused by variations in the parameters of the Earth's orbit around the sun, causing seasonal and geographical changes in the distribution of solar radiation, also known as orbital forcings or Milankovitch cycles (Milankovitch, 1941; Wolff et al., 2010). The main periodic components consist of: (1) eccentricity of the Earth's orbit (405, 127, and 96 thousand years (kyr)), (2) obliquity, or the tilt, of the Earth's rotational axis (41 kyr), and (3) the precession of the equinoxes and the solstices due to "wobbling" of the rotational axis of the Earth (23 and 19 kyr) (e.g. Laskar et al., 2004). The periodicity of the glacial/interglacial cycles during the last ~700 kyr is consistent with the ~100 kyr eccentricity cycle (Figure 2.1) after having changed between ~1250 kyr and ~700 kyr from matching the 41 kyr obliquity forcing during the Early Pleistocene (Clark et al., 2006). The stacked benthic (species living at the ocean floor) $\delta^{18}O$ in Figure 2.1 (Jouzel et al., 2007a) refers to a combined ocean signal from a wide geographical distribution. The variations in the forcing resulting from eccentricity cycles is not thought to be sufficient to produce the dramatic observed climatic signal over glacial/interglacial cycles and have been proposed to rather control the effect of obliquity and precession (Imbrie et al., 1993; Cronin, 2010).

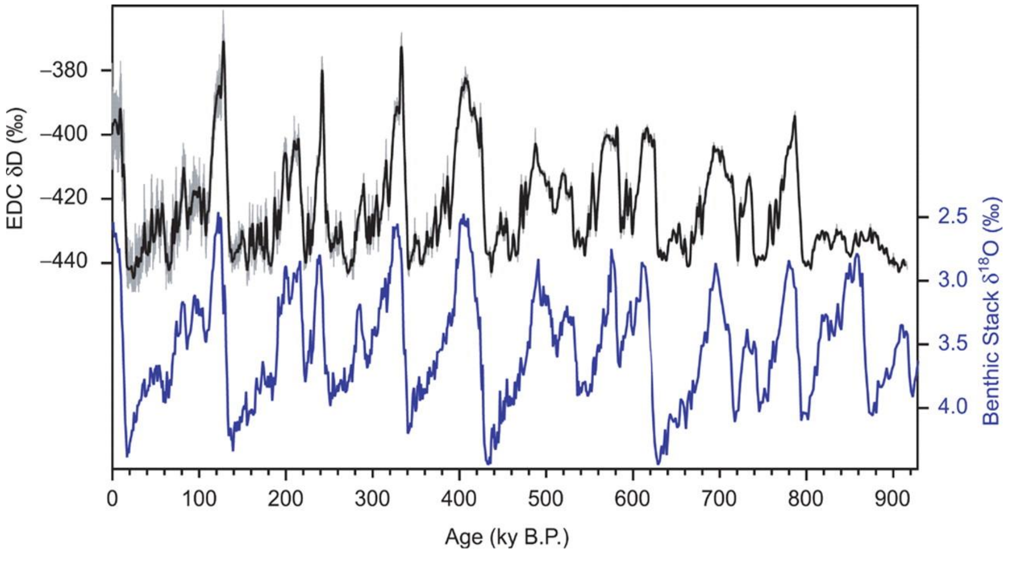

Figure 2.1: Two proxies for climate variability over the last 800 kyr. δD record from Antarctica Dome C (proxy for temperature) (Jouzel et al., 2001; Jouzel et al., 2007a) in black and stacked benthic $\delta^{18}O$ record (Lisiecki and Raymo 2005) in blue which both illustrate the striking periodicity in the climate record with an approximate 100 kyr period. From Jouzel et al. (2007a).

2.2.1 Dansgaard-Oeschger and Heinrich Events

Superimposed on orbital-scale climate cycles are abrupt millennial scale climate oscillations that have been observed throughout the Pleistocene that are too abrupt to be directly explained by orbital theories (Dansgaard et al., 1993; Raymo et al., 1998; McManus et al., 1999). Among these sub-orbital climate events are Dansgaard-Oeschger (D-O) events, first observed in ice-cores from the summit of Greenland (Dansgaard et al., 1993). D-O events are characterized by a strong temperature signal from $\delta^{18}O$ on Greenland, equivalent to 50% of the glacial/interglacial amplitude with suggested warming of 5-16°C (Wolff et al., 2010; Huber et al., 2006). Warm states are termed Greenland Interstadials (GI) and cold states are called Greenland Stadials (GS). These fluctuations are particularly pronounced and frequent in the Marine Isotope Stage (MIS) 3, between ~60 and 27 kyr (Figure 2.2) during intermediate glacial conditions. D-O events are defined by the Greenland ice core records as an abrupt warming where the $\delta^{18}O$ reaches a maximum within decades, followed by stepwise gradual retreat back into cold conditions ending with a sharp drop back into stadial conditions (Wolff et al., 2010). A total of 25 D-O events have been identified over the last glacial period (115-20 kyr) (Dansgaard et al., 1993).

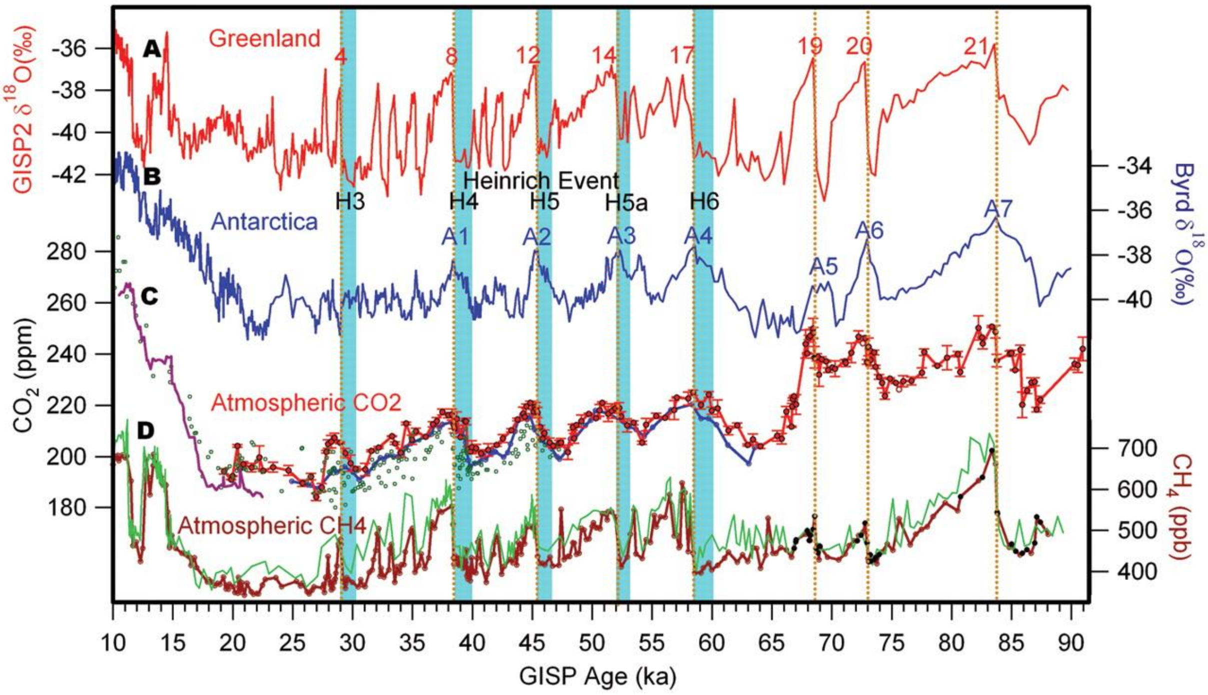

Figure 2.2: $\delta^{18}O$ records from A) Greenland (red) and B) Antarctica ice cores (blue), C) atmospheric concentrations of CO_2, and D) atmospheric methane concentrations, over the last glacial period (~90-10ka). Selected D-O events are numbered in red and Heinrich events are marked by blue columns. Figure from Ahn and Brook (2008).

Distinct ice-rafting events to the North Atlantic originating from the Laurentide ice sheet, termed Heinrich events, occurred temporally with some of the stadial phases preceding D-O warmings (Figure 2.2) and are associated with lower sea surface temperatures (SST) and salinity together with higher IRD (Ruddiman, 1977; Heinrich, 1988; Bond et al, 1992; Broecker, 1994). It has been hypothesized that Heinrich events are caused by internal glacial dynamics in which the ice caps collapse after the size crosses a destabilizing threshold (MacAyeal, 1993) or by climatic forcing accompanied by D-O warming (Alvarez-Solas et al., 2010). Because Heinrich events are not associated with every D-O event they are not likely to be integral to the dynamics of D-O cycles. The main focus will be on D-O events in this thesis, but since the stadial phase covered by the material here (GS9) is associated with Heinrich event 4, it will be referred to as Heinrich Stadial 4 (HS4) here.

D-O related climate signals are expressed globally and in most components of the climate system presented in section 2.1. Events on Greenland have been found to coincide with warmer and wetter climate in Europe (Genty et al., 2003), with enhanced summer monsoons in the Indian Ocean (Schulz et al,. 1998) and with a northward shift of the Intertropical Convergence Zone (ITCZ) (Schneider et al., 2014). Millennial scale climate change is also present in Antarctic records where temperatures vary in a sinusoidal fashion with smaller amplitudes compared to Greenland (Figure 2.2). Antarctic temperatures increase gradually during Greenland cold phases and the termination of Antarctic warming is coinciding with the onset Greenland warming (Blunier and Brook, 2001). Ocean circulation is considered to be one of the main drivers for global communication of these events.

2.2.2 Ocean circulation and D-O events

Studies correlating the Greenland D-O signal to North Atlantic sediment records have revealed changing SST, foraminiferal assemblages and IRD over D-O time-scales showing that the North Atlantic was affected and or involved in the D-O climate variations (Bond et al., 1993). Interstadials and stadials on Greenland are associated with different water masses in the North Atlantic and in the Nordic Seas (Curry and Oppo, 1997; Dokken and Jansen, 1999). Broecker et al. (1985) first postulated that variability in the stability of the Atlantic Meridional Overturning Circulation (AMOC) could lead to climate oscillations during the last glacial period and deep water formation rates in the northern Atlantic (Figure 2.3 for a schematic overview of the modern thermohaline circulation and AMOC).

The Thermohaline circulation (THC) refers to large scale ocean circulation driven by density gradients created by fluxes of heat and freshwater at the surface. Deep water is formed where seawater becomes dense enough to sink due to high salinity and/-or low temperatures (Broecker, 1991), notably in the Nordic Seas and Labrador Sea in the North Hemisphere and the Ross Sea and Weddell Sea in the South Hemisphere. Deep waters are subsequently spread through the basin. Upwelling of deep waters is thought to mainly occur in the Antarctic Circumpolar current, and along the coast of the continents, where Ekman transport leads to divergence due to prevailing westerly winds (e.g. Toggweiler and Samuels, 1993). Near-surface currents transporting water from low-latitudes poleward close the vertical cycle (Kuhlbrodt et al., 2007). The THC is closely related to the Meridional Overturning Circulation (MOC or AMOC for the Atlantic component) that refers to the northward flow of warm and salty surface waters and southward flow of colder deep waters. Unlike the THC, the MOC is also including wind driven currents.

A series of studies compiled by Voelker (2002) showed that GS/GI cycles during MIS3 are associated with interhemispheric redistribution of heat in the oceans. GI are coinciding with an anomalously warm North Atlantic and cool South Atlantic indicating a transport of heat from the southern hemisphere producing an enhanced overturning system. On the contrary, GS are associated with lower northward meridional heat transport. This model, often termed the bipolar "see-saw" (Stocker and Johnsen, 2003) consisting of "on" and "off" modes of the AMOC, is consistent with the antiphase relationship between Greenland and Antarctic isotope data (Figure 2.3) and migration of the ITCZ toward the warming hemisphere over GS/GI cycles. This model by variable northward heat transport by the AMOC has become a leading hypothesis in understanding abrupt climate change.

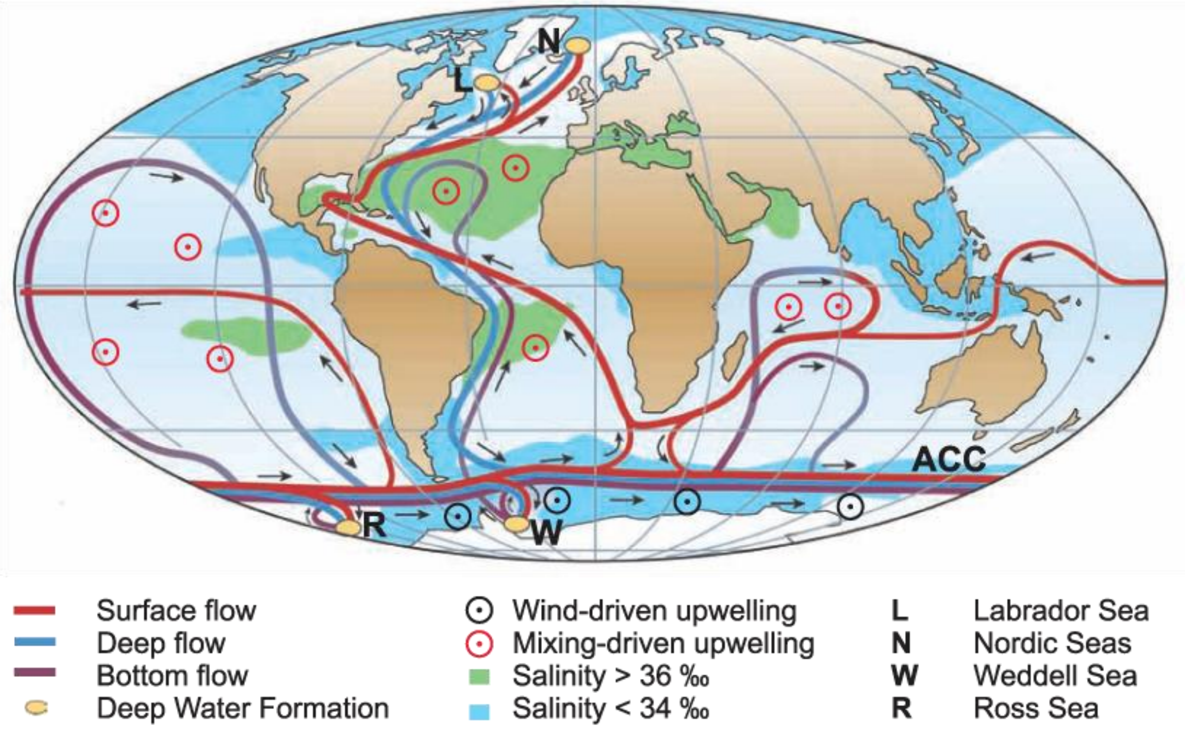

Figure 2.3: A schematic representation of the THC with MOC components. Note the dominantly northward surface currents and southward deep-currents in the Atlantic. Figure from Kuhlbrodt et al. (2007).

The atmospheric concentration of greenhouse gases varied on a millennial scale through the last glacial period and has been linked with changes in the AMOC (Schmittner and Galbraith, 2008). While methane (CH_4) and nitrous oxide (N_2O) correlate with Greenland isotope excursions where warm spikes coincide with spikes in CH_4 and N_2O; carbon dioxide (CO_2) co-varies with the Antarctic oxygen isotope records (Figure 2.2) (Blunier and Brook, 2001; Flückiger et al., 2004; Ahn and Brook, 2008). The variations of methane and nitrous oxide attest to changes in biogeochemical and ecosystem variability with D-O events (Blunier and Brook, 2001; Schmittner and Galbraith, 2008).

2.2.3 D-O triggers and forcing mechanisms

Despite the progress, there is still uncertainty regarding the causal mechanistic relationship in the observed AMOC variability and the climatic signal on Greenland and at other locations. Some have focused on mechanisms that disturb the large scale AMOC system, including fresh water perturbations in sites of deep-water formation with the idea that stratification would halt deep-water formation and thus the driver for the AMOC (Ganopolski and Rahmstorf, 2001; Vellinga and Wood, 2002). Such studies generally fit well with empirical data, although most climate models require unrealistically high freshwater input to suppress deep water formation (Dokken et al., 2013). Another approach has been to consider variations in the salinity of Atlantic water introduced to the sites of deep-water formation in the Nordic Seas (Broecker et al., 1990; Leduc et al., 2007). According to Leduc et al. (2007), increased transport of moisture over Central America would lead to saltier northbound Atlantic waters leading to an increase of deep water formation and thus strengthening the AMOC. Models considering this scenario have pointed out that CO_2 variations associated with the D-O cycles could act as a forcing to this pattern (Zhang et al., 2017).

The causal agent for the amplitude and abruptness of the abrupt D-O warming events is in many studies thought to be abrupt reductions in Nordic Seas/North Atlantic sea ice extent (Gildor and Tziperman, 2003; Li et al., 2005; Dokken et al., 2013). Expansive sea ice and fresh water cover in the Nordic seas/North Atlantic regions separates the sea surface from the atmosphere preventing heat flux from warm northbound ocean currents to the atmosphere. Sea ice increases the surface albedo, further cooling sea ice covered regions. Atmospheric general circulation models have indicated that retreat of sea ice in the Nordic seas causes 10°C winter warming at the Greenland summit (Li et al., 2010). Rapid transitions in deuterium excess in Greenland Ice cores associated with D-O cycles have been interpreted as latitudinal shifts of the moisture source for Greenland precipitation due to retreat or advance of North Atlantic sea ice (Masson-Delmotte et al., 2005; Jouzel et al., 2007b). Furthermore, similar models predict far-felt climatic shifts, such as the latitude migration of precipitation belts in the tropics cause by sea ice extent, consistent with proxy data (Dokken et al., 2013). Studies have shown that subsurface and intermediate waters were warmer in the southern Norwegian Sea during GS phases (Rasmussen and Thomsen, 2004; Dokken et al., 2013). This may be caused by subduction of warm Atlantic water below a fresh water lid and sea ice inhibiting heat loss to the atmosphere with the effect of regional atmospheric cooling. The presence of warm intermediate waters has potential for removing overlying sea ice if becoming sufficiently buoyant to break the stratification (Rasmussen and Thomsen, 2004).

3 Oceanography of the Nordic Seas

The Denmark Strait (DS), which is ~480 km long and ~290 km wide at the narrowest point, is located between Greenland and Iceland and connects the Iceland Sea to the Irminger Sea, a part of the Atlantic Ocean. The DS together with the Faroe Bank Channel forms the two main gateways for dense water from the Nordic Seas into the North Atlantic and constitute an important part of the thermohaline present-day circulation.

The core site is located on the northern side of the sill in the DS and in a crucial position to record variations in the influence of Atlantic and Polar water masses. Surface waters at the core site are influenced by Atlantic Water (AW) entering the Nordic Seas in the Northern Icelandic Irminger Current (NIIC), and Polar Surface Water (PSW) transported southwards in the East Greenland Current (EGC) (Figure 3.1).

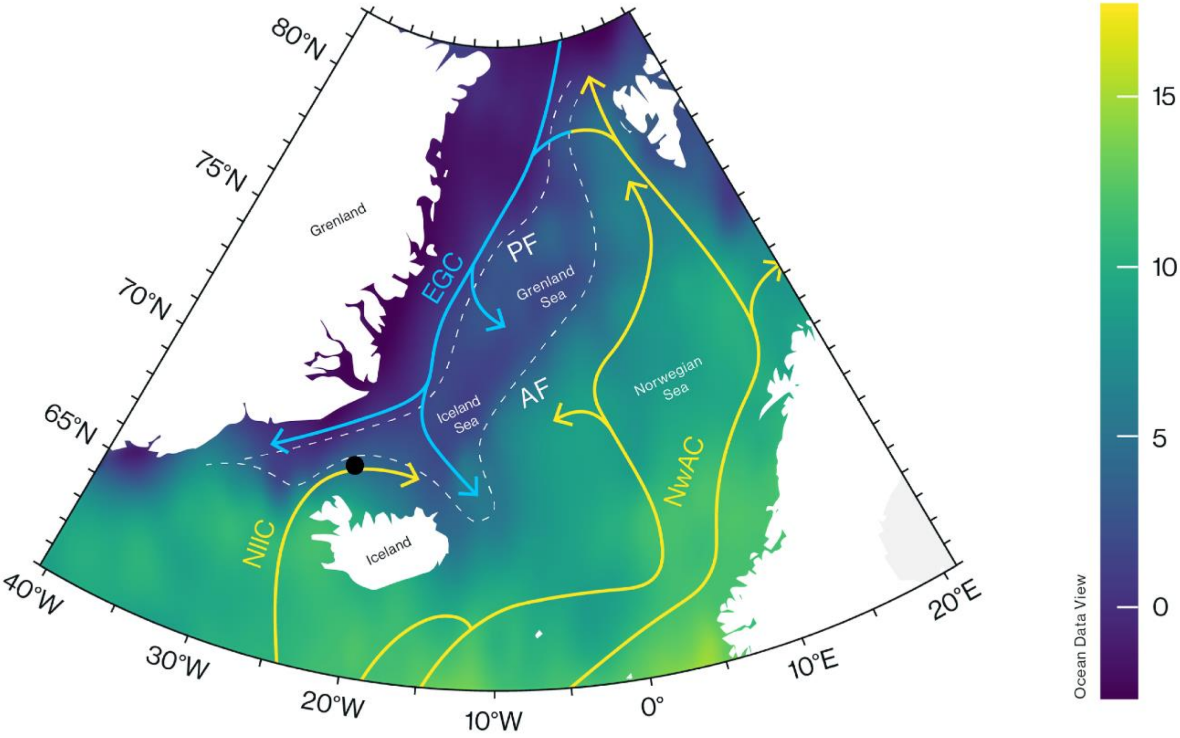

Figure 3.1: A regional map of the Nordic Sea including modern surface hydrology. The black dot indicates the core-site. The color scheme shows diva-gridded temperatures (°C) during the extended summer season (June, July, August, September: JJAS) at 10 m water depth, are derived from GLODAPv2 data (Olsen et al., 2016) and plotted using Ocean Data View (Schlitzer, 2018). Arrows schematically represent major currents influencing the area (after Våge et al., 2018; Isachsen et al., 2014; Macrander et al., 2014), with warm Atlantic pathways in yellow and cold currents in blue, mainly the East Greenland Current (EGC) , the East Icelandic Current (EIC) branching off in the Iceland Sea (IS). White dashed lines correspond to the Polar front (PF) and Arctic front (AF) that are drawn schematically based on temperature gradients in the area. Other abbreviations: NIIC: North Icelandic Irminger Current; and NwAC: Norwegian Atlantic Current.

3.1 Bathymetry

The Nordic Seas (here: Greenland, Iceland and Norwegian Seas) is a semi-enclosed basin where exchange of water from the Arctic Ocean and the North Atlantic Ocean occurs. It is also the primary site for deep-water formation in the Northern Hemisphere (Hopkins, 1991). Bathymetry plays a significant role in the dynamics of ocean circulation by limiting or directing it (Hopkins, 1991). The Nordic seas are connected to the Arctic Ocean by the Fram Strait in the north, and by the Barents Sea to northeast. While the Fram Strait is a deep, yet narrow passage, the Nordic Seas are separated from the Atlantic Ocean by the Greenland-Scotland Ridge, which forms a barrier for water exchange below 840 m water depth (Hansen and Østerhus, 2000). Exchange between the Atlantic Ocean and the Nordic Seas is enabled by three gaps in the barrier: (1) in the DS between Greenland and Iceland with a maximum water depth of ~620 m, (2) above the Iceland-Faeroe Ridge with a maximum water depth of ~480m, and (3) the Faeroese Channel between the Faeroe Islands and Scotland with maximum water depth of ~840m in the Faeroe Bank Channel (Hansen and Østerhus, 2000).

The main bathymetric features within the Nordic seas are continental shelves, the mid-ocean ridge with associated topographic sub-features, and its neighboring basins. The mid ocean-ridge system effectively separates the Nordic seas into the Norwegian Sea, Iceland Sea and Greenland Sea. The Iceland Sea is bounded by Iceland in the south, Greenland in the west, the Jan Mayen Fracture Zone and Jan Mayen ridge to the north and east respectively. Compared to the Norwegian and Greenland basins, the Iceland Sea is relatively shallow on the Icelandic plateau (Figure 3.2.A).

3.2 Nordic Seas Hydrography

Water masses may be distinguished by physical characteristics, i.e. temperature and salinity. Water masses in the Nordic Seas originate from the relatively warm and salty Atlantic Ocean and the cold and fresher Arctic Ocean. Mixing of these end-members in conjunction with heat-modification from interactions with the atmosphere; salinity-modification with the evaporation/precipitation balance; sea ice melting and continental run-off; and circulation patterns, create water masses of variable density. A schematic overview of major surface currents in the Nordic Seas is presented in Figure 3.1 and summer temperatures and salinity at different depths in Figure 3.3.

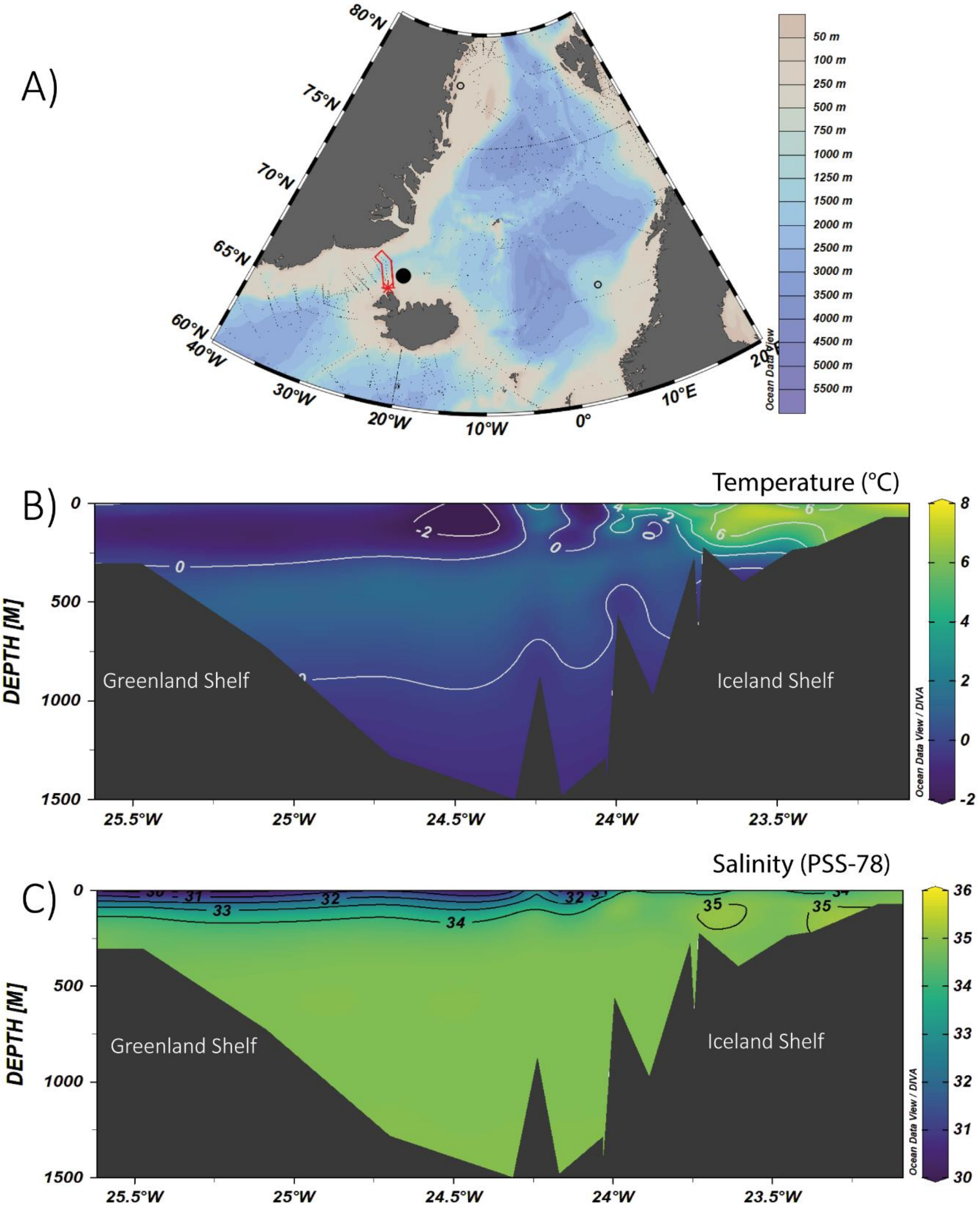

Figure 3.2: A) Water depths in the Nordic Seas with core-site indicated by the large black dot. Small black dots are data points for temperature and salinity plots from extended summer season (JJAS). The red polygon indicates position and data points included in profiles B and C. B) Present day temperature profile in the Denmark Strait between the Greenland and Icelandic Shelf. Note warm Atlantic waters covering the Iceland Shelf. C) Salinity over the same profile. Data is derived from GLODAPv2) data (Olsen et al., 2016) and plotted using Ocean Data View (Schlitzer, 2018).

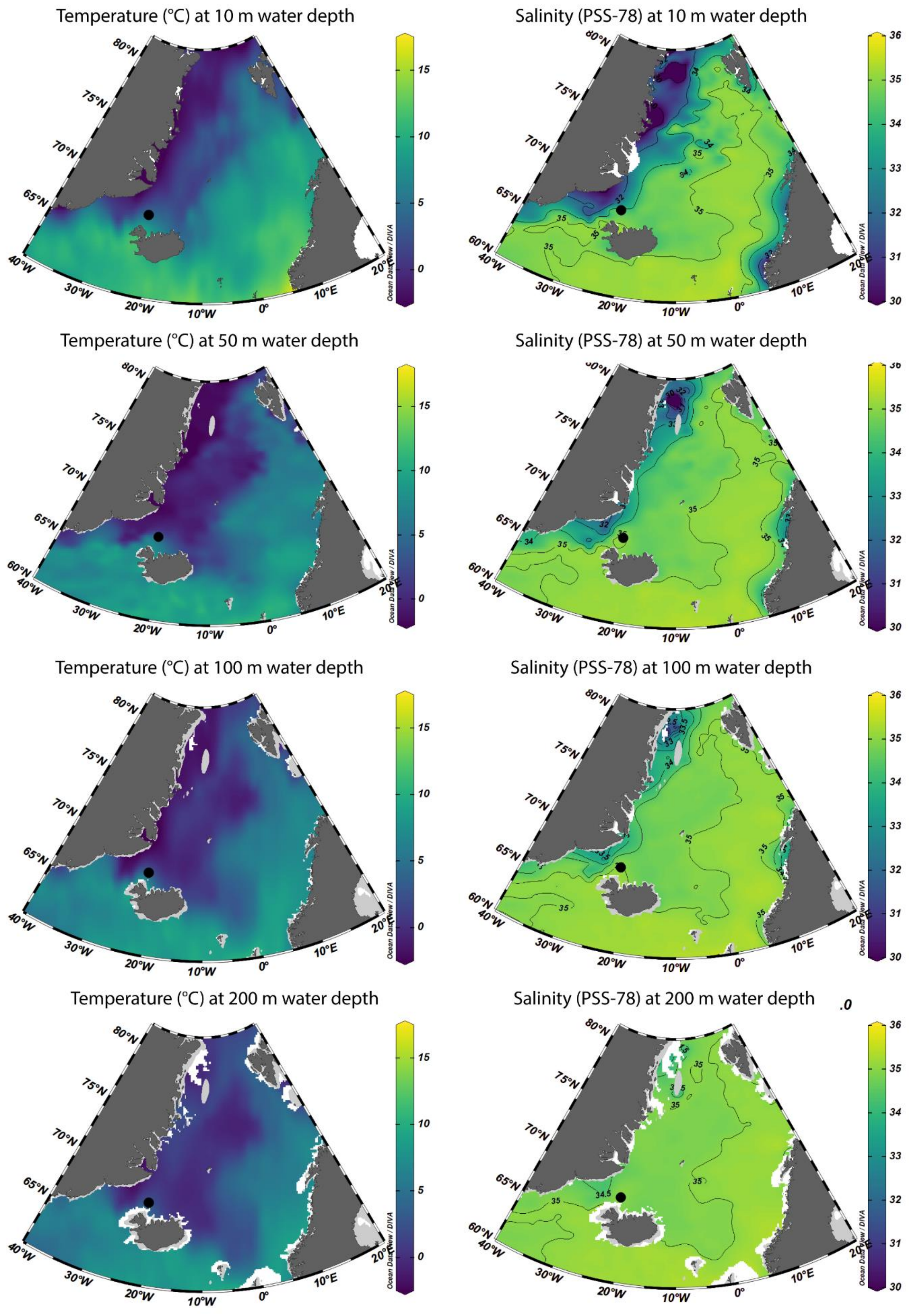

Temperature (°C) at 10 m water depth

Salinity (PSS-78) at 10 m water depth

Temperature (°C) at 50 m water depth

Salinity (PSS-78) at 50 m water depth

Temperature (°C) at 100 m water depth

Salinity (PSS-78) at 100 m water depth

Temperature (°C) at 200 m water depth

Salinity (PSS-78) at 200 m water depth

Figure 3.3: Present day temperature (left column) and salinity (right column) surfaces at 10, 50, 100, and 200 m water depth in the Nordic Seas with data from JJAS. Surfaces are extrapolated with diva-gridding from measured data points which locations are displayed in Figure 3.2.A. Black dot illustrates the core-site. Data is derived from GLODAPv2 data (Olsen et al., 2016) and plotted using Ocean Data View (Schlitzer, 2018).

Most of the Atlantic Ocean water masses that enters the Nordic Seas, do so through the Faeroese Channel in the Norwegian Atlantic Current (NwAC) (Østerhus et al., 2005) as a continuation of the North Atlantic Current (NAC) which brings relatively warm and saline surface waters from low to high latitudes in the Atlantic Ocean (Krauss, 1986). The NwAC gradually cools, releasing heat to the atmosphere, and mixes with adjacent water masses. The current follows the Norwegian continental slope with a branch reaching into the shallow continental shelf area of the Barents Sea (Loeng, 1991). A western branch of the NwAC is directed by the Mohns Ridge towards Jan Mayen effectively separating the Norwegian and Greenland Seas (Figure 3.1). Remnant Atlantic Waters that enter the Arctic Ocean through the Fram Strait are gradually modified and some returns southwards in the East Greenland Current (EGC) as intermediate and deeper water masses (Rudels et al., 2002). The EGC is the main southward surface conduit of water from the Arctic Ocean and Nordic Seas to the North Atlantic and transports cold, low salinity Greenland Polar Water (GPW) and sea ice along with recirculated Atlantic Water (Rudels et al., 2002). A strong halocline separates the GPW and Atlantic Originating Water (AOW), especially in summer due to increased melting (Hopkins, 1991) (Figure 3.2.C).

Atlantic water also enters the Nordic Seas through the DS in the Northern Icelandic Irminger Current (NIIC) flowing anticyclonically along the west coast of Iceland (Figure 3.1). The volume flux of the NIIC is weaker than the eastern inflows of Atlantic Water and somewhat cooler and of lower salinity, but it constitutes the major heat source for North Icelandic shelf waters and largely control temperature changes North of Iceland (Østerhus et al., 2005; Sicre et al., 2008). The influence of Atlantic water on the northern Icelandic shelf is highly variable, in terms of position and extent (Jónsson and Valdimarsson, 2005; Østerhus et al., 2005). The NIIC meets the EGC, which transports cold (-2 to 0°C), relatively fresh PSW and ice, in the Denmark Strait, and entrains PSW in the process. Modelling studies have shown that the flow rate of the NIIC over the Denmark Strait is heavily dependent on wind fields north-east of the Denmark Strait (Logemann and Harms, 2006).

The mixing of the surface endmembers, i.e. Atlantic Water masses and Polar Water masses, creates Arctic Surface Water (ArSW) (Hopkins, 1991). Mixing occurs predominantly in the gyres in the Greenland and Iceland Sea. ArSW summer stratification collapses during autumn and winter as heat is lost to the atmosphere resulting in mixing with intermediate waters.

The surface waters in the Nordic seas are of three distinct, in terms of temperature and salinity, water masses with a Polar domain, an Arctic domain and an Atlantic Domain (Swift and Aagaard, 1981). Due to the overall geometry where Atlantic waters mainly enters and flows northwards in the eastern part of the basin and Polar water exits the basin in the west, the frontal areas separating these water masses have a NNE/SSW trend. The polar front separates the low salinity GPW and ArSW along the margin of EGC (Figure 3.1). The Arctic front separates cold Arctic water masses, mainly in the Greenland and Iceland Seas, from warm Atlantic water masses, mainly in the Norwegian Sea (Hopkins, 1991). The core site is in vicinity of both fronts and is sensitive to variations in the influence of EGC, NIIC and the mixing of these water masses.

Denmark Strait Overflow Water constitutes about half of the total dense water overflow over the Greenland-Scotland Ridge and is thus an important component in the formation of North Atlantic Deep Water (NADW) contributing to the THC (Hansen et al., 2004). Most of the overflow is advected by the deeper water masses in the EGC, containing AOW (Tanhua et al., 2005; Våge et al., 2018). The other major overflow water contribution has been postulated to be of Arctic origin formed in the interior of the Iceland and Greenland Seas (Våge et al., 2018). The latter is formed in the Iceland Sea Gyre where Atlantic Water loses heat and forms an intermediate water mass returning to the North Atlantic through the Denmark Strait (i.e. eastern intermediate water >0°C in Figure 3.2.B) (Våge et al., 2013; Våge et al., 2018).

3.3 Climatic Setting

The climate in the Nordic Seas region is anomalously warm compared to the zonal mean due to the northward transport of heat in the North Atlantic Current (Seager et al., 2002).

The subpolar low-pressure zone around 60°N experiences merging of polar easterlies from high pressure systems in polar regions and prevailing westerlies from subtropical high-pressure systems. The Icelandic Low is a semi-permanent low-pressure cell centered around Iceland that influence the Nordic Seas region (Hopkins, 1991). Much emphasis has been put on the pressure difference between the Icelandic Low and the Azores High influencing the distribution of heat and moisture, wind direction and speed in the Atlantic Region (Hurrell et al., 2003). Pressure variations and connected systematic atmospheric and ocean variations have been termed the North Atlantic Oscillation (NAO) and has been shown to vary on inter-annual to decadal timescales with large implications, especially during wintertime. A positive NAO refers to a large pressure gradient and permits a strengthening of the westerlies with resulting increases in heat transport to the eastern Nordic Seas. A positive NAO index is also associated with intense and frequent storms near the Iceland and Norwegian Sea and more precipitation over Iceland (Hurrell et al., 2003). The intensity of winter convection in the Nordic Seas also appear to be synchronized to the NAO-index (Dickson et al., 1996). It is important to consider that the atmosphere-ocean interaction is not one- directional but works as a coupled system.

The modern configuration of pressure systems is not necessarily a direct analogy to glacial climates in the Nordic Seas region. The presence of thick Laurentide and Fennoscandian ice scheets during Last Glacial Maximum (LGM) have been shown in model simulations by Pausata et al. (2011) to shift the Iceland Low and Azores High southwards and with a lower pressure gradient between them, analogous to a more negative modern NAO. In accord with a more negative NAO, simulations with an atmospheric general circulation model study by Li and Battisti (2008) showed that the LGM Atlantic circulation was characterized by a more zonal Atlantic Jet. More frequent meridional excursions of the jet and storm tracks, similar to the modern North Atlantic, was shown to occur when the Atlantic region is devoid of sea ice (Li et al., 2010).

4 Theory, materials, and methods used in this study

An introduction to the materials and proxies used in this study is presented in this chapter, followed by a description of the laboratory procedures and instruments involved in acquiring the data that is presented in chapter 5.

The core studied in this thesis, core GS15-198-36CC, was recovered using a calypso coring device during summer 2015 from the continental slope in the Northern Denmark Strait at 67°51,655'N 21°52,898'W and 770 m water depth (Figure 3.1). The total length of the core is 1953 cm and was cut into 14 sections, each split into a working part and an archive part. Materials for this thesis are covered in section 3 and 4 between 285 cm and 340.5 cm. A lithological description of the core section will be provided in section 5.1.

4.1 Planktonic Foraminifera

Foraminifera are unicellular organisms, mainly marine eukaryotes that secrete their calcite shells, often called tests, in an aquatic environments. While most species of foraminifera live at the seafloor, called *benthic foraminifera*, about a group of ~50 species live in the upper water column, forming part of the plankton community and are called *planktonic foraminifera* (Kucera, 2007). Planktonic foraminifera typically prefer photic conditions but may submerge to about 1000 m and are found from the tropics to high latitudes, commonly in the open ocean (Kimoto, 2015). The geographical distribution of planktonic foraminifera is controlled by environmental factors, as species are adapted to different conditions. Thus, the absolute and relative abundance of different species at a specific sight may provide environmental information about ocean temperature and ecological conditions (e.g. Phleger, 1939). Calcite tests of planktonic foraminifera compose a significant portion of the open marine sediment flux (Erez, 2003; Kucera, 2007) and are valuable materials for reconstructions of climatic and environmental parameters.

In paleoceanography, shells of foraminifera are the most used proxy for past ocean conditions, in particular temperature (Lea, 2014; Kucera, 2007). The stable isotope composition is widely used as a proxy for water composition and temperature, and trace element composition (Mg/Ca ratio), as a proxy for ocean temperature (Ravelo and Hillaire-Marcel, 2007; Lea, 2014). Planktonic foraminifer's sensitivity to environmental ambience, wide habitat diversity and disposition for preservation in the sediments, make them valuable in paleoceanography and paleoclimatology in general. In this thesis the chemical composition of the planktonic shells is used and therefore an overview of such proxies is provided in section 4.3.

As planktonic foraminifera float in the water column it is important to have knowledge of the ecology of the species that are analyzed, with special attention to the time-spatial distribution during calcification. On that note, a brief introduction on the ecology of the planktonic species used for geochemical analyses here follows below.

4.2 *Neogloboquadrina pachyderma*

Neogloboquadrina pachyderma (here *N. pachyderma*) is the most characterizing species of planktonic foraminifera in high-latitude waters in both hemispheres and comprise the majority of the planktonic foraminiferal species assemblage in both Polar Regions (Eynaud, 2011). In the Nordic Seas, *N. pachyderma* has been found to constitute >90% of the surface sediment assemblage while *Turborotaltita quinqueloba* and *Globigerina bulloides* comprise the rest of the polar frequenting species (Pflaumann et al., 1996). *N. pachyderma* has even been found overwintering in Antarctic sea ice in concentrations higher than in the underlying water column (Dieckmann et al., 1991). Arctic and Antarctic stocks represent different genotypes out of possibly seven individual genotypes of *N. pachyderma (*Darling et al., 2007).

There is some uncertainty regarding the depth-habitat and calcification depth of *N. pachyderma* and which parameters that determine the distribution. *N. pachyderma* is thought to inhabit and calcify at a wide range of depths in the Nordic Seas from 40 to 250 m water depth and it migrates downwards through its life cycle (Simstich et al., 2003). It is likely that *N. pachyderma* calcifies and inhabits different depths in different oceanographic regions. Simstich et al. (2003) also found that the calcification off Norway was at 70-250 m and at 70-130 m below the EGC in the nutrient rich- well-developed halocline. At the ice margin in the Arctic, *N. pachyderma* has been found to inhabit warmer Atlantic waters below cold and fresh Polar surface waters between 50-200 meters water depth (Carstens et al., 1997). A study from the northeast water polynya off the eastern Greenland coast by Kohfeld et al. (1996) found that *N. pachyderma* inhabits and grows at depths between 20-80 m in the zone related with the chlorophyll maximum. Bauch et al. (1997) in accord with Kohfeld el al. (1996) proposed that *N. pachyderma* depth distribution is not strictly controlled by physical parameters, i.e. temperature and salinity, but to food and light supply given by a preferred depth-habitat of 100-200 m in the Arctic Ocean. Planktonic foraminifera are known to avoid low salinity environments, and *N. pachyderma* has been shown to normally occupy environments with salinities between 35-36 psu (Ravelo and Hillaire-Marcel, 2007).

Despite the discussion regarding the depth-distribution of *N. pachyderma*, there is general agreement that it migrates downwards through its life cycle. Detailed intra-test studies have indicated differences in the test-composition at different stages through the life cycle that are related to depth (Kozdon et al., 2009). At depth, during the latter part of the life cycle, *N. pachyderma* shows potential for encrustation in which chemically different calcite precipitates on the tests, constituting up to 70% of the total mass of the specimen (Kohfeld et al., 1996). As *N. pachyderma* migrates downwards through its life cycle, the bulk chemical composition reflects a continuum of depth from early ontogenic calcite to the crust (Kozdon et al., 2009).

The summer average from July to September (JAS) is thought to represent the main production season for planktonic foraminifera in the Nordic Seas (Meland et al., 2006). In Polar Waters, predominant in the western Nordic Seas and the core-site in this study, the main blooming season for *N. pachyderma* is limited to ice-free conditions during JAS (Schiebel and Hemleben, 2005). In Atlantic water masses, which also influence the core site in this study, there is also a bloom during spring (Jonkers et al., 2010b).

In studies on deposited planktonic foraminifera, it is often assumed that collected specimens have inhabited surface water masses directly above the core location (Sebille et al., 2015). However, ocean models have indicated that under the right oceanographic conditions, planktonic foraminifera may be transported over significant distances and deposited specimens therefore may reflect distant oceanographic conditions (Sebille et al., 2015).

4.3 Climate Proxies

Proxies are biological, physical or chemical measurements in climate archives that stand in for direct observations of climate parameters and data derived from proxies can be calibrated against modern analogs to provide quantitative information (IPCC, 2013). To understand the processes that link proxies to climate parameters is fundamental for their application (Cronin, 2010). On that note, a brief theoretical outline of the climate proxies used in this thesis will be presented in this subchapter.

4.3.1 Stable isotopes

The stable isotope ratios of oxygen ($^{18}O/^{16}O$) and carbon ($^{13}C/^{12}C$) are frequently used in reconstructions of past climate and biogeochemical parameters in numerous archives. An isotope is a variant of an atom whose nucleus contains a different number of neutrons to protons (Hoefs, 2018). An isotope with added neutrons is therefore of higher atomic mass than the atom of an equal number of protons and neutrons. Chemical properties of an atom are generally determined by the number and configuration of electrons, but slight variations in mass do produce subtle differences in physical behavior (Hoefs, 2018).

Stable isotopes are useful as proxies as the ratio of heavy to light isotopes in a material is a consequence of many variables, in which many are related to climate such as ice volume, hydrography, moisture source, ocean temperature and atmospheric temperature (Cronin, 2010). Processes that affect the isotopic ratios can therefore be reconstructed based on isotopic relative abundance. The ratio of heavy to light isotopes is a result of slight enrichment of one isotope relative to another in a chemical or physical process due to the small differences in mass during the process (Hoefs, 2018). This differential uptake of the heavier or lighter isotope during the formation or breakdown of a compound is termed "fractionation". Thermodynamic reactions are subject to fractionation of isotopes as different molecular species have different reaction rates. Generally, molecules that are built of light isotopes react more easily than heavier equivalents as their bonds are relatively weaker (Hoefs, 2018).

There are two main phenomena that control isotopic fractionation: equilibrium isotope distribution and kinetic effects (Hoefs, 2018). Equilibrium isotope distribution is modeled by classical thermodynamics as reactions approaching isotopic equilibrium and are mostly related to temperature. Kinetic effects produce fractionations in reactions in non-equilibrium that are associated with unidirectional or incomplete reactions such as evaporation and biologically controlled reactions (Hoefs, 2009). Kinetic reactions are irreversible and cannot be treated with traditional thermodynamic methods. The factor of fractionation, α, is defined as the ratio of isotopes (R_A and R_B) in one phase (A) to the other phase (B).

$$\alpha_{A\text{-}B} = \frac{R_A}{R_B}$$ Equation 1 (Rohling and Cooke, 1999)

To accurately determine absolute abundances of isotopes is very difficult. However, the determination of relative abundances between two samples can be performed with much higher precision. In practical terms a set of references with known isotopic values are used in comparison to samples. These references, or standards, are used internationally to compare isotope data from different laboratories. The accepted denotation of isotope ratio measurements is in the delta value (δ given in per mill (‰)) that denotes the difference in the ratio of the sample (R) compared to a standard:

$$\delta_{(\text{Sample})}\ ‰ = 1000 * \frac{R_{(Sample)} - R_{(Standard)}}{R_{(Standard)}}$$ Equation 2 (Hoefs, 2018)

A sample with higher ratios relative to the standard is often referred to as heavy, or enriched in respect to the heavier isotope, and a sample with lower ratios is referred to as light, or depleted in respect to the lighter isotope.

4.3.2 Oxygen isotopes

Oxygen occurs in gaseous and liquid form in addition to solid compounds which are stable over high temperature ranges (Hoefs, 2009). Its highly reactive nature as an oxidative agent and wide abundance gives oxygen a central role in regulating and mediating biogeochemical processes on Earth. Oxygen is a major constituent of the atmosphere and the hydrosphere and is therefore an important constituent of the climate system. There are three stable isotopes of oxygen naturally occurring ^{16}O, ^{17}O and ^{18}O, with the relative abundances of 99.76%, 0.04% and 0.20% respectively (Rohling and Cooke, 1999). The ratio of $^{18}O/^{16}O$ is most normally used in palaeoclimatological research owing to the larger mass difference and higher abundance.

Palaeoclimatological research is most concerned with fractionation of oxygen isotopes related to the hydrological cycle. The processes that causes phase change and fluxes between the hydrological reservoirs also cause fractionation of oxygen isotopes which provides a close link between the hydrological cycle and $\delta^{18}O$. These include evaporation, transport of atmospheric vapor, precipitation, sea ice freezing and melting, water stored as continental ice and river run-off (Rohling and Cooke, 1999). See Figure 4.1 for an overview.

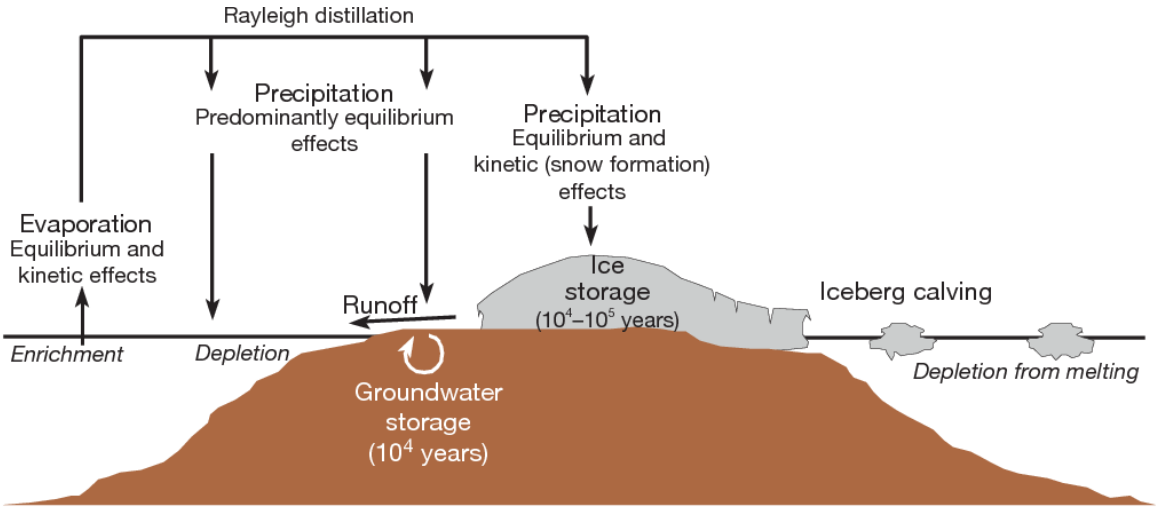

Figure 4.1: Schematic depiction of the hydrological cycle with its relationship to distribution of oxygen isotopes in respect to the evaporation/precipitation balance, storage in ice and seawater. Figure from Rohling (2013).

When water evaporates from the ocean, the vapor is enriched in ^{16}O because of higher vapor pressure. This process yields higher fractionation than predicted under equilibrium distribution due to kinetic effects (Hoefs, 2018). As the vapor is transported, the vapor is further enriched in ^{16}O as the heavier isotope more readily precipitates. This process is largely opposite to evaporation, although kinetic effects are negligible (Rohling and Cooke, 1999). The effect of this fractionation is that remaining surface water is enriched with respect to ^{18}O, the first precipitation is similar in composition as the source of the moisture, and the transported vapor becomes increasingly depleted in respect to ^{18}O. This evaporation/precipitation relationship is a successive cycle which leads to progressively lower $\delta^{18}O$ in waters towards the poles and continental interiors. Adding to this pattern is the altitude effect where the isotopic composition of water becomes lighter with increasing altitude because air masses hold less water when cooled. As rivers transport depleted waters back to the oceans, coastal waters in connection to fresh water are depleted in respect to ^{18}O.

Glaciers serve as reservoirs storing $\delta^{18}O$-depleted water. During ice ages, this process leads to significant alterations in the global $\delta^{18}O$ budget with an enrichment of ^{18}O in the ocean (high $\delta^{18}O_{sw}$) (Shackleton, 1967) as glacial ice storage works on a longer time scales ocean ventilation.

The process of sea ice formation and melting affects local $\delta^{18}O$ as newly formed ice is enriched by 2.57±10‰ relative to seawater (Macdonald et al., 1995). Isotopically light brines are also formed which can cause convection carrying relatively saline waters with low $\delta^{18}O$ values into the interior.

Generally, the $\delta^{18}O$ values of the surface ocean is a function of the evaporation/precipitation balance and input of freshwater superimposed on changes in ice volume. Because $\delta^{18}O$ of seawater and salinity are both influenced by the evaporation/precipitation balance, they are correlated in the surface ocean, expressed with a meridional gradient of higher values at low latitudes and lower values at higher latitudes (Ravelo and Hillaire-Marcel, 2007). Advection and mixing of water masses from their respective source area ultimately control the stable oxygen composition of seawater ($\delta^{18}O_{sw}$) at any given site (Rohling and Cooke, 1999), which creates regional deviations in the overall global relationship between $\delta^{18}O_{sw}$ and salinity (Ravelo and Hillaire-Marcel, 2007). The $\delta^{18}O_{sw}$ is a calculation based on oxygen isotope values and temperature reconstruction from foraminifera.

4.3.2.1 Oxygen isotopes in foraminifera

The calcite shells secreted by planktonic foraminifera are constructed by ions present in the ambient seawater. The isotopic composition of biogenic carbonate ($CaCO_3$) therefore reflect the composition of the ambient seawater ($\delta^{18}O$) as discussed in section 4.3.2. The fundamental reaction for calcium carbonate precipitation is given by the following equation.

$Ca^{2+} + 2HCO_3^- \rightleftharpoons CaCO_3 + CO_2 + H_2O$ Equation 3 (Rohling & Cooke, 1999)

In the 1940s it was determined that the isotopic composition of calcite can be used as a thermometer for the waters in which it calcified (Urey, 1947). This idea was applied on planktonic foraminiferal calcite by Cesare Emiliani in the 1950s (Emiliani, 1955). In agreement with Epstein (1953), he noted that oxygen isotopes represented the isotopic composition of the ambient water in addition to temperature. Further he argued that during glacial times, large accumulation of ice sheets must have affected the global composition of seawater. This breakthrough initiated the quest to develop empirical equations that relate the isotopic composition of the calcite ($\delta^{18}O_{calcite}$), the isotopic composition of ambient seawater ($\delta^{18}O_{sw}$), and temperature (T) to serve as a paleothermometer. Epstein et al. (1953) produced the classical paleotemperature equation which has later been revised by Shackleton (1974):

$$T\ (^{o}C) = 16.9 – 4.38\ (\delta^{18}O_{calcite} - A) + 0.10\ (\delta^{18}O_{calcite} - A)^{2} \qquad \text{Equation 4}$$

Equation 4 has two unknowns: the calcification temperature and the isotopic composition of seawater. As described above, the isotopic composition varies over time and space and cannot easily be estimated which results in uncertainties in direct temperature calculations. However, coupled with an independent paleothermometer $\delta^{18}O_{sw}$ may be better estimated and used as a tracer for hydrographical variability (Mashiotta et al., 1999; Lea et al., 2000).

In the $\delta^{18}O_{sw}$ calculation here, sea level change and the temperature effect on $\delta^{18}O_{calcite}$ is corrected for and the VDPB scale is converted to SMOW. The sea level reconstruction from Waelbroeck et al. (2002) was used to account for the $\delta^{18}O_{sw}$ shift of 0.0092‰ per meter sea level change due to the glacial effect (Shackleton, 1974). The average $\delta^{18}O$ of the core tops (3.515‰) was used as a modern reference for downcore sea-level corrections. The reconstructed temperature record by Mg/Ca, as explained in section 4.3.4, was used as the independent temperature record to account for the temperature effect in $\delta^{18}O_{calcite}$ which is 0.23‰ per °C (Shackleton, 1974). Furthermore, modern calcification temperatures and $\delta^{18}O_{calcite}$ are corrected for downcore from average temperature (6.82°C) core-top Mg/Ca temperature reconstructions. The difference between the VPDB and $\delta^{18}O_{sw}$ (SMOW) was corrected for using a constant of 0.3‰ (Sessford et al., 2018). The formula thus becomes:

$$\delta^{18}O_{sw} = (\delta^{18}O_{downcore} - \delta^{18}O_{coretop}) - (\text{sea level (m)} * 0.0092) - ((T°C_{coretop} - T°C_{downcore})*0.23) + 0.3 \qquad \text{Equation 5}$$

Palaeothermometry equations assume that the biogenic carbonate precipitates in equilibrium with sea water. Research in this field is still linking how environmental and ecological parameters control precipitation that produces an offset from equilibrium. Known examples of such “vital effects” include ontogenic effects, namely effects caused by the development of an organism, symbiont photosynthesis effects, respiration effects, gametogenic calcite effects and carbonate chemistry variations, mostly connected to concentrations of CO_3^{2-} (Rohling and Cooke, 1999).

4.3.3 Carbon isotopes

Two stable isotopes of carbon are naturally occurring on Earth: ^{12}C and ^{13}C and have the relative abundances of 96.89% and 1.11% respectively (Faure, 1986). ^{14}C is a radioactive isotope that is commonly used as a dating tool of organic material due to its half-life of 5,730±40 years (Godwin, 1962). The $\delta^{13}C$ of foraminiferal calcite reflects the carbon isotope composition of the dissolved inorganic carbon (DIC) in the ambient seawater, but calcification does not occur in isotopic equilibrium with seawater (Ravelo and Hillaire-Marcel, 2007). Changes in $\delta^{13}C_{DIC}$ occurs globally and geographically in close connection with the carbon cycle.

The carbon cycle is complex; subjected to feedbacks and operating over different timescales from daily photosynthetic cycling to tectonic burial and volcanism. By far, the largest carbon reservoirs are the mantle and crust. The surface reservoirs i.e. the ocean, biosphere and atmosphere are progressively smaller, but the exchange rate between the reservoirs is generally inverse to their size (Wallmann and Aloisi, 2012). It is convenient to characterize the carbon cycle in organic and inorganic components. Organic carbon cycling is dominated by photosynthesis and respiration with average $\delta^{13}C$ of about -25‰ whereas inorganic carbonate reservoirs have an average $\delta^{13}C$ of about 0‰ being governed by carbonate reactions and the chemistry of available carbon (Rohling and Cooke, 1999).

The global average $\delta^{13}C_{DIC}$ of the ocean varies over time by changes in the global carbon cycle and the portioning and fluxes in and between the carbon reservoirs (Ravelo and Hillaire-Marcel, 2007). The process of photosynthesis, particularly related to the C_3 pathway, heavily favors incorporation of ^{12}C leaving organic matter is depleted with respect to ^{13}C with an average between -25‰ and -27‰ (Alonso-Cantabrana and von Caemmerer, 2016). Processes that influence the size of the global organic carbon reservoirs are therefore modifying the $\delta^{13}C$ of inorganic carbon ocean in the atmosphere (Ravelo and Hillaire-Marcel, 2007). Such processes include the rate of fixation of carbon in terrestrial environments and rates of preservation and burial of organic material. Alterations of these rates may be caused by glacial modification of the size of the terrestrial biosphere or ocean anoxic events leading to increased preservation of organic matter. Conversely, the oxidation of preserved organic matter, or heavily depleted gas hydrates, cause a depletion of mean ocean and atmosphere ^{13}C (Ravelo and Hillaire-Marcel, 2007).

The discrimination of ^{13}C during photosynthesis have implication for local variations, and in depth-profile, of variations in $\delta^{13}C_{DIC}$ in the ocean. After marine producers preferentially take up ^{12}C in the photic zone, the unconsumed organic matter sinks down in the water column leaving the surface waters enriched in ^{13}C (Rohling and Cooke, 1999). The sinking organic matter is mostly respired and recycled back to inorganic carbon deeper in the water column releasing ^{12}C leaving deeper waters enriched in ^{12}C (Ravelo and Hillaire-Marcel, 2007). Increased productivity in the surface therefore increases the transport of ^{12}C to the deeper waters and creates a steeper profile. This profile resembles nutrient profiles as nutrients are also liberated as organic matter re-mineralizes. δ^{13}C values decrease with age when water masses are isolated from the mixed surface layer due to gradual decomposition of organic matter and mixing (Dokken et al., 2013). Since δ^{13}C is related to the water mass age, δ^{13}C can be used to track ventilation changes. Furthermore, the δ^{13}C at a given site may be influenced by the mixing of water masses with different δ^{13}C signatures (Ravelo and Hillaire-Marcel, 2007).

At isotopic equilibrium between the atmosphere and the surface ocean, colder waters have higher δ^{13}C than warmer waters (Mook et al., 1974). Because the timescale for ^{13}C equilibrium is ~10 years, about an order of magnitude slower than that of CO_2, equilibrium is rarely achieved as water masses rarely reside in a surface region over such timescales (Lynch-Stieglitz et al., 1995; Schmittner et al., 2013).

The δ^{13}C of foraminiferal calcite reflects the carbon isotope composition of DIC in the ambient seawater, but deviations from isotopic equilibrium occur due to kinetic and vital effects (Ravelo and Hillaire-Marcel, 2007). Romanek et al. (1992) found that kinetic fractionation causes calcite in foraminifera to be 1.0 ± 0.2‰ enriched in ^{13}C relative to DIC. Vital effects offsetting the biogenic carbonate from equilibrium include activity by symbionts, growth rate and response to carbonate ion concentration variations (Rohling and Cooke, 1999).

4.3.3.1 ^{14}C dating

Radiocarbon (^{14}C) is produced in the upper atmosphere by cosmic ray neutrons bombarding molecular nitrogen (N_2) (Cronin, 2010). Newly produced ^{14}C subsequently becomes integrated in the carbon cycle. Living organisms continuously replenish ^{14}C which decays to ^{14}N with a half-life of 5730 years (Godwin, 1962). The replenishment of ^{14}C stops when the organism dies. Thus, radiocarbon dating is based on measuring the remaining ^{14}C in organic material to know the age of said material. However, ^{14}C years do not equate to calendar years directly because production rates of ^{14}C in the atmosphere varies through time (Stuvier, 1961; Reimer et al., 2009), and also by changes in the partitioning in different carbon reservoirs over time (Siegenthaler et al., 1980), recently by human activity (Stuvier and Quay, 1981). Conversions from radiocarbon years to calendar years is therefore achieved through calibration (e.g. Reimer et al., 2009).

4.3.4 Mg/Ca-thermometry

The ratio between Magnesium and Calcium (Mg/Ca) in calcite is widely used as a proxy for reconstructing past ocean temperatures (Kucera, 2007; Katz et al., 2010). Mg/Ca may serve as an independent temperature record that can be used to correct for the temperature effect on $\delta^{18}O_{calcite,}$ which allows for the oxygen isotope composition of the seawater ($\delta^{18}O_{sw}$) to be constrained (Mashiotta et al., 1999). Thus, $\delta^{18}O_{sw}$ can itself can be used to reconstruct changes in the local hydrography as described in section 4.3.2.1 (Lea et al., 2000; Duplessy et al., 1992).

4.3.4.1 Inorganic carbonate precipitation

Already in the early 20th century, Clarke and Wheeler (1922) found that the abundance of magnesium (Mg^{2+}) incorporated in their shell could be related to temperature during calcite growth since the Mg concentration in seawater is nearly constant throughout the world's oceans. The fundamental principle for using Mg/Ca ratio as a method to reconstruct temperatures is that the substitution of Mg^{2+} in calcium carbonate is an endothermic reaction and the Mg/Ca ratio of the calcite is expected to increase with increasing temperature. The van't Hoff equation describes that a reaction associated with heat of reaction (ΔH), or enthalpy change, will be sensitive to temperature (Garrels and Christ, 1965):

$$\frac{d\ln K}{d(\frac{1}{T})} = -\frac{\Delta H}{R} \qquad \text{Equation 6}$$

Where *R* is the universal gas constant, *T* the temperature in kelvin and *K* the equilibrium constant for the equation. The relationship in Equation 6 predicts an exponential increase with temperature. ΔH has been estimated to be 21kJ/mol for substitution of Mg^{2+} in calcite (Koziol and Newton, 1995) which indicates that under ideal thermodynamic conditions, the Mg/Ca ratio in calcite should increase exponentially by 3% per degree Celsius increase temperature between 0°C and 30°C (Rosenthal et al., 1997; Lea et al., 1999).

Empirical experiments by precipitating inorganic calcite are in agreement with the thermodynamic prediction from the van't Hoff equation (Katz, 1973; Mucci, 1987; Omoori et al., 1987). One example being Omoori et al. (1987) who found that the distribution coefficients (λMg) of Mg^{2+} in calcite precipitated in seawater to be between 0.012 ± 0.001 at 10°C to 0.040 ± 0.003 at 50°C. This corresponds to a ~3% increase in the distribution of Mg^{2+} in calcite per degree Celsius.

4.3.4.2 Magnesium to calcium ratio in foraminifera

The Mg/Ca composition of calcite in planktonic foraminifera and the sensitivity to temperature deviates from thermodynamic predictions and thus from inorganic calcite. Mg^{2+} abundance in foraminiferal calcite relative to Ca^{2+} is one-two orders of magnitude lower than that of inorganically precipitated calcite (Bentov and Erez, 2006) as illustrated in Figure 4.2. The culture experiments of Nürnberg et al. (1996) yielded the first Mg/Ca-temperature relationship. Mg/Ca of planktonic foraminifera have since been calibrated using core-top and sediment trap studies (Nürnberg, 1995; Elderfield and Ganssen, 2000; Lea et al., 2000; Dekens et al., 2002; Anand et al., 2003) and lab-culturing experiments where temperature variability can be isolated and facilitate more accurate calibrations to temperature (Nürnberg et al., 1996; Lea et al., 1999; Mashiotta et al. 1999) (see Barker et al., 2005 for an overview). Most of these studies showed a 9-10% exponential increase in Mg/Ca per degree Celsius in most of the planktonic foraminifera shells. The deviation from thermodynamic principles indicates that biogenic processes exert a major influence on the incorporation into the biogenic carbonates (Erez, 2003; Bentov and Erez, 2006; Lea et al., 1999; Rosenthal et al., 1997). Furthermore, temperature calibration equations deviate between species of planktonic foraminifera, with an example illustrated in Figure 4.2 for the planktonic species *Globigerina bulloides (G. bulloides)* and *Globigerinoides sacculifer (G. sacculifer)*.

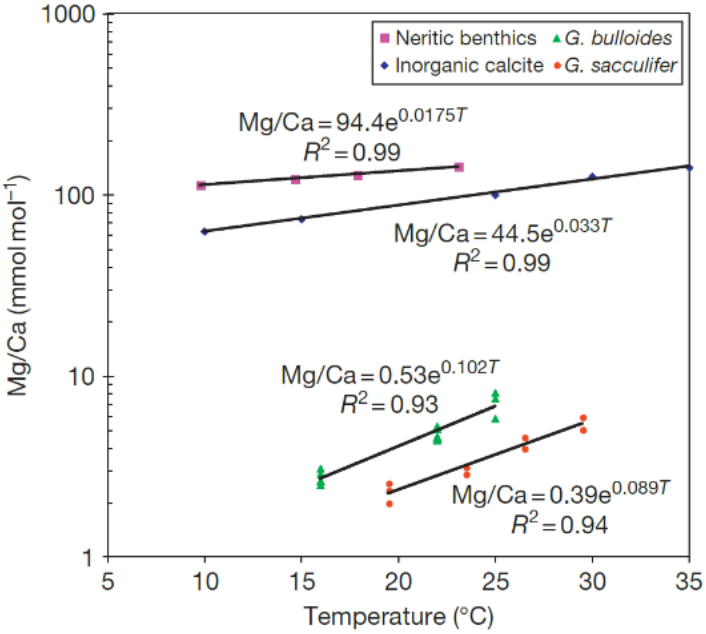

Figure 4.2: Calibration curves for two planktonic species, inorganic carbonate and neritic benthics. Planktonic foraminifera show higher sensitivity to temperature than inorganic carbonate and lower Mg incorporation. Also note the offset between the two planktonic species *G. bulloides* and *G. sacculifer.* Figure from Lea (2014).

Foraminiferal Mg/Ca dependence on temperature is expressed as an exponential relationship and fit to equations in the form of:

$$Mg/Ca\ (mmol/mol) = Be^{AT} \qquad \text{Equation 7}$$

Where T is the calcification temperature and B (pre-exponential) and A (exponential) are species-specific constants obtained through regression analysis. The exponential constant describes the sensitivity to temperature and is typically about 0.1, which equals 10% per degree Celsius.

As several genotypes of *N. pachyderma* have been identified (Darling et al, 2007) with characteristic geographical distribution and deviating temperature-calibrations (Riveiros et al., 2016), it is reasonable to use calibrations from the vicinity of the study area.

4.3.5 Secondary effects on measured Mg/Ca

Despite the robust relationship between calcification temperature and Mg/Ca ratio in foraminiferal calcite, other environmental influences may modulate Mg/Ca ratios in calcite and therefore the application of the proxy as a reliable paleothermometer. Some of these effects are related to post-depositional processes that contaminate the signal from the original calcification. Laboratory cleaning protocols are implemented on samples prior to measurement to limit the effects of contaminants on the Mg/Ca ratio. However, there may be primary influences on the elemental composition of foraminiferal calcite other than temperature that have implications for Mg/Ca thermometry.

4.3.5.1 Salinity

It is still uncertain to what extent salinity imposes an effect on the Mg/Ca ratio. Lab culture studies show a positive relationship between salinity and Mg/Ca (Nürnberg et al., 1996; Lea et al., 1999; Kisakürek, 2008; Arbuszewski et al., 2010). Core-top studies have shown biases towards higher Mg/Ca ratios in saline environments, one example being a +1,6°C bias per +1 psu change in the species *Globigerinoides ruber* assuming a Mg/Ca temperature response of 9% per degree Celsius (Mathien-Blard and Bassinot, 2009). Due to large uncertainties in the salinity-Mg/Ca relationship, the effects of salinity are difficult to quantitatively account for. Furthermore, *N. pachyderma* is known to avoid fresh water by inhabiting more saline subsurface water (Carstens et al., 1997) and large-scale salinity differences on the site may therefore only have indirect effects on Mg/Ca.

4.3.5.2 Dissolution effects

Core-top studies along a bathymetric transect show that post-depositional dissolution indicates a decrease in deposited planktonic foraminiferal calcite Mg/Ca with increasing water depth (Rosenthal and Boyle, 1993; Rosenthal et al., 2000; Dekens et al., 2002). This caveat long produced doubts to the usefulness of Mg/Ca as a paleothermometer (Lea, 2014). The decrease in Mg/Ca ratios of planktonic foraminifera is caused by preferential dissolution of Mg-rich calcite, which is more susceptible to dissolution (Brown and Elderfield, 1996). The rate of dissolution is related to the calcite saturation of seawater, or pore water fluid within sediments (Barker and Elderfield, 2002). The solubility of seawater is determined by temperature, pressure (and therefore depth) and carbonate chemistry with special attention to dissolved CO_2 concentrations. Deeper waters are therefore less saturated with respect to calcite and enables dissolution of calcite. Mg/Ca ratios are therefore decreasing with depth (Regenberg et al., 2014).

4.3.5.3 Carbonate chemistry, CO_3^{2-} and pH

Regenberg et al. (2014) determined a link between the preservation/dissolution pattern from 79 data sets in which Mg/Ca ratios were found to decrease below a threshold of CO_3^{2-} concentrations of 21.3 ±6.6 µmol/kg. The concentration of CO_3^{2-} is positively correlated to temperature in the North Atlantic and could therefore mute temperature reconstructions (Jonkers et al., 2013). The concentration of CO_3^{2-} is related to other inorganic carbon species by pH-driven chemical equilibria and thus pH should have an indirect effect on Mg/Ca precipitation/dissolution through its controls on the relative concentration of inorganic carbonate species. Lea et al. (1999) suggested that pH has a significant effect on the uptake of Mg in foraminiferal calcite. However, this effect is poorly quantified and is presumed to be species-dependent (Lea, 2014).

4.3.5.4 Diagenesis and post-depositional processes

The elemental composition of calcite within the sediments may be altered as calcite re-precipitates from pore fluid together with Mg-bearing Manganese/Iron oxides and hydroxides (Regenberg et al., 2007). Re-precipitated calcite may overwrite the Mg/Ca ratio that is produced during primary precipitation. Re-precipitated calcite reflects conditions within the sediments and not in the surface-subsurface environment considered in reconstructions using planktonic species. The effect does not scale to the relative amount of calcite in a sample that is re-precipitated: as Mg is preferentially dissolved, one can expect that re-precipitated calcite is enriched in Mg. Inorganic calcite that precipitates with much higher Mg/Ca ratios may lead to overestimations of temperature reconstructions.

In the suboxic zone in the sediment, Mn and Fe oxides are reduced to Mn and Fe ions that diffuse upwards where they re-precipitate as oxides when in contact with oxygen (Boyle, 1981; Pena et al., 2005). However, Mn^{2+} has also been implied to precipitates as manganese carbonate overgrowths in reducing sedimentary conditions (Boyle, 1983). Such overgrowths are impure with variable proportion of trace elements such as manganese, magnesium and iron (Pena et al., 2005) and therefore may act as contaminants in Mg/Ca analysis.

The most common clay minerals contain a significant amount of Mg (between 1-10%) and represent a significant proportion of marine sediment (Barker et al., 2003). Fine clay particles surround foraminiferal shells, but also enter the aperture and fills the chambers. Clay may also be contained within a matrix of organic matter (Barker et al., 2003). Organic matter itself contains Mg that may produce offsets in measurements. Clay and organic matter should therefore be removed from the sample to avoid contamination.

4.3.5.5 Barite contamination

Barium (Ba) may be present in several phases in marine sediments including Manganese/Iron oxides, carbonate and organic matter in variable extent. The main barium carriers are clays and barite ($BaSO_4$) (Gonneea and Paytan, 2006). Barite can precipitate in the water column, on the sea floor and within the sediments where barium encounters sulfate (Griffith and Paytan, 2012). Barite is commonly removed by diethylenetriaminepentaacetic acid (DTPA), $C_{14}H_{23}N_3O_{10}$, before trace element analysis of foraminifera, which is particularly important for Ba/Ca analysis used as a proxy for paleo- productivity (Lea and Boyle, 1993), but is also used in preparation for Mg/Ca analysis. Several elements are incorporated into barite and substituting for Ba (Griffith and Paytan, 2012), but there is little potential for Mg-substitution. Barite precipitated in seawater may contain some organic matter (Paytan et al., 2002)

4.4 Laboratory methods

A description of the laboratory methods used in this thesis will follow in this subchapter along with a brief description of the functioning of the instruments that were used.

4.4.1 Sampling

The GS15-198-36CC working half was sampled at EARTHLAB at the University of Bergen at 0.5 cm spacing intervals. Samples were then dried in a heating cabinet at 50°C. To remove clumps, the samples were put in distilled water and shaken overnight and were then wet sieved into the fractions >500 µm 150-500 µm, 63-150 µm and <63 µm. Again, the samples were dried in a heating cabinet at 50°C and the dry weight for all size-fractions larger than 63 µm was measured before samples were transferred into labelled vials.

4.4.2 Picking Foraminifera

Samples from the 500-150 µm size fraction were dry-sieved into three fractions: >212 µm, 150-212 µm and <150 µm. The planktonic species *N. pachyderma*, was selected from the 150-212 µm size fraction only. Only this narrow size fraction was selected to limit size effects, as Mg/Ca and other chemical properties, including stable isotopes, have been shown to be dependent on test size (e.g. Elderfield et al., 2002).

4.4.3 Sample preparation for stable isotope analysis

The optimal sample weight to make sure of complete reaction is 40-70 µg. Samples were therefore weighed to be within this range. 8-12 pristine specimens of *N. pachyderma* were generally appropriate for each sample run.

In an attempt to remove contaminants before analysis, the foraminifera shells were popped open by use of a clean glass rod and 3-4 drops of methanol was added to each sample. The vials containing the samples were subsequently put in an ultrasonic bath for 5-10 seconds to suspend fine-fraction contaminants. Without touching the sample, the easily accessible methanol with suspended material was extracted by use of a syringe. Samples were then dried in a heating cabinet at 50°C to ensure evaporation of remaining methanol.

4.4.4 Mass Spectrometry

Analysis of stable isotopes of oxygen and carbon was performed by use of a Thermo Finnigan MAT253 gas source mass spectrometer at FARLAB, UiB. The instrument determines the mass ratios of gases and since the sample $CaCO_3$ produces CO_2 when exposed to acid, stable isotopes of both carbon and oxygen may be determined simultaneously. A Kiel IV Carbonate Device is coupled to the mass spectrometer and injects phosphoric acid into the vials containing the sample at 70°C producing CO_2 by the following reaction:

$CaCO_3 + H_3PO_4 \rightleftharpoons CaHPO_4 + CO_2 + H_2O$ Equation 8 (Hoefs, 2009)

The CO_2 is next injected into the mass spectrometer. As Equation 8 shows, carbon in the produced CO_2 comes directly from carbon in the sample and $\delta^{13}C$ may therefore be measure directly. Phosphoric acid is used to make sure that there is no exchange of oxygen between the acid and the products (Clark and Fritz, 1997) and thus the oxygen in the products stem from the sample and are divided by 2/3 into CO_2 and 1/ into H_2O.

The mass spectrometer consists of three main parts; the source of ions, the electromagnetic analyzer, and the ion detectors as schematically illustrated in Figure 4.3. The gas is ionized in the ion source and accelerated and focus as a beam towards the analyzer. The electromagnetic field in the analyzer deflect the path of the ions giving to their mass/charge ratio and the ions thus leave the analyzer in separate beams. Detectors are placed according to the predicted paths of the mass of ions analyzed (Hoefs, 2018). In the case for CO_2, beams with the mass 44 (^{12}C, ^{16}O, ^{16}O), mass 45 (^{13}C, ^{16}O, ^{16}O) or (^{12}C, ^{17}O, ^{16}O) and mass 46 (^{14}C, ^{16}O, ^{18}O) or (^{12}C, ^{17}O, ^{17}O) or (^{13}C, ^{17}O, ^{16}O) are collected and counted by the detectors allowing the determination of the mass ratios 46/44 and 45/44.

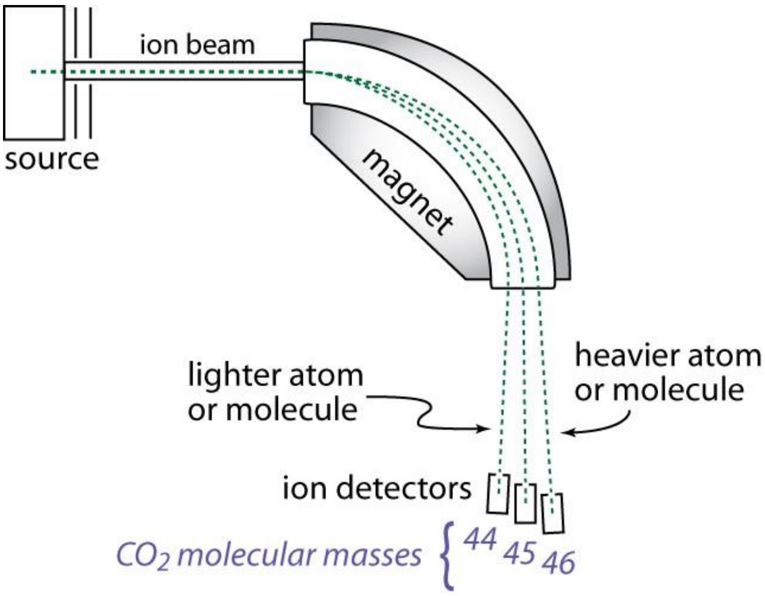

Figure 4.3: Schematic illustration of the components and functioning in a gas sources mass spectrometer. Figure from Dunn (2016).

4.4.5 Standards for isotope measurements

To accurately measure the absolute abundance of minor isotopes is a vast analytical challenge and the problem is bypassed by comparing measured values in the samples to measured standards with known isotopic composition. Thus, a relative estimation of the isotopic composition in the sample is attained.

To enable comparisons of measurements from different labs, isotopic ratios of carbon and oxygen from carbonate are reported against the internationally recognized Vienna Pee Dee Belemnite (VPDB) standard that is provided by the International Atomic Energy Agency (IAEA).

To not deplete the international standard, laboratories use reference standards that has a known value on the VDPB scale. The original PDB standard was spent requiring the VPDB standard to be developed. To quantify drift and precision of measurements, laboratories develop their own working standards that are calibrated to the reference standard. In this study, the working standard Cararra Marble 12 (CM12) was used and weighed to include the weight-range of the samples (40-67 µg). Based on the CM12 measurements, the external precision during the runs were equal to or better than 0.03 and 0.06 (1 sigma) for carbon and oxygen isotopes respectively. The working standard was calibrated to the VPDB scale using the reference standard NBS-18 from the National Bureau of Standards, which has a known isotopic value relative to the VPDB ($\delta^{13}C$ VPDB = -5.014‰ and $\delta^{18}O$ VPDB = -23.2‰) (IAEA, 1995)

4.4.6 Sample preparation for Mg/Ca measurement

Foraminiferal calcite is susceptible to contamination by phases added to the tests post-mortem, including contamination from organic material or clays or post depositional overgrowths (Boyle, 1981). Such contaminants may produce bias in elemental ratios and should therefore be removed from the sample to extract a clean Mg/Ca signal. Three main cleaning procedures have been developed and used in preparation of foraminiferal samples for trace element analysis: (1) "Mg-cleaning", (2) "Cd-cleaning", and (3) "full-cleaning" (Elderfield and Ganssen, 2000; Boyle and Keigwin, 1985; Martin and Lea, 2002). The "Mg-cleaning" method includes removal of clays by distilled water and methanol, oxidation of organic matter by hydrogen peroxide (H_2O_2), and an acid leaching step by using diluted nitric acid (HNO_3) to remove absorbed contaminants. In the "Cd-cleaning" method, a reductive step is added to the "Mg-cleaning" to remove Mn-Fe oxide coatings by anhydrous hydrazine. The "full-cleaning" method includes an additional step of barite removal by DTPA solution.

There is a current debate to whether the reductive step is needed, or even counterproductive in Mg/Ca analysis due to hydrazine causing partial dissolution of sample carbonate (Hasenfratz et al., 2017). Indeed, the reductive step has been shown to systematically lower Mg/Ca ratios by 10-15% (Barker et al., 2003). On the other hand, detailed studies on individual tests have revealed that Mg-rich $MnCO_3$ overgrowths (Pena et al., 2005) and high Mg, Fe and Mn overgrowths thought to be Mn-Fe oxides (Pena et al., 2008) may be present and should be removed. Furthermore, a cleaning method where contaminant phases are leached and measured after each step have showed Mg-rich Mn-oxide coatings on foraminifera emphasizing the importance of the reductive step in Mg/Ca analysis (Haley and Klinkhammer, 2002).

DTPA solution was first used by Lea and Boyle (1993) to remove barite contamination in foraminiferal calcite in analysis of barium concentrations in primary calcite. In Ba/Ca analysis, the DTPA-step has been shown to be important as the reagent removes barite ($BaSO_4$) contamination (Lea and Boyle, 1993; Haley and Klinkhammer, 2002). However, the use of DTPA solution as a cleaning reagent of small samples requires great care because DTPA solution is aggressive to other chemical species and readily dissolves calcite. Like the reductive step, preferential dissolution of magnesium may be expected. Barite is not associated with high-magnesium content, unlike other contaminant phases that are removed prior to Mg/Ca analysis. One advantage of using the "full-cleaning" method is therefore the possibility to also include Ba/Ca records as all elements are measured simultaneously.

Approximately 200, constituting approximately 1 mg, specimens of *N. pachyderma* in the size fraction 150-212 µm were selected and crushed between two glass plates. Contaminants were carefully removed when seen under the microscope. Then, samples were transferred into acid-leached vials.

This approach was adopted to maximize the number of shells involved and therefore the analyses' representativeness of the foraminiferal population.

The cleaning procedure performed in this study is modified from an adapted method version of the School of Earth and Ocean Sciences at Cardiff University based on Barker et al. (2003), Boyle (1981) and Lea and Boyle (1993) that includes a barite-removal step by using DTPA solution and omitting contaminant check steps (S. Bates, pers. com, 2016) and instead the samples were centrifuged after dissolution (10 min, 10000 rpm) to separate any insoluble particles.

All samples underwent clay removal by water and methanol cleaning, a reductive step to remove metal oxides, an oxidative step to remove organic matter, sample transfer to new vials, and a dilute acid rinse to remove remaining absorbed contaminants. Samples were split after the oxidative step. Thus, one set of samples were measured after the following protocol and the second set underwent equal treatment, except for the omitted barite removal. One objective of this work was to test two different cleaning protocols prior to analysis, the "Cd-cleaning" and the "full-cleaning" methods. The detailed cleaning protocol used here is attached in Appendix A.

4.4.7 Optical Spectrometry

Trace element analysis of *N. pachyderma* was performed by use of an Agilent 720 ICP-OES at the Trace Element Lab (TELab) at UNI Research Climate.

The ICP-OES instrument consists of two main parts: the induced coupled plasma (ICP) and the optical emission spectrometer (OES). Sample solution is transported by a peristaltic pump into a nebulizer that creates a mist of fine droplets of the sample that is injected into a spray chamber. The instrument measures each sample six times each run to create an average measurement. Argon 5.0 (99.9999% argon) is injected into the nebulizer and through an induction coil that produces a radiofrequency which ignites the argon to produce plasma. Argon gas is used for this purpose to avoid interference in subsequent elemental detection. As the sample solution is introduced to the plasma, the compounds are ionized and excited to a higher state. Light characteristic to specific elements is emitted when the ions return to their ground state. The emitted light moves through an opening and into the optical emission spectrometer where it passes through lenses before it reaches the detector. Specific combinations of wavelengths that characterizes individual elements are detected. The intensity of each combination of wavelengths correspond to the concentration of the element.

Each sample was dissolved in 0.1M trace metal pure nitric acid (HNO_3) to reach a calcium dilution of 40 ppm. Sample concentrations are kept uniform and cross referenced with standards of equal Ca-concentration reduce matrix effects (Rosenthal et al., 1999). Six in-house standards were measured at the end of the run with a range of compositions similar to modern foraminifera (0.5-7.66mmol/mol). A quality check with the Mg/Ca ratio of 5.076 mmol/mol was measured every eight sample, to a total of 44 times, to maintain control over potential analytical drift and to calculate long-term analytical precision. Long-term analytical precision was calculated to be 1σ= 0.020 mmol/mol. Mg/Ca of long-term international limestone standard (ECRM752-1) measurement is 3.76 mmol/mol 1σ=0.07 mmol/mol and the average published value of 3.75 mmol/mol (Greaves et al., 2008).

5 Results

The interval 285-340 cm in core GS15-198-36CC covers the onset of GI9 until the gradual cooling of GI8 with high sedimentation rates and continuous deposition of *N. pachyderma* thus allowing high-resolution studies of near-surface water masses.

In the following subchapters, I briefly describe the core section used for this work. Then, I present differences of *N. pachyderma* Mg/Ca using the two different cleaning protocols and thereafter, the results from subsequent temperature reconstructions and stable isotope analysis.

5.1 Core section description

The core has been visually described on board the ship after coring. Over the interval covered in this thesis the core is quite homogenously consisting of silty clay (Figure 5.1). The interval 273 cm to 310 cm is described as “dark-gray-brown silty clay” with an anomalously dry interval between 280 cm and 290 cm. The interval between 310 cm and 322 cm is described as “olive-dark-gray silty clay”. Between 322 cm and 450 cm, the core is described as “dark gray, silty clay”.

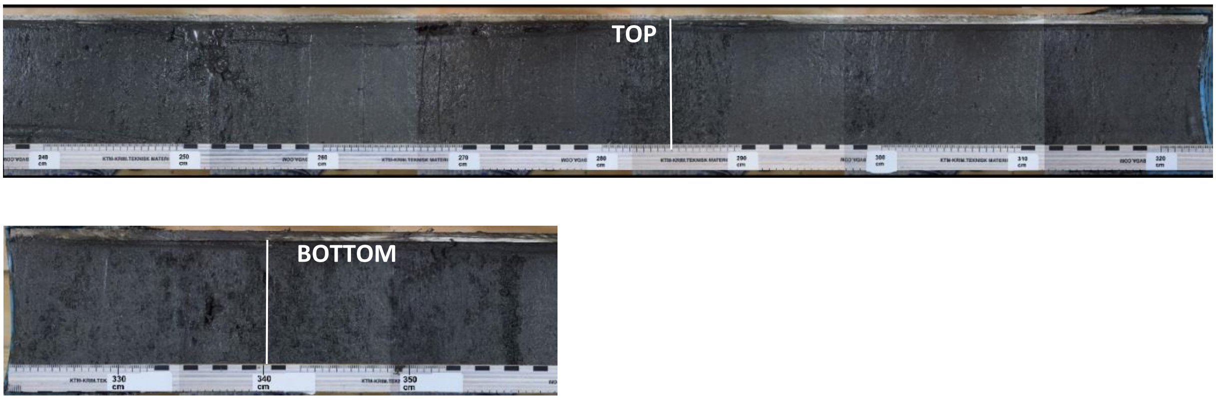

Figure 5.1: Collection of images of core section 3 (240-322.5 cm) above and core section 4 (322.5-350 cm) below, including all materials used in this thesis. White lines indicate the core interval studied here with top (285 cm) and bottom (340.5 cm). The strong horizontal (to the core) color shifts approximately every 10 cm apparent in the Figure are due to merging of individual images.

5.2 Element Analysis

Samples with high ratios of Mg/Ca or (average + 2 sigma) were replicated when sufficient sample material was available. 21 samples were replicated in total, 8 cleaned with “Cd-cleaning” method and 13 with the “full-cleaning” method. Replicated measurements with significantly lower contaminant values replaced original data. Replicates and original measurements were averaged when deemed indistinguishable in terms of quality. Three data points, all from the “Cd-cleaning” method, were discarded due to exceptionally high values of Fe/Ca (> 2000 µmol/mol) and Al/Ca (> 1000 µmol/mol).

5.2.1 Results from different cleaning protocols

In order to remove different chemical elements that may contaminate the samples, two different cleaning procedures have been used prior the Mg/Ca analysis (see section 4.6 and appendix for details). Here, I present results of elemental ratios that give indications to the degree of contamination and to what extent the added DTPA step alters elemental ratios in samples. The downcore Mg/Ca results from the "Cd-cleaning" and the "full-cleaning" methods are compared in Figure 5.2, along with Fe/Ca, Al/Ca, Mn/Ca, and Ba/Ca, monitoring the possible contamination. The effect of DTPA step on trace element concentration is shown in Figure 5.3 and the relationship between contaminant concentrations and Mg/Ca in Figure 5.4. All correlations described are determined by regression analysis and the coefficient of determination (R^2).

5.2.1.1 Mg/Ca

Plotting measured Mg/Ca on depth (Figure 5.2.a) illustrates the downcore variability. The downcore Mg/Ca ratios from the “full-cleaning” method generally follow the same trends as the “Cd-cleaning” method. This includes an increase in Mg/Ca values from 335-330 cm depth, a high plateau between 335-320 cm, a synchronous depletion of Mg/Ca from ~320 cm, and synchronized fluctuations on a low Mg/Ca baseline between 310 cm and 285 cm.

The range of Mg/Ca values is between 0.39-0.73 mmol/mol using the “full-cleaning method”. The range using the “Cd-cleaning” method is between 0.42 mmol/mol to 0.87 mmol/mol including outliers. Results of samples cleaned by the "Cd-cleaning" method present higher peaks, larger spread and are more shifted towards the higher end of the Mg/Ca range (Figure 5.2a). Figure 5.3 illustrates that there is a correlation (R^2=0.22) between the Mg/Ca ratios from both cleaning methods, but generally the samples cleaned with the “full-cleaning” method yield lower Mg/Ca values than the “Cd-cleaning method”. On average, samples cleaned by the “full-cleaning” method have 7.8% lower Mg/Ca values than samples cleaned by the “Cd-cleaning” method. Interestingly, lowered values are systematic downcore below ~307 cm, but almost completely absent above 307 cm.

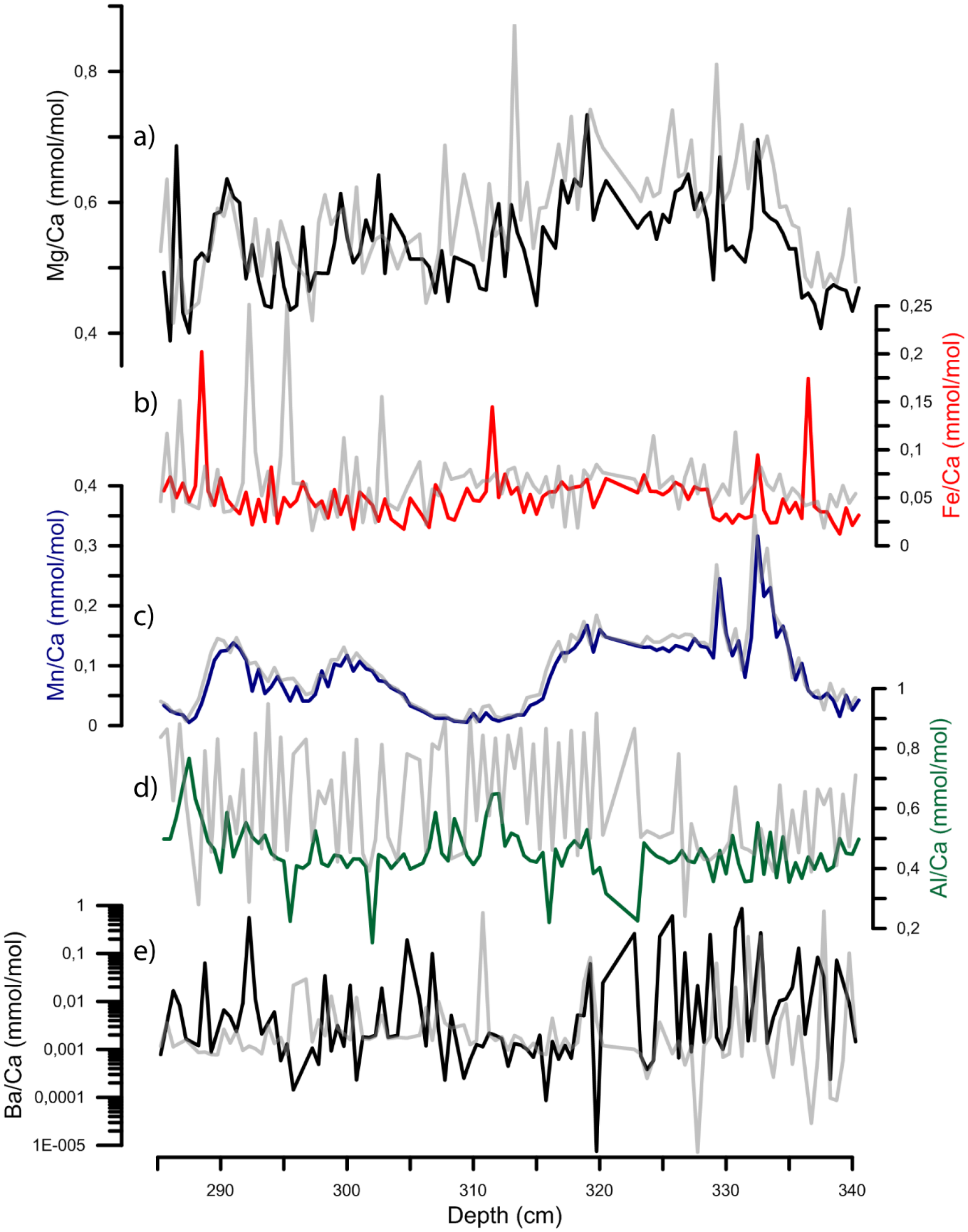

Figure 5.2: Measured element ratios at core depth (cm). Colored graphs in front are measured element ratios with a) Mg/Ca, b) Fe/Ca (red), c) Mn/Ca (blue), d) Al/Ca (green), e) Ba/Ca (black in the bottom), the "full-cleaning" protocol (using DTPA solution). Grey graphs are the respective downcore elemental ratios after the "Cd-cleaning" (without using DTPA solution). All ratios are denoted in mmol/mol. Note the logarithmic scale for Ba/Ca.

5.2.1.2 Fe/Ca

DTPA-treated samples generally range between Fe/Ca= 0.02-0.07 20-70 µmol/mol whereas non-DTPA treated samples have slightly elevated Fe/Ca in the range 20-120 µmol/mol (Figure 1.2). Fe/Ca is on average 50 µmol/mol and 66 µmol/mol for DTPA-treated and non-DTPA-treated samples respectively, yielding a difference of 24.2 %. The fluctuations of Fe/Ca are decrease downcore after DTPA-treatment as seen in Figure 5.2. Sporadic spikes (>150 µmol/mol) that are still in the dataset were not rejected as they do not correspond to either elevated Mg/Ca or spikes in other contaminants.

Downcore Fe/Ca is less noisy for samples subjected to the “full-cleaning” method. Higher Fe/Ca for DTPA treated samples, about 20 µmol/mol above average, are associated to the high Mg/Ca plateau at ~335-320 cm (Figure 5.2). Generally, Fe/Ca and Mg/Ca correlation is low for both cleaning methods, with R^2=0.019 and 0.009 for non-DTPA and DTPA-treated samples respectively (Figure 5.4). The “full-cleaning” method decreases the relationship between Mg/Ca and Fe/Ca.

5.2.1.3 Al/Ca

Downcore Al/Ca ratios after the “Cd-cleaning” method fluctuate between of 400 and ~800 µmol/mol. The range of Al concentration after the “full-cleaning” method is lower: between 350-650 µmol/mol. Average Al/Ca are 450 µmol/mol and 610 µmol/mol for DTPA and non-DTPA treated samples respectively, with an average reduction of 26.2% Al/Ca after the “full-cleaning” method. Figure 5.4 illustrates that the correlation between Al/Ca and Mg/Ca is low, with R^2=0.0002 and 0.0009 after the “full-cleaning” and the “Cd-cleaning” methods respectively with slopes of -0.02 and 0.06. It also shows that DTPA treatment systematically lowers high (~800 µmol/mol) Al/Ca to values of ~400 µmol/mol.

5.2.1.4 Mn/Ca

Mn/Ca ratios range from 1 µmol/mol to 350 µmol/mol. Downcore values for DTPA and non-DTPA treatment is visually comparable by following the same trends. Figure 5.3 illustrates the similarity between DTPA and non-DTPA steps for Mn/Ca are correlated by an R^2=0.97. The “full cleaning” method lowers the Mn/Ca ratios by 12.5% with average concentrations of 96 µmol/mol and 84 µmol/mol for non-DTPA and DTPA treatment respectively.

Mn/Ca values co-vary with Mg/Ca after both treatments, albeit with a higher correlation after DTPA treatment with R^2=0.38 and R^2=0.29 without DTPA solution (Figure 5.3) and slopes of 0.53 and 0.41. The correlation is apparent in Figure 5.2 where high Mn/Ca values correspond to high Mg/Ca and vice versa. The variability in Mn/Ca is larger than Mg/Ca, with variability over two orders of magnitude. Mg/Ca below 0.5 mmol/mol is associated with very low Mn/Ca (<20 µmol/mol). The highest peaks in Mn/Ca are associated with the initial downcore Mg/Ca increase between ~335-330 cm (Figure 5.2). These values are above the 105 µmol/mol limit as determined by Boyle (1983).

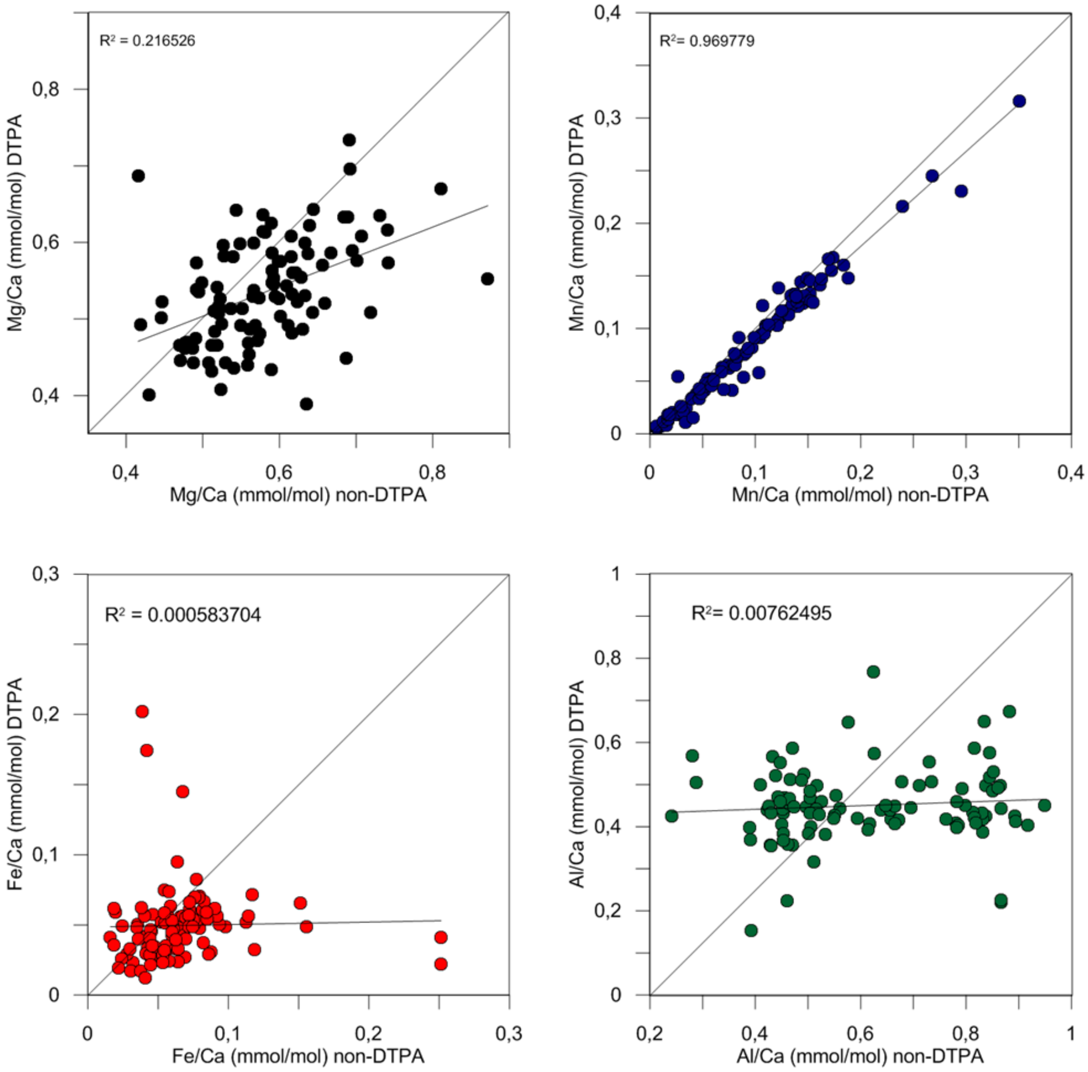

Figure 5.3: Measured element ratios after adding DTPA-treatment of Mg/Ca, Mn/Ca, Fe/Ca and Al/Ca plotted against the same measurements without DTPA-treatment. Best linear fit is included.

5.2.1.5 Ba/Ca

Ba/Ca ratios are significantly lower and more fluctuating than concentrations of the trace elements discussed above. Measured values after both cleaning protocols vary from 0.1 to 800 µmol/mol and are thus plotted on a logarithmic scale in Figure 5.2 and Figure 5.4. Average ratios are low: 44 µmol/mol and 23 µmol/mol after the “full-cleaning” and the “Cd-cleaning” methods respectively. These measured values are close to the detection limit of the instrument ICP-OES and I will therefore not go into further detail regarding Ba concentrations.

5.2.1.6 Summary

Mg/Ca ratios vary independently of Al/Ca, Fe/Ca and Ba/Ca which indicate that their associated contaminant phases are not exerting important controls on the Mg/Ca ratios. In that respect, Mn/Ca is different by co-varying with Mg/Ca values downcore. The Mn/Ca values are largely below or close to the 105 µmol/mol contamination limit determined by Boyle (1983), which suggests that contamination by Mn-phases do not control the Mg/Ca values. Between ~335-330 cm depth, however, Mn/Ca values are above this level irrespective of cleaning method and temperature estimations from Mg/Ca in this interval should be treated with care. Overall, the “full-cleaning” method lowers contaminant values and reduces the relationship with Mg/Ca. On that note, I continue with the Mg/Ca temperature reconstruction using the samples subjected to the “full-cleaning” method.

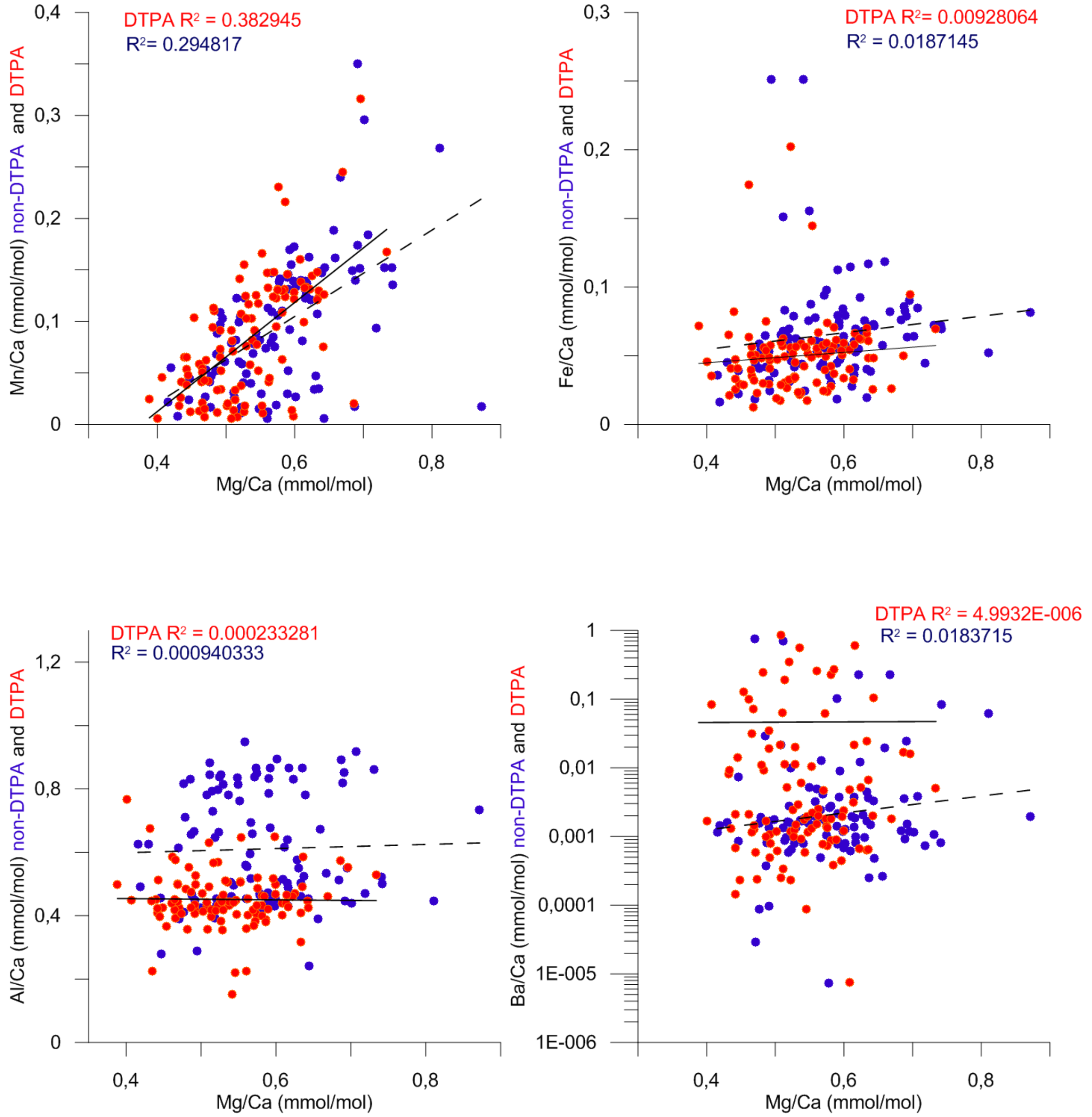

Figure 5.4: Contaminant ratios (Mn/Ca, Fe/Ca, Al/Ca, and Ba/Ca) after DTPA-treatment (Red) and without DTPA-treatment (blue) plotted against Mg/Ca ratios for corresponding sample cleaning process. Solid linear fit corresponds to DTPA-treated samples and dashed line to fit for non-DTPA treatment. Note logarithmic scale on Ba/Ca.

5.3 Temperature reconstruction

5.3.1 Temperature calibration

Samples cleaned by the “full-cleaning” method are chosen for temperature reconstruction due to generally lower contaminant values and lower correlation with contaminants. The temperature calibration equation used in this study is based on the empirical calibration from Elderfield and Gansen (2000) for *N. pachyderma*, with a modified pre-exponential constant calibrated to core tops in the southern Norwegian Sea by Ezat et al. (2016):

Mg/Ca (mmol/mol) $= 0.4e^{0.1T}$ Equation 9

Elderfield and Ganssen (2000), using the Mg-cleaning method, calculated a pre-exponential constant of 0.50 for *N. Pachyderma*. Ezat et al. (2016) found that the full-cleaning methods, also used in this study, lowered Mg/Ca by 10-50% compared to the Mg-cleaning method.

Core-top calculated temperatures are 5.48°C, 6.58°C, 7.44°C, and 7.76°C which are plotted on the temperature profile on the conductivity- temperature-depth (CTD) profile in Figure 5.5. Calculated core-top temperatures are assumed to reflect modern conditions and the validity of the Mg/Ca to temperature calibration may be evaluated by comparing them to measured seawater temperatures. Core-top foraminifera were not dated, but they were stained with Rose Bengal so we can cautiously claim that they are representative of modern conditions (Bernard et al., 2006). Two of the core-tops fall in the range of temperatures found shallower than ~100 meters water depth, consistent with calcification in the near-surface environment. Two core-tops calculated temperature suggest warmer temperatures than measured in the water column. However, including the standard error of ±0.6°C associated with the temperature calibration equation (Elderfield and Ganssen, 2000) puts these core-top calculated temperatures very close to modern surface temperatures from the CTD. It is worth noting that measured CTD may not be representative because it was measured during a single day at the core location where conditions are susceptible to changes as the site is close to frontal areas (Figure 3.3). Based on interpolations of GLODAPv2 data points over the summer season (Figure 3.1 and 3.2.b) the reconstructed core-top temperatures are within a reasonable temperature range under influence of Atlantic Waters at the site.

5.3.2 Reconstructed temperature from Mg/Ca

Figure 5.6.a) shows reconstructed temperatures from Mg/Ca in *N. pachyderma* plotted versus depth (in cm). Uncertainty introduced by the Mg/Ca- temperature calibration equation is ±0.6°C (Elderfield and Ganssen, 2000). Long term analytical precision during the runs was ±0.020 mmol/mol (1σ). The

combined uncertainty from instrumental precision and temperature calibration equation (±0.0085 in the pre-exponential constant) is represented by shaded error in Figure 5.6.a). Uncertainty related to replicability of samples was not quantified, as only samples that were assumed to be contaminated were replicated. Because each sample contained a split total of ~200 specimens of *N. pachyderma,* replicability is presumably quite high. A high number of specimens increases the representability of the sample by limiting variability within the foraminiferal group related to seasonality, outliers in terms in depth habitat, or errors in species determination.

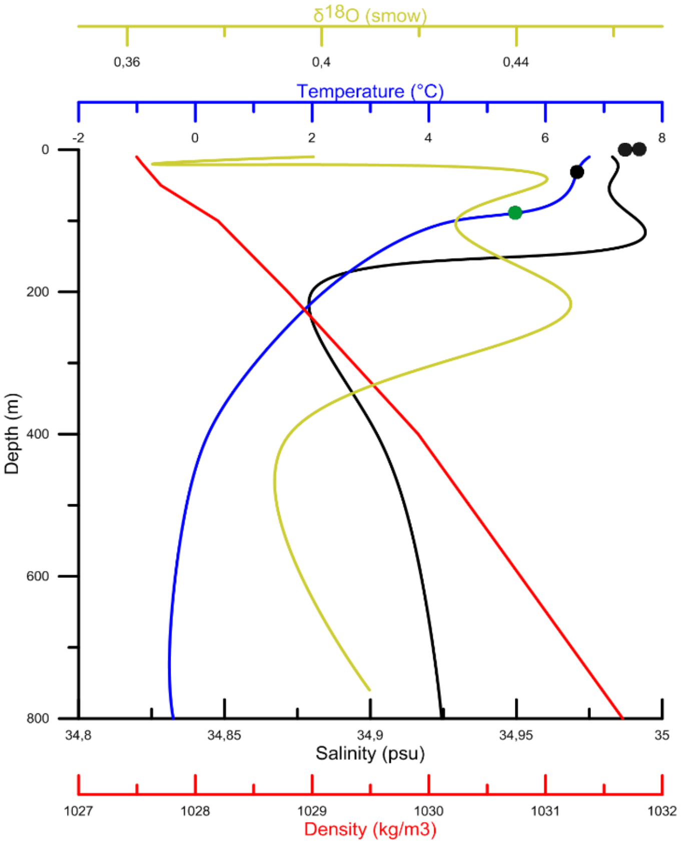

Figure 5.5: Spline smoothed CTD profile from core-location July 26. 2015 with temperature in blue, salinity in black, density in red and $\delta^{18}O$ (smow) in yellow. Dots plotted on the temperature scale represent core top temperatures calibrated from the equation Mg/Ca (mmol/mol) $= 0.4e^{0.1T}$. Black dots are core tops from the depth interval 0.5-1 cm and the green from 0-0.5cm. Measurements are from water depths 10, 20, 50, 100, 200, 400 and 800 m (760 m for $\delta^{18}O$ (smow)).

Reconstructed temperatures from *N. pachyderma* ranges from -0.30°C to 6.07°C with a total amplitude of 6.37°C. The temperature record consists of four main phases that correlate downcore variations in $\delta^{18}O$ and $\delta^{13}C$ as illustrated in Figure 5.6 and summarized in table 5.1: (1) cold waters (~1°C) (A) before abrupt warming to ~5°C and a short cooling phase (B) until temperatures rise again (C). (2) a phase of relatively warm and stable conditions between 327 and 317 cm characterized by a gradual warming towards the maximum recorded temperatures of >5°C, (3) Cooling from about 317 cm to 310 cm from maximum values towards ~1°C. Abrupt cooling occurs between 317-315 cm before temperatures rise

~2°C before dropping back to ~1°C, at ~310 cm. (4) A phase of oscillating temperatures with increasing amplitude on a cold baseline between 310 cm and 285 cm. The temperature changes in Phase 1 and 3 are larger than the uncertainty introduced by the Mg/Ca-temperature calibration equation. The oscillations in Phase 4, and after the abrupt temperature drop in Phase 3, are of an amplitude of 2-3°C; also larger than the uncertainty related to the temperature calibration.

5.3.3 Oxygen isotope results

The *N. pachyderma* δ^{18}O record amount to near-surface variations in temperature and the isotopic composition in the ambient seawater during calcification. Lighter δ^{18}O indicates warmer conditions and fresher water and vice versa. Figure 5.6.b) shows the δ^{18}O (‰) record from *N. pachyderma* plotted versus depth. External precision during the runs was equal to or better than 0.06‰ (1σ), represented by error bars in Figure 5.6.b). No samples were replicated and no attempts to quantify replicability were made. As only 8-12 specimens were used for each run, contaminated specimens or species recognition errors may lead to deviations.

The *N. pachyderma* oxygen isotope record ranges from 2.68‰ to 5.42‰, a total variability of 2.74‰. However, this total variability is probably overstated due to a few extreme points deviating significantly from the trend. Ignoring points at 334.25 cm, 332.25 cm, and 329.75 cm yields a total variability of 2.06‰. The main feature of the δ^{18}O record is a phase of relatively light isotopic composition between 327 cm and 317 cm, during Phase 2. δ^{18}O changes from values close to maxima to minima over an interval of two centimeters during Phase 1C. Similarly, the subsequent enrichment at the end of the ^{18}O depleted interval occurring between 317-310 cm. Up-core from the transition, δ^{18}O remain stable at ~4-4.2‰ until a further enrichment of heavy isotopes is recorded between 289-285 cm.

There are clear similarities between the records of reconstructed temperature and δ^{18}O and the δ^{13}C. The most striking similarity is the coinciding enrichment in heavy isotopes and cooling described in Phase 3 at 317cm. The cooling comes after temperature maxima and enrichment of heavy isotopes after δ^{18}O minima. In Phase 4, oxygen isotopes remain stable during large oscillations in reconstructed temperature. The warming described in Phase 1 coincides with stable, even a slight enrichment of the heavy isotope. The depletion of the heavy isotope at 329-327 cm coincide with a small warming.

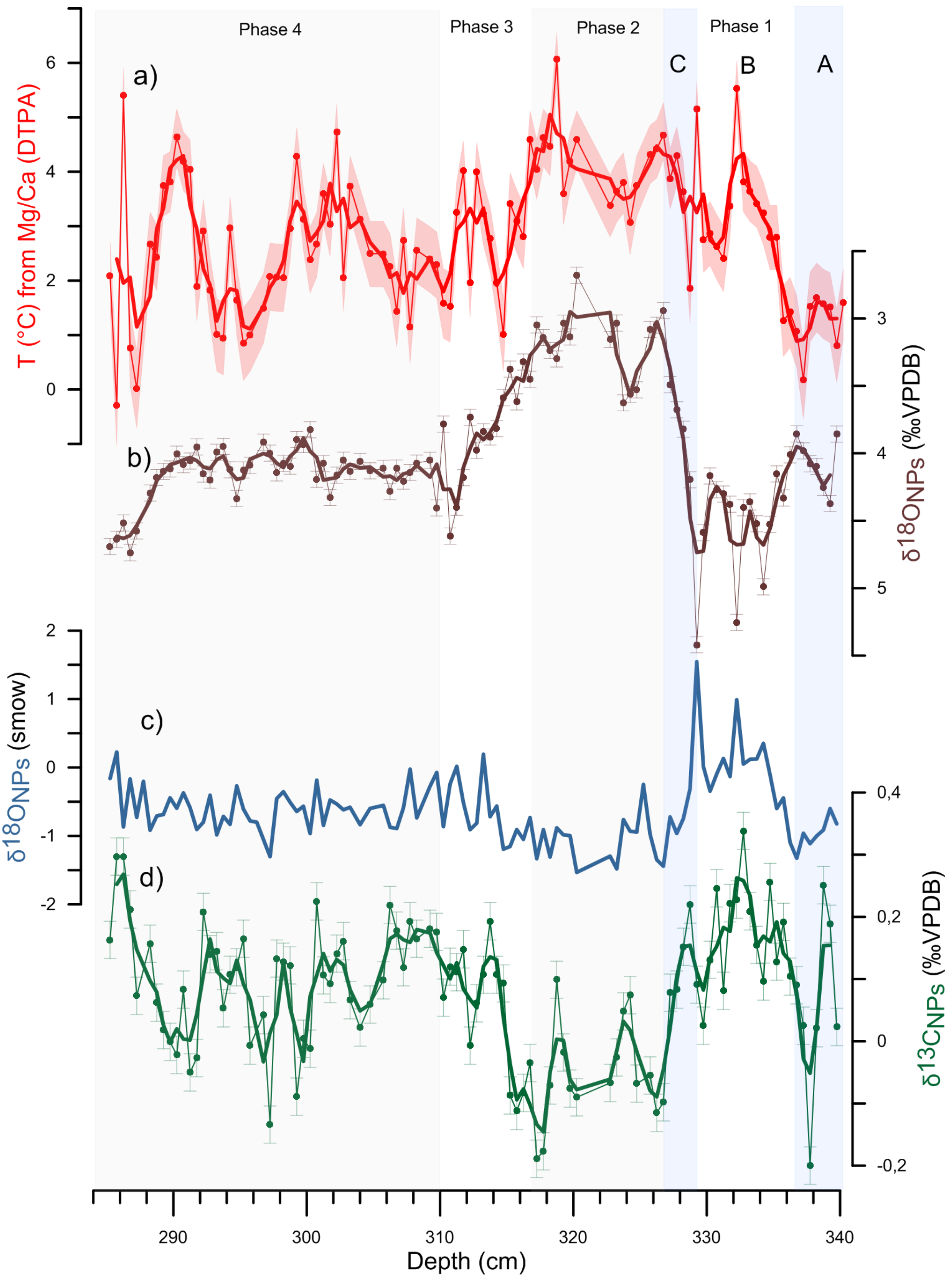

Figure 5.6: Downcore data sets from GS15-198-36CC plotted against depth with phases described in the text. Thick lines represent 3-point running averages. Note that interval 320.5-322.5 cm is missing. (a) Reconstructed temperature (°C) with all 104data points. The shaded area represents error from long-term analytical precision (±0.020mmol/mol) and uncertainty introduced by the Mg/Ca-temperature calibration equation (±0.0085 in the pre-exponential constant). The high point at 286.25 cm is not associated with high indicators of contaminations. (b) *N. pachyderma* $\delta^{18}O$ record relative to VDPB plotted with all 106 data points. Error bars illustrate external precision ±0.06‰ (1σ). Also note the reversed scale for $\delta^{18}O$. (c) Calculated near-surface $\delta^{18}O$(smow) as described in the text. (d) *N. pachyderma* $\delta^{13}C$ record relative to VDPB plotted with all 106 data points. Error bars illustrate external precision ±0.03‰ (1σ).

5.3.3.1 $\delta^{18}O_{sw}$

As described in subchapter 4.3.2.1., the isotopic composition of seawater may be estimated using an independent temperature proxy to account for the temperature effect on $\delta^{18}O$ and has here been calculated by Equation 4.5.

The isotopic composition of seawater is related to salinity, as both are influenced by the hydrographical balance. As illustrated in Figure 5, the modern local relationship between salinity and $\delta^{18}O_{sw}$ is detached in the depth-profile from the coring site. The isotopic composition of seawater is correlated to water masses in addition to the large-scale salinity/$\delta^{18}O_{sw}$ relationship. Surface waters in the Denmark Strait are influenced primarily by Atlantic Waters and Polar Waters which have distinctly different properties reflected by $\delta^{18}O_{sw}$. Thus, $\delta^{18}O_{sw}$ reconstructions may provide valuable information of the junction of these different water masses.

Figure 5.5.c) shows the $\delta^{18}O_{sw}$ record plotted on depth that ranges from 1.54‰ to -1.53‰, with a total variability of 3.07‰. Excluding the outliers in Phase 1, the range is halved. The overall record resembles $\delta^{18}O_{calcite}$, with the lowest values in Phase 2, higher values in Phase 1 and 4 and a transition in Phase 3.

Uncertainty in the $\delta^{18}O_{sw}$ calculation (not plotted here) are propagated from uncertainty both in the temperature reconstruction and in $\delta^{18}O$ measurement.

5.3.4 Carbon isotope results

Figure 5.6.d) shows the $\delta^{13}C$ (‰) record from *N. pachyderma* plotted versus depth. Instrumental precision during the analyses was equal to or better than 0.03‰ (1σ), represented by error bars in Figure 5.6.d). No attempts to quantify replicability were made. As with oxygen isotopes, the low number of specimens used in stable isotope analysis may lead to offsets even if only some individual tests are contaminated.

The carbon isotope signal is related to the productivity/respiration balance due to biological preferential uptake of the light isotope (Ravelo and Hillaire-Marcel, 2007). $\delta^{13}C$ decreases with age when water masses are isolated form the mixed surface layer due to gradual decomposition of organic matter and may therefore be used to track ventilation changes.

The *N. pachyderma* carbon isotope record ranges from -0.20‰ to 0.34‰, a total variability of 0.54‰. The amplitude variations are smaller for $\delta^{13}C$ than $\delta^{18}O$, but the two records co-vary positively downcore. $\delta^{13}C$ measurements plotted against $\delta^{18}O$ yields a linear relationship with R^2=0.43, illustrating the correlation. The most depleted of the core section with respect to heavy carbon isotopes corresponds to the interval with most depleted $\delta^{18}O$ between 327 cm and 317 cm. The transition into, and out of, this interval are synchronous in the two isotopic records. In the subsequent

Phase 4, δ^{13}C values fluctuate with variations up to 0.2‰. These changes are synchronous with temperature variations where warm temperatures coincide with lowered δ^{13}C. Throughout the section, δ^{13}C and reconstructed temperature are negatively correlated, except in Phase 1 A-B where δ^{13}C is enriched together with increasing temperatures.

Table 5.1: Summary of the downcore evolution in reconstructed temperatures, δ^{18}O, and δ^{13}C presented in the Phases described in the text.

Phase		Description
1 (340-327cm)		Overall warming of near-surface waters followed by depletion of ^{18}O and ^{13}C.
	A.	Low temperatures (~1°C), δ^{18}O=~4‰.
	B.	Warming and lower δ^{18}O.
	C.	Depletion of ^{18}O from ~4.5‰ to 3‰, depletion of ^{13}C from ~0.2 to -0.1‰.
2 (327-317cm)	-	High temperatures that are gradually increasing increasing (4-5°C).
	-	Low and gradually decreasing δ^{13}C.
	-	Low δ^{18}O.
3 (317-310cm)	-	Subsurface temperatures drop from 4-5°C to 2-3°C between 317-315 cm followed by short-lived warming.
	-	Enrichment of ^{18}O from 3 to 4‰.
	-	Enrichment of ^{13}C from -0.1 to 0.2‰.
4 (310- 285cm)	-	Colder temperatures but with warmer phases (3-4°C)
	-	Low δ^{13}C. Higher temperatures coincide with lower δ^{13}C.
	-	High and stable δ^{18}O.

6 Chronology

Core GS15-196-36CC was retrieved in close proximity to core PS2644-5 (67°52.02'N, 21°45.92'W). The published age model of PS2644-5 is thoroughly constructed by 80 ^{14}C dates and further constrained by the assumption that meltwater events recorded downcore by δ^{18}O coincide with ice berg discharge from ice sheets during GS (Voelker et al., 1998; Voelker et al., 2000; Voelker and Haflidason, 2015). Because the two cores are for the purposes of this study from the same location, we take advantage of the age model from PS2644-5 in establishing the age model for GS15-198-36CC (Sessford et al., 2018). The procedure as described below was done by Sessford et al. (2018) in core GS15-198-36CC.

To establish the correct D-O events and an approximation of ages for GS15-198-36CC, the magnetic susceptibility record (the degree of magnetization of a material in relation to an applied magnetic field), from GS15-198-36CC was tuned to the magnetic susceptibility record from PS2644-5, published by Laj (2003). Core PS2644-5 depth scale was then transferred to that of GS15-198-36CC so that both cores had the same composite depth. Further, the magnetic susceptibility record in GS15-198-36CC was tuned to the NGRIP δ^{18}O record on the GICC05 timescale (Svensson et al., 2008) using tie-points connecting corresponding excursions in the records by the software AnalySeries 2.0 (Paillard et al., 1996) (Figure 6.1). The tie points in the age model in this study differs slightly to that of Sessford et al., 2018 to better constrain the depths between 300-340 cm. In Sessford et al., 2018 this section was floating, but here we constrain it to get a better idea of the transitions between GS9 and HS4.The approach is based on the coherency between magnetic properties in the North Atlantic/Nordic Seas and δ^{18}O records on Greenland (Kissel et al., 1999) and we avoid interpretations based on water mass properties when tuning foraminiferal δ^{18}O to Greenland δ^{18}O.

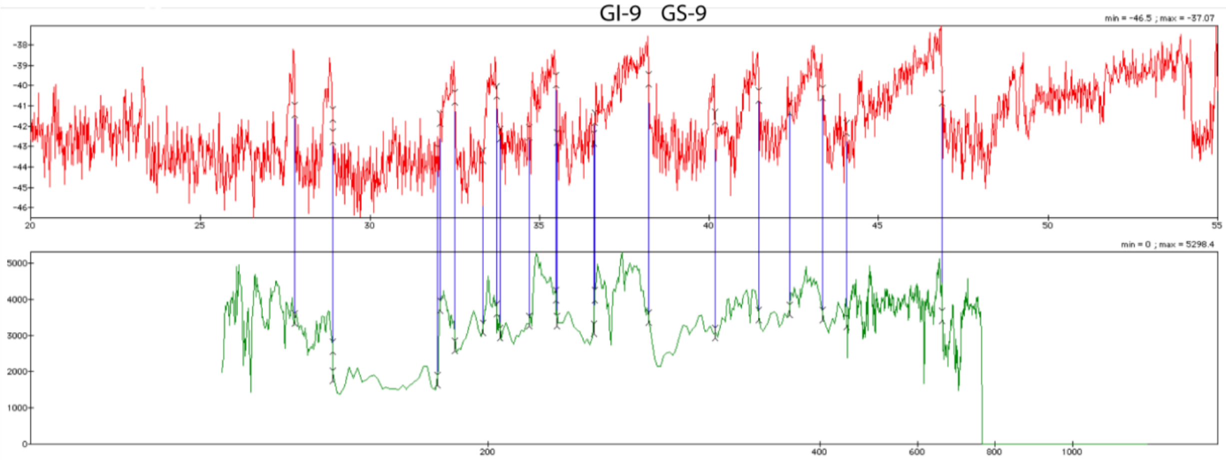

Figure 6.1: The tie-points (blue) between the NGRIP δ^{18}O record on the GICC05 timescale (red) and the magnetic susceptibility record from core GS15-198-36CC (green).

Sedimentation rates were calculated based on the age model (Figure 6.2). The average sedimentation rate over the period 37.11-40.41 kyr is 16.67 cm per kyr. The two tie-points defined within the age-range are connected to the warmings leading into GI8 and GI9. Because sedimentation rates are calculated between the tie-points, sedimentation rates are averaged over GI9 and GS-9 (HS4).

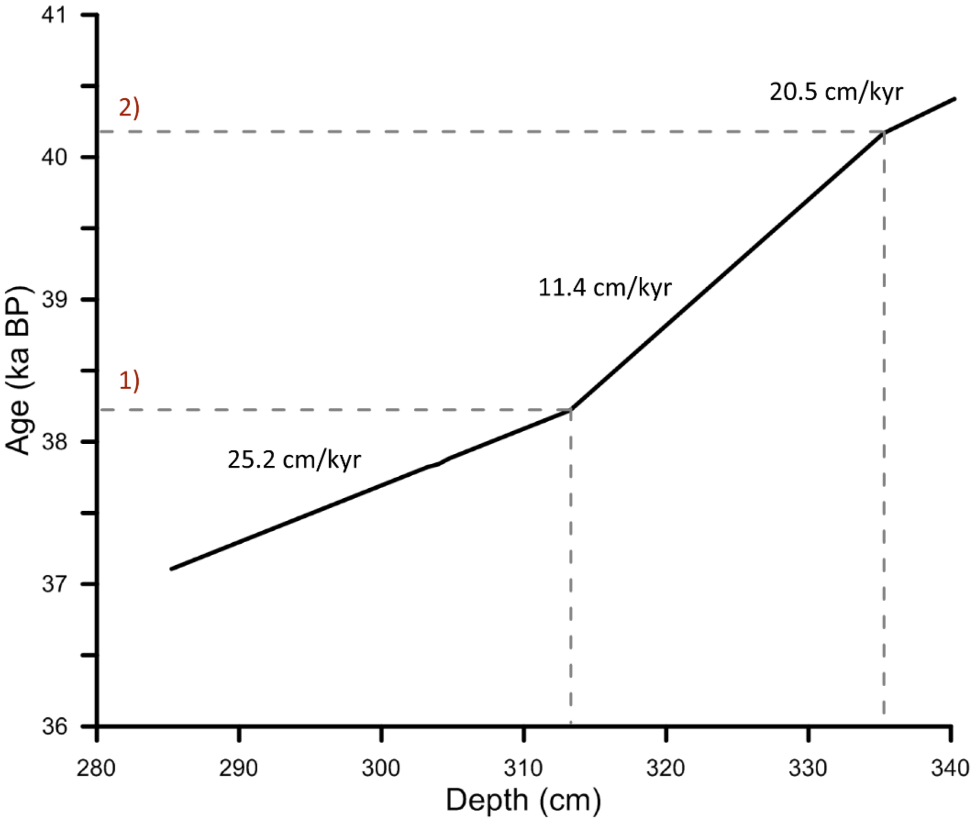

Figure 6.2: Age depth plot for the depth interval 285-340.5 cm in core GS15-198-36CC. Accumulation rates for depth intervals are noted in the black text. Dashed lines indicate transitions from which accumulation rates are calculated. 1) indicates the timing of the warming into the GI8 warm phase and 2) the warming into GI9 warm phase.

7 Discussion

The main purpose of the following sections is to address the objectives presented in section 1.2. The first section below, 7.1, is dedicated to a discussion over the results of the different cleaning protocols and their effects on the measurements. In section 7.2, I deal with the potential environmental clues that are suggested by Mn/Ca variations. The reliability of the Mg/Ca temperature reconstructions is discussed in section 7.3 while the temperature reconstructions together with stable isotope records are interpreted in section 7.4.

7.1 Cleaning Methods

The downcore Mg/Ca records from the “Cd-cleaning” and “full-cleaning” methods are generally in agreement. The main features in terms of depth and amplitude of variations are present in both records. Overall, Mg/Ca is reduced by 7.8% using the “full-cleaning” method, which is less than the average reduction of Al/Ca (26.2%), Fe/Ca (24.2%), and Mn/Ca (12.5%) where concentrations primarily serve as indicators of contaminant phases.

The added DTPA step reduces Al/Ca and Fe/Ca ratios, as evident by reduced noise in the signals downcore (Figure 5.2). High-end Al/Ca at ~800 µmol/mol are almost completely absent in samples subjected to the “full-cleaning”, contrasting the “Cd-cleaning” method. However elevated Al/Ca and Fe/Ca ratios are generally not correlated with high Mg/Ca ratios regardless of the applied cleaning method (Figure 5.4). This low correlation suggests that contaminant phases associated with neither aluminum, Al (aluminosilicates and clays) or iron, Fe (organic material, silicates and iron oxides) are important contaminants after the “Cd-cleaning” protocol prior to the DTPA step. Nevertheless, the DTPA step produces a systematic decrease of Al/Ca ratios and to some extent of Fe/Ca ratios together with a decreased correlation with Mg. This suggests that there is some merit to use the “full-cleaning” method at this site.

Downcore variations of Mn/Ca ratios follow a different pattern than Al/Ca and Fe/Ca by being relatively noiseless, little altered by the added DTPA step, and co-varying with Mg/Ca ratios. The correlation with Mg/Ca is noteworthy, and the “full-cleaning” method leads to a somewhat closer relationship between Mn/Ca and Mg/Ca ratios. The correlation suggests that the mechanisms controlling the concentration of manganese and magnesium into the tests of the foraminifera could be related. The implications of the Mn/Ca record, which is relatively unaffected by the DTPA step, are discussed further in section 7.2.

7.1.1 Effects of DTPA treatment

The DTPA treatment is aimed at removing barite, which can have multiple origins and is a potential source of contaminants. The DTPA treatment resulted in a general reduction in Al/Ca, Fe/Ca, Mn/Ca, and Mg/Ca ratios, with the most pronounced effects on Al/Ca. There are few indicators in the literature that Al substitutes for Ba in barite which makes this result surprising. It is therefore unlikely that the dissolution of barite directly resulted in the reduction of Al/Ca and the other elemental ratios. Ca together with Sr are most likely to substitute for Ba in barite (Griffith and Paytan, 2015) and the effect of direct dissolution of barite would therefore be expected to *increase* the ratios of elements over Ca, in contrast to what is found here. However, barite formed in the water column can also contain traces of organic matter (Paytan et al., 2002) as it forms in microenvironments supersaturated with respects to barite by degradation of organic matter or mediated by pelagic microorganisms (see Griffith and Paytan for an overview). Mg, Fe and other elements associated with organic matter may therefore be contained within pelagic barite. On the other hand, barite may also precipitate within the sediments (diagenetic barite) in supersaturated pore fluids that may be influenced by hydrothermal activity or cold seeps (Paytan et al., 2002).

Barker et al. (2003) postulated that the reductive step might remove contaminant phases other than Mn-Fe-oxides that are trapped by such coatings. It is possible that a similar process occurs when the removal of barite exposes trapped contaminant phases. With that rationale, Mg and Fe in organic matter that was not accessed by the H_2O_2 in the oxidative cleaning step as it was trapped by barite may be exposed and removed with the solution. The DTPA step is aggressive also with respect to dissolution of calcite (Lea and Boyle, 1993), an apparent effect when visually comparing sample size before and after treatment. Thus, it is possible that post-depositional calcite that is trapping contaminant phases is also removed. The reduction of Al/Ca after the “full-cleaning” method to a baseline level of ~400 µmol/mol may be associated with the dissolution diagenetic barite and post-depositional calcite that exposes aluminosilicates, such as Al-rich clay-minerals like illite, that are subsequently removed by the solution.

7.1.2 Non-uniform Mg reduction after the “full-cleaning” method

The reduction of Mg/Ca due to the “full-cleaning” method is non-uniform over the record: deeper than ~307 cm the “full-cleaning” method results in consistently lower Mg/Ca compared to the “Cd-cleaning” method (~10.5% reduction), whereas the difference is smaller above ~307 cm (~3.8%) (Figure 7.1). Curiously, the change occurs close to the depth where the color of the sediments change from “olive-dark-gray silty clay“ to “dark-gray-brown silty clay” (Figure 5.1) and close to the change in sedimentation rate from 11.4 to 25.2 cm/1000 years (Figure 6.1) which corresponds to the timing of the warming into GI8.

The timing of the divergence of Mg/Ca ratios after DTPA treatment suggests that the difference in removal of Mg-containing phases is related to the change in sedimentation rate or sedimentary geochemistry under the transition into GI8. It is tempting to speculate on the variability in the barite abundance, but Ba/Ca records are most likely unreliable due to noisiness in the record and since the measured values are close to the instrumental detection limit of the ICP-OES. One may infer, however, that the sedimentation of pelagic barite was lower during GS9 due to decreased primary productivity, which has been shown to decrease during Greenland stadials (Nave et al., 2007). Assuming that pelagic barite is the primary source of barite to the sediments (Horner et al., 2017) there should then be a higher potential for barite associated contamination phases during the GI. I thus suggest that there is less barite to be removed in records from the Stadial phase and that the DTPA solution therefore continues to attack calcite. Since Mg is more susceptible to dissolution (Brown and Elderfield, 1996), these measurements are left with lower Mg/Ca ratios.

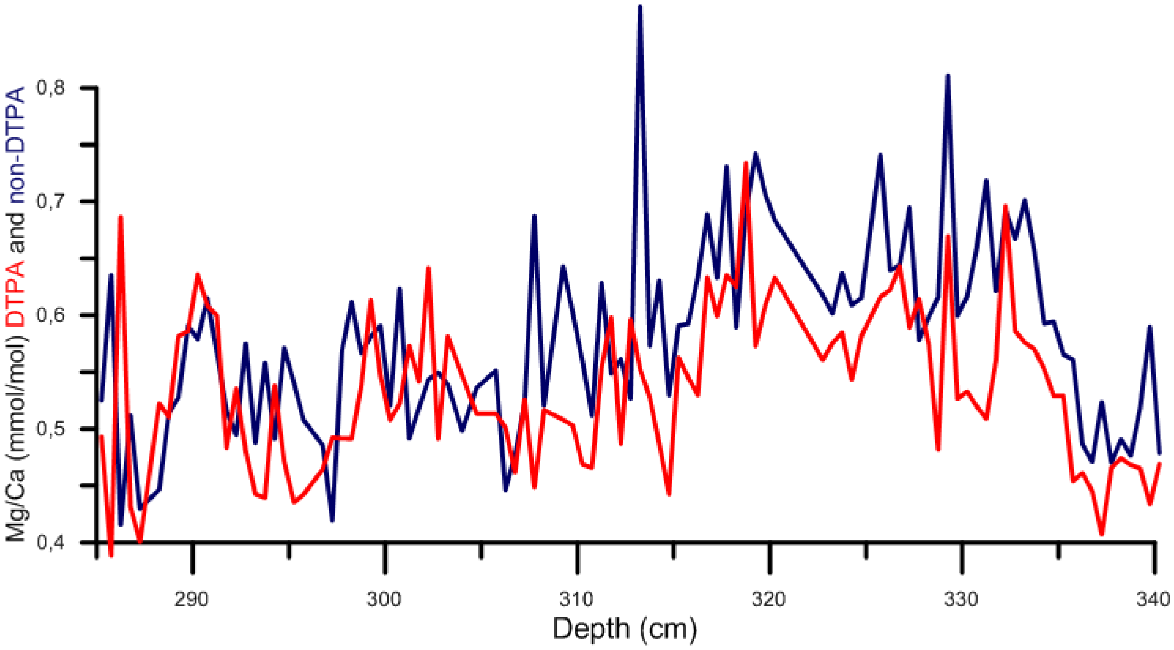

Figure 7.1: Comparison of Mg/Ca after the "Cd-cleaning" (blue) and the "full-cleaning" (red) methods showing how the records diverge, depending on cleaning method, at ~310cm.

Overall, the "Cd-method" and "full-cleaning" methods yield very similar results in terms of Mg/Ca. The "full-cleaning" method is more efficient at removing aluminum and iron to some extent, but due to the low correlation between Al/Ca, Fe/Ca and Mg/Ca, contaminant phases associated with aluminum and iron are not a major issue in this record regardless of the added DTPA step. Mn/Ca is largely unchanged by the “full-cleaning” method showing that the DTPA-step is largely inefficient at removing Mn-related contaminant phases. Still, because it is associated with lower ratios of contaminant indicators, the Mg/Ca record after the “full-cleaning” method will be used in the following discussion.

7.2 Environmental clues from Mn/Ca

The correlation between Mn/Ca and Mg/Ca deserves attention. Manganese is a common suspect of contamination in complex Mn-Fe-oxides and manganese rich carbonates that precipitate as overgrowths within the sediments (Boyle, 1981; Boyle, 1983; Pena et al., 2005; Pena et al., 2008). Magnesium is present in Mn-nodules in concentrations at about 100 mmol/mol (Barker et al., 2003), which is orders of magnitudes higher than what is seen in primary foraminiferal calcite and in this record. Thus, the presence of even smaller quantities of Mn-oxides as overgrowths on foraminiferal calcite may contaminate the signal from primary calcification at subsurface. Boyle (1983) report that foraminifera samples with Mn/Ca < 105 µmol/mol indicate minimal effects of diagenetic coatings on the results. Mn/Ca values in this record are around or above this threshold below 320 cm, with clear spikes between 329-335 cm depth coinciding with the initial warming recorded by Mg/Ca (Figure 5.2 and 5.6).

The Mn/Ca record in this study resembles a “smoothed” version of the Mg/Ca record (Figure 7.2 and 7.3). The Mn/Ca record also co-varies with δ^{13}C where low Mn/Ca coincide with high δ^{13}C (Figure 7.2 and 7.3), particularly during GI8 and the transition into the interstadial where the coefficient of determination is 0.3; comparable to the correlation to the Mg/Ca record (Figure 7.2). This correlation raises questions whether there is a common origin to the signals, or if there is a causal link where environmental controls on one lead to changes that are expressed in the others.

The distribution and speciation of manganese in the sediments is controlled by the redox-state, where Mn (II) is soluble in oxygen depleted settings and the higher oxidation states Mn (III) and Mn (IV) occur as relatively insoluble oxides and hydroxides in well oxygenated environments (Calvert and Pedersen, 1996). Under reducing conditions, Mn accumulation is low and controlled by the detritic fraction, and there is no accumulation of Mn-oxides (Calvert and Pedersen, 1996). Thus, the sedimentary distribution of manganese, due to its redox-sensitivity, is controlled by several factors related to oxygen contents on and within the sediments, including the degree of ventilation of bottom waters, bulk sedimentation rate, and rate of organic matter transport to the sea floor (Jaccard et al., 2016). The sedimentary distribution and speciation of manganese is accordingly related to environmental factors that are connected to the availability of oxygen. The reductive step in the cleaning protocol has likely removed Mn-oxides, but the removal efficiency is not possible to determine in this study.

Assuming complete Mn-oxide removal by the reductive step, the downcore variations in Mn/Ca reflect manganese incorporated into calcite, either during primary test formation or in post-depositional overgrowths. In the latter case, the elevated Mn/Ca during the warm phases would be related to more reducing sediment conditions allowing soluble Mn (II) to precipitate in secondary calcite as overgrowths. Such carbonate overgrowths may be assumed to be enriched in Mg/Ca also, due to the preferential dissolution of Mg (Brown and Elderfield, 1996) leaving pore-fluids enriched in Mg.

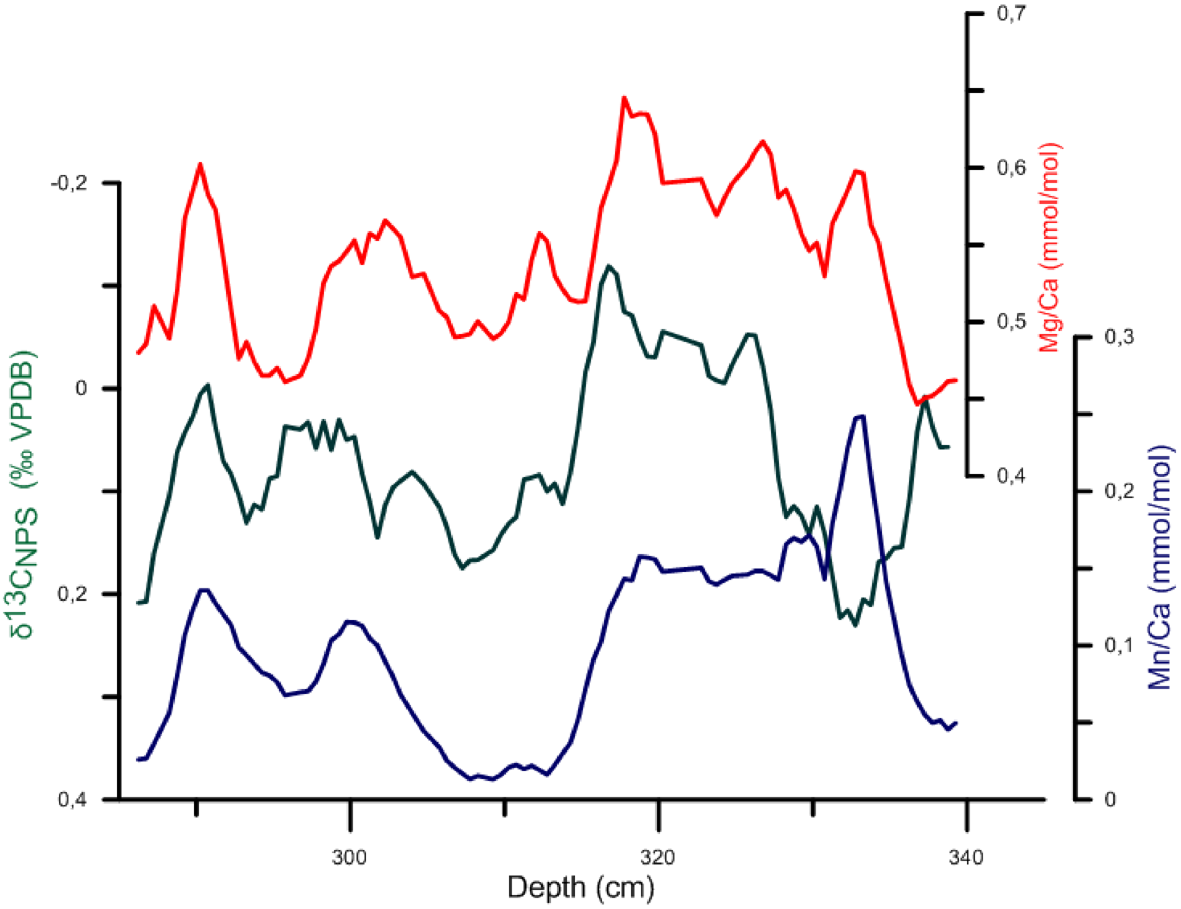

Figure 7.2: 3-point running average of Mg/Ca after the “full-cleaning” method (red), δ^{13}C (green) and Mn/Ca after the “full-cleaning” method (blue) at depth (cm). The scale of δ^{13}C is inversed compared to the normal presentation to highlight the correlation.

Alternatively, the Mg/Ca record purely reflects temperatures in the near-surface during primary calcification. High Mg/Ca ratios (i.e. warmer temperatures) correspond with lower δ^{13}C, which is here interpreted as a signal of poorer ventilation of near-surface waters caused by a strong halocline that isolates the near-surface from the atmosphere (see argument in section 7.4.1). With fresher waters in the surface forming a strong halocline there is limited formation of deep-waters. As a result, bottom waters are not replenished by cold and well oxygenated surface waters. This would mean that Mn is not oxidized in the surface sediments and that reduced species dominate, precipitating as Mn-rich carbonate overgrowths. In good agreement with $\delta^{13}C$ records in this study, poor ventilation of intermediate waters in the south-east Nordic Seas during Heinrich events have also been inferred by carbon isotopes (Rasmussen and Thomsen, 2009; Dokken et al., 2013). North Atlantic bottom water oxygen concentrations have been found to vary over D-O cycles with minima during Heinrich events (Hoogakker et al., 2015) fitting with reduced deep-water formation in the Nordic Seas and a weakened AMOC.

However, much remains unclear regarding this argument. Temperature at the air-sea interface influences $\delta^{13}C$ (DIC) in seawater (Mook et al., 1974) which may cause the inverse correlation between Mg/Ca and $\delta^{13}C$, but this effect may fit well with the reasoning above (as further discussed in section 7.4.1). Furthermore, lower primary production during Heinrich events (Nave et al., 2007) presumably led to lower transport of organic matter to the sediments. With less accumulating organic matter there would be less respiration at/within the sediments leaving oxygen available for Mn-oxidation. If the influence of organic matter transport exceeded the influence of dissolved oxygen concentrations in the bottom waters, it is likely that high (>100 µmol/mol) Mn/Ca during the stadial is associated with Mn-oxides. That would imply that the Mn-oxides were not sufficiently removed by the reductive cleaning. Furthermore, the relationship breaks down deeper than ~325 cm (Phase 1) where $\delta^{13}C$ becomes higher together with Mn/Ca and Mg/Ca. A comparison with samples cleaned without the reductive step could yield clues about the manganese speciation and could further permit attempts at correcting for Mn-rich contaminant phases on Mg/Ca temperatures (Hasenfratz et al., 2017). Yet, it seems likely that Mn/Ca after reductive cleaning yields environmental clues, and is not simply an indicator of contamination of Mg/Ca.

7.3 The reliability of the temperature reconstructions

To reconstruct reliable temperatures in cold polar waters is a difficult task. Within the Polar domain, quantitative temperature reconstructions based on planktonic foraminiferal assemblages are not useful because *N. pachyderma* comprise nearly all of the planktonic foraminiferal faunal assemblages (Pflaumann et al., 2003; Meland et al., 2005). Such problems extend outside of the polar domain in areas with summer surface temperatures below 4-5°C (Pflaumann et al., 2003) and motivates the use of Mg/Ca in order to estimate past temperatures in the study area. However, Mg/Ca ratios are often too high to reflect modern calcification temperatures north of Iceland for unknown reasons (Meland et al., 2005). Mg/Ca temperature reconstructions are also complicated to use in the Nordic Seas because the Mg/Ca ratios vary less with temperature when temperature are low than when temperatures are high (e.g. Elderfield and Ganssen, 2000). This caveat is important in the western part of the basin since it is dominated by Polar surface water. Furthermore, salinity variations related to melting of glacial ice and formation/melting of sea ice may impact Mg/Ca temperature reconstructions as salinity has been shown to influence Mg substitution (Nürnberg et al., 1996; Lea et al., 1999; Kisakürek, 2008). However, the fact *N. pachyderma* escapes low salinity environments by diving beyond fresh surface waters (Carstens et al., 1997), likely decreases the importance of surface salinity changes at high latitudes. Moreover, high influx of glacial marine sediments increases the potential of sample-contamination, further increasing uncertainties.

Since this is the first planktonic Mg/Ca temperature reconstruction from the Denmark Strait over a D-O cycle during the MIS3, the reliability of the reconstructions is assessed through core-top inferences, oxygen isotope comparisons and comparisons with nearby records. The data presented here suggests that temperature reconstructions in the Denmark Strait during the last glacial period is possible, despite that several of the factors known to influence foraminiferal Mg/Ca are not accounted for in detail.

7.3.1 Core-top inferences

Reconstructed temperatures from core-top samples at the site are in good agreement with local temperature profiles (Figure 5.5). Core-top reconstructed temperatures of 0-0.5 cm depth and 0.5-1 cm depth fall between ~5.5±0.6°C and ~7.8±0.6°C corresponding to modern surface water temperatures above ~100 m water depth during the summer season (uncertainty from Elderfield and Ganssen, 2000). These warm temperatures, both from the conductivity- temperature-depth (CTD) sensors and core-top reconstruction, suggests influence of Atlantic water at the site. However, the CTD only records a single day and it may be unlikely that the NIIC regularly penetrates so far northwest (Macrander et al., 2014). Therefore, it is possible that the temperature measured by the CTD is higher than the average summer temperature at the site. However, based on the extrapolated summer season average temperatures in Figure 3.1, the CTD temperatures are not unreasonable. Moreover, the high end core-top reconstructed temperature of 7.8°C is about 1°C higher than surface temperatures indicated by the CTD and adding the uncertainty of the calibration puts the reconstructed temperatures very close to the CTD-temperatures.

7.3.2 Correlation with oxygen isotope data

A comparison of oxygen isotope data with the Mg/Ca temperature reconstruction may provide insight into the validity of the temperature reconstruction because the records are derived from the same sample material and thus reflect the same environmental conditions. Stable isotopes have a long history of application in the Nordic Seas and North Atlantic (Meland et al., 2005). The major features of the Mg/Ca record also appear in the oxygen isotope records (Figure 5.6 and 7.3), and the similarity is most apparent during HS4 and the transition to GI8. At the transition into GI8, Mg/Ca reconstructed temperatures decrease together with an enrichment in ^{18}O and ^{13}C. This similarity lends credence to the Mg/Ca thermometer. However, since $\delta^{18}O$ is related to salinity and some studies indicate that also the Mg/Ca ratio has a salinity component (Nürnberg et al., 1996; Lea et al., 1999; Kisakürek, 2008), the coeval response at the transition into GI8 does not definitively verify that Mg/Ca records only temperature. Yet, it is unlikely that salinity controls the Mg/Ca ratio due to *N. pachyderma's* low tolerance for fresh waters (Carstens et al., 1997). The change in $\delta^{18}O$ from ~3‰ to 4.10‰ over the transition to GI9 in Figure 7.3 (Phase 3 in Figure 5.6) translates to a temperature decrease of ~4.8°C according to the 0.23‰ per °C relationship (Shackleton, 1974) which corresponds well to the Mg/Ca reconstructed temperature decrease including uncertainty of ~4.5°C (Figure 5.6.a). Excluding the calculated uncertainty from the Mg/Ca temperature estimates, the $\delta^{18}O$ temperature change over the transition is somewhat larger than the Mg/Ca temperature reconstruction. This difference is reflected also in the $\delta^{18}O_{sw}$ (Figure 7.3.e) which thereby includes an increase of $\delta^{18}O_{sw}$ in the transition from HS4 to GI8.

The transition from warm to colder temperatures in the Mg/Ca reconstructions broadly coincide with higher $\delta^{18}O$ and the transition into the interstadial in isotope data on Greenland (Figure 7.3). This suggests that the Mg/Ca change reflect near-surface cooling when abrupt warming is reflected in Greenland ice cores. While the warming on Greenland occurred over decades, changes in the marine record presented here takes place over centuries. The timing is overlapping, however, highlighting the relationship between the settings on Greenland and the marine settings. That Mg/Ca records agree with $\delta^{18}O_{calcite}$ and are in opposite phase with Greenland temperature, is particularly evident over the transition into the warm interglacial. This implies that Mg/Ca ratios are likely to record temperature change associated with the transition.

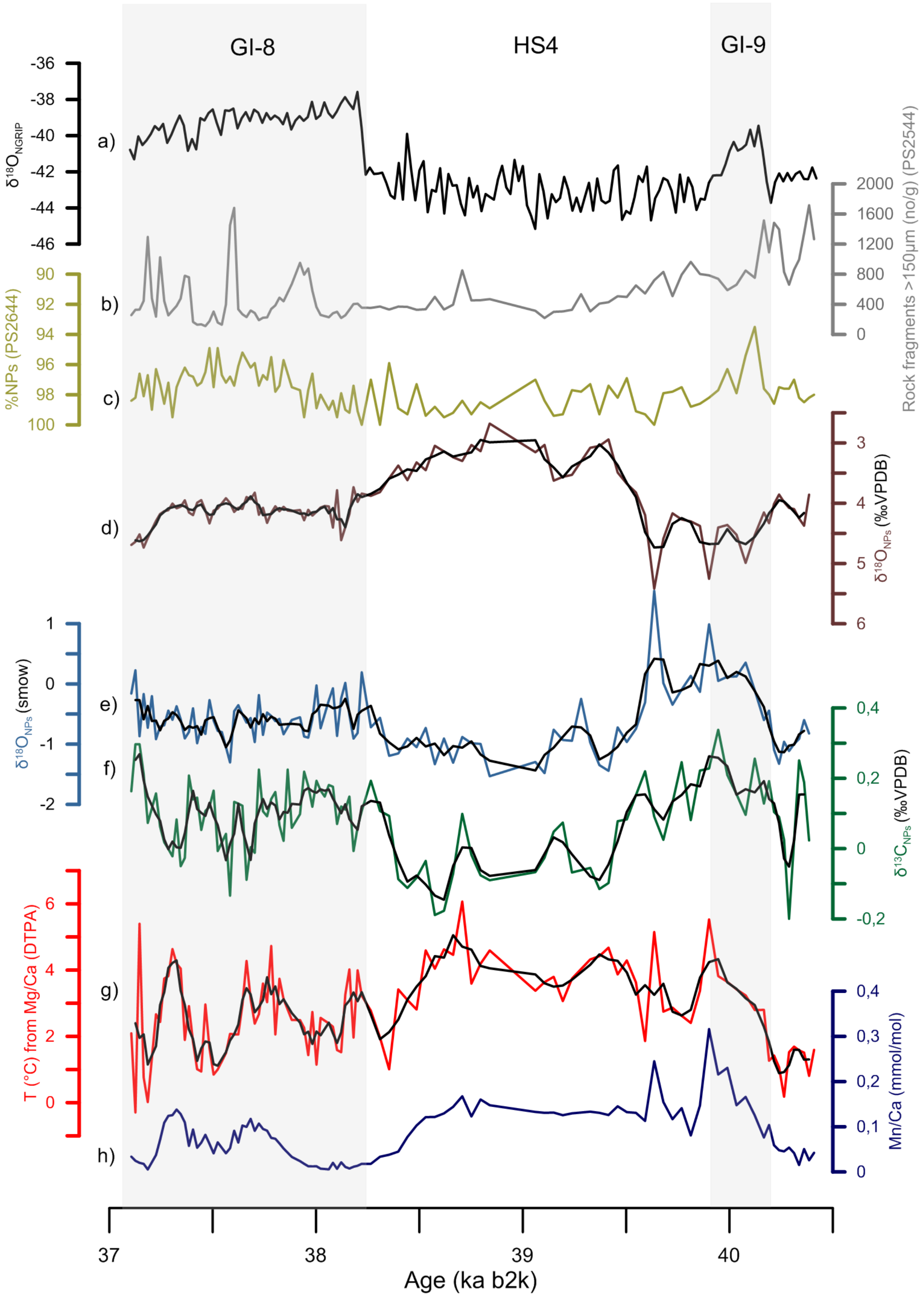

Figure 7.3: Downcore data sets from NGRIP, core PS2644 and core GS15-198-36CC covering the period 37.1 to 40.4 kyr plotted on the GICC05 (b2k) time scale. (a) NGRIP $\delta^{18}O$ (proxy for temperature on Greenland with lower $\delta^{18}O$ indicating warmer conditions), (b) lithic fragments >150 µm (IRD) counted in number per gram from core PS2644 plotted on the constructed age model, (c) percentage of *N. pachyderma* in the size fraction 150-500 µm from core PS2644 plotted on the constructed age model, (d) GS15-198-36CC near-surface $\delta^{18}O$ from *N. pachyderma*, (e) GS15-198-36CC near-surface $\delta^{18}O_{sw}$ (smow) from *N. pachyderma*, (f) GS15-198-36CC near-surface $\delta^{13}C$ from *N. pachyderma*, (h) Mn/Ca from *N. pachyderma*. Grey shaded periods indicate interstadial periods. Black lines in d-g) show 5 point running averages.

7.3.3 Similarity with other Nordic Sea cores

Similarities between records in this study and records from the Southeast Norwegian Seas support the validity of the records in this study and the achievability of Mg/Ca based temperature reconstruction in the Denmark Strait. The North Atlantic Current enters the Nordic Seas primarily in the Norwegian Sea (Østerhus et al., 2005), transporting heat and making the upper water column warmer and saltier than in the Iceland and Greenland Seas. This difference is highlighted by the Polar and Arctic fronts that have a meridional orientation (Figure 3.1). Temperature reconstructions from the northeastern flank of the Faeroe-Shetland Channel in core MD99-2284 (yellow dot in Figure 7.4) based on foraminiferal assemblages largely resemble the records in core GS15-198-36CC in terms of a stadial subsurface warm phase and colder temperatures during the interstadial (Dokken et al., 2013). The amplitude of temperature change is also similar, besides from a temperature "overshoot" at transitions to interstadials in core MD99-2284. Furthermore, *N. pachyderma* records from core ENAM93-21 (red dot in Figure 7.4) is in good agreement with the oxygen isotope records here with peak stadial $\delta^{18}O$ of ~3‰ and $\delta^{18}O$ of ~4‰ during GI8 (Rasmussen and Thomsen, 2004). The resemblances in the records overall across the basin lends credence to the robustness of the temperature reconstructions here.

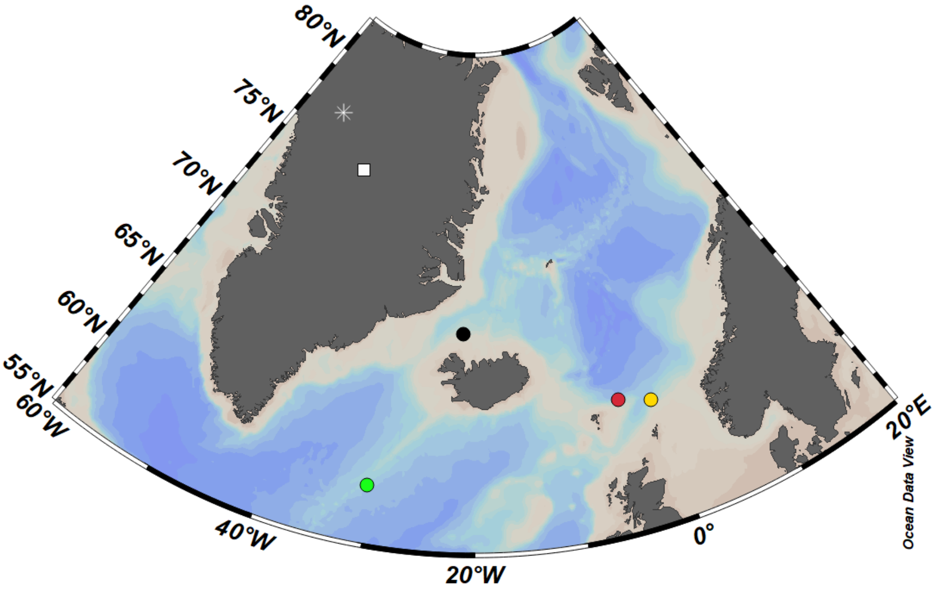

Figure 7.4: Overview of the locations of cores referred to in the text. The black dot indicates the core-site for core GS15-198-36CC and is adjacent to the location of core PS2644, red dot for core ENAM93-21 (Rasmussen and Thomsen, 2004; Rasmussen et al., 1996), yellow dot for core MD99-2284 (Dokken et al., 2013), and green dot for cores LO09-18 / DS97-2P (Jonkers et al., 2010a). White square indicates the NGRIP ice core site, and the white star the location of NEEM (Guillevic et al., 2014).

7.4 Temperature evolution during the recorded interval

As described earlier, D-O events are characterized on Greenland by an abrupt warming from cold stadial conditions to a warmer interstadial phase followed by gradual cooling before temperatures drop back to stadial conditions (Figure 7.3.a). Although defined on Greenland, the climatic imprint of D-O events are far-felt (Voelker, 2002). Stadial and interstadial phases are also linked with different water mass characteristics in the North Atlantic and Nordic Seas (Curry and Oppo, 1997; Dokken and Jansen, 1999). The pattern of stadial and interstadial phases are attributed to variations in the AMOC (Broecker et al., 1985) likely due to freshwater perturbations in the North Atlantic region. The abruptness of the warming into interstadial phases has more recently been attributed to a rapid demise of sea ice extent (Gildor and Tziperman, 2003; Li et al., 2010; Dokken et al., 2013; Rasmussen and Thomsen, 2004). Here follows an interpretation of the geochemical proxies and their inferences about the temperature evolution and water mass characteristics in the Denmark Strait.

7.4.1 HS4

During the stadial phase when Greenland is cold (GS), *N. pachyderma* calcify in relatively warm waters in the Denmark Strait as indicated by the Mg/Ca temperature reconstruction (Figure 7.3). This seemingly counterintuitive feature of the stadial may be contextualized by corroboratory data here and by revisiting the life cycle of polar planktonic foraminifera. *N. pachyderma* is known to migrate vertically in the water column to avoid unsuitable habitats, particularly related to low-salinity surface waters (Carstens et al., 1997). A well-developed halocline may therefore force *N. pachyderma* to migrate downwards in the water column into warmer subsurface waters that are isolated from the atmosphere due to stratification and sea ice cover, which disable the loss of heat from relatively warm waters to the cold atmosphere. Model simulations have indicated that such a subsurface warming in the North Atlantic Ocean and the Nordic Seas is possible despite a reduced, or even shut-off AMOC (Shaffer et al., 2004; Marcott et al., 2011; Jensen et al., 2018). Without deep water formation, intermediate waters at low latitudes warm by downward diffusion of heat or mixing to water depths of 2500 m (Schaffer et al., 2004) and some of the accumulated heat is subsequently transported northwards. A strong halocline in the Nordic Seas, with a meltwater cap in the surface likely accompanied by expansive sea ice, was probably a pervasive facet of the stadial phase (Dokken et al., 2013; Li et al., 2005; Hoff et al., 2016; Sadatzki et al. in press). This scenario is further supported by the $\delta^{13}C$ and $\delta^{18}O$ records here as described below.

Carbon isotopes are retrieved from the same sample as Mg/Ca and yield additional clues to the mechanisms controlling the distribution of warm subsurface waters. The $\delta^{13}C$ signal in planktonic foraminiferal calcite is related to ventilation and age of the ambient water masses. CO_2 is exchanged between the atmosphere and the ocean at the surface and through photosynthesis and ^{12}C is preferentially utilized causing ambient water to be enriched with respect to $\delta^{13}C$ when organic matter sinks and is removed from local carbon cycling. When a strong halocline is present, *N. pachyderma* migrates downwards in the water column out of the low-salinity mixed layer and into warmer subsurface waters. Due to gradual decomposition of low $\delta^{13}C$ organic matter and mixing with deeper water masses, $\delta^{13}C$ is gradually lowered with age when disconnected from the atmosphere, as observed during HS4 that is associated with the lowest $\delta^{13}C$. This $\delta^{13}C$ pattern is likely enhanced by the influence of temperature at the air-sea interphase where warmer waters have lower $\delta^{13}C$ at equilibrium (Mook et al., 1974). Following the reasoning above, warmer waters at the site would be a result of displacement at the margin where warmer waters submerge below a less dense halocline. Without approaching equilibrium with a progressively colder atmosphere towards the site, the lower $\delta^{13}C$ signal from a warmer site may become preserved. Seawater on a northward path is likely to become progressively older if mixed with other water masses including decomposed low $\delta^{13}C$ organic matter before reaching the study site. As observed in the record (Figure 7.3), HS4 is associated with increasing temperatures and progressively lower $\delta^{13}C$.

The interval of depleted $\delta^{13}C$ during HS4 should be considered in the context of global carbon cycle inventories. Heinrich Stadials are associated with increasing atmospheric CO_2 concentrations with an amplitude of ~20 ppm for H4 (Ahn and Brook, 2014). The mechanisms for CO_2 increase during Heinrich Stadials are not completely understood, but they are thought to include decreasing terrestrial carbon storage, reduced CO_2 solubility due to a warmer Southern Ocean, and increased ventilation of respired carbon in the Southern Ocean (Schmittner et al., 2007). A release of respired carbon, in the Southern Ocean and from the terrestrial biosphere, would lower the total atmospheric $\delta^{13}C$. Because the North Atlantic Ocean is relatively well equilibrated with the atmosphere (Galbraith et al., 2015), I speculate that an effect would be a lowering of $\delta^{13}C$ (DIC) at the core site. This may account for a small part of the depletion observed in the HS4 in this record. Indeed, the atmospheric CO_2 concentration recorded at Antarctica rises (Figure 2.2) as the $\delta^{13}C$ lowers in this record over HS4 (Figure 7.3). It is difficult to accurately correct for this effect, but since $\delta^{13}C$ co-varies with reconstructed temperatures also within shorter events during GI8 in this record, I argue that the $\delta^{13}C$ signal is mainly reflecting ventilation changes. Furthermore, LGM to modern $\delta^{13}C$ marine change has been estimated to be ~0.3‰ ± 0.2 ‰ (Gebbie et al., 2015) which is comparable to the amplitude of change recorded here over stadial/interstadial.

N. pachyderma is generally associated with Polar Water or Arctic Water (Johannessen et al., 1994), and one might therefore expect that the increased penetration of Altantic Water during HS4 (as implied by the higher water temperatures) would decrease the dominance of *N. pachyderma*. However, *N. pachyderma* constitute >95% of the planktonic species assemblage over the complete record here (Voelker and Haflidason 2015). It is possible that the full assemblage has not been resolved since foraminiferal assemblage counts were only done in the 150-500 μm size fraction, potentially missing Atlantic Species in the smaller size fraction (Hasum and Hald, 2012). Bé and Tolderund (1971) report that where summer temperatures are below 5°C, there is almost a total dominance of *N. pachyderma*. Since the entire temperature range in this record is below 5°C, this temperature cut-off may explain why the *N. pachyderma* count does not respond to the warming. This also underlines that Mg/Ca ratios may be used to reconstruct temperatures in this temperature range.

Lower $\delta^{18}O$ during HS4 in this record indicates that a combination of warmer water, meltwater and brines influenced the depth habitat of *N. pachyderma*. Whereas temperature constitute a part of the $\delta^{18}O$ signal, HS4 is also marked by lower $\delta^{18}O_{sw}$ (Figure 7.3). Some mixing probably occurred between the fresher surface waters with low $\delta^{18}O_{sw}$ and the warmer and more saline waters at the depth habitat of *N. pachyderma* contributing to the lower $\delta^{18}O_{sw}$. Large scale downward mixing of fresher surface waters is unlikely, however, as it is unfavorable for *N. pachyderma*. On the other hand, waters containing brines from the formation of sea ice mixed into the depth habitat of *N. pachyderma* would also potentially lower $\delta^{18}O_{sw}$ (Dokken and Jansen, 1999). Beyond explaining a part of the $\delta^{18}O_{sw}$ signal, brine rejection associated with sea ice formation close to shelves acts as a mechanism to maintain a strong halocline (Aagaard et al, 1981; Dokken et al., 2013; Lind et al., 2018). This mechanism is enhanced when there is summer melt of sea ice which leaves the surface waters freshened, promoting sea ice growth the following winter. Both downward mixing of fresher surface waters and sinking of brines probably worked in conjunction to lower the oxygen isotope signal of near-surface waters in the Denmark Strait during HS4.

These two mechanisms for lowering $\delta^{18}O_{sw}$ come with different implications for the salinity of the subsurface, which together with a detached modern $\delta^{18}O_{sw}$ /salinity relationship (Figure 5.5) make quantifications of salinity difficult. Furthermore, meltwater from ice sheets during the last glacial would have a lower $\delta^{18}O_{sw}$ signal than modern meltwaters as conditions where colder. The lowering of the freshwater endmember in $\delta^{18}O_{sw}$ would cause an overestimation of the fresh water influence if not accounted for.

The most abrupt oxygen isotope change in this record occurs during the GS9, with a lowering of $\delta^{18}O$ into the stage described in the paragraphs above, between 39.6 kyr and 39.4 kyr without any synchronous change in Greenland temperatures (Figure 7.3). The timing of this change is coherent with North Atlantic ice berg discharge in Heinrich Event 4 that occur centuries after the onset of the stadial

(Bond et al., 1993; Guillevic et al., 2014), although age-model uncertainties should be considered. This stage (Phase 1C in Figure 5.6) is associated also with abrupt lowering of δ^{13}C implying poorer ventilation, or a larger geographical extent of the fresh water lid. The strong halocline as described in the paragraphs above could therefore be related to the ice-berg discharge. Before this change in the early GS9, the oxygen and carbon isotope records indicate that rather ventilated and saline waters were present over the core site. Moreover, Mg/Ca reconstructed temperatures are relatively high also in the stadial interval before the change in oxygen and carbon isotopes, even though these temperature estimates should be treated with caution due to high Mn/Ca values (Figure 7.3.g-h).

7.4.2 Interstadial situation

When Greenland is warm during GI8, planktonic foraminiferal calcite records overall colder temperatures, heavier δ^{13}C and δ^{18}O (Phase 4 in Figure 5.6) than during the stadial phase (Figure 7.3). Heavier δ^{13}C indicates that there is enhanced ventilation of the near-surface waters. Together, the data supports a weaker halocline and weaker stratification allowing for noticeable influence of Atlantic waters near the surface. Without the presence of the low-density fresh waters stratifying the water column, warmer Atlantic Waters are not isolated from the atmosphere leading to gradual heat loss on its northward course, and to colder temperatures.

The data indicate an unstable near-surface environment during GI8. On the colder and well-ventilated baseline through the interstadial, there are temperature variations with a maximum amplitude similar to the GS9 to GI8 transition (Figure 7.3.g). These warm episodes occur with excursions of light carbon isotopes which are especially apparent in the younger part of the record (Figure 7.3.f). The relationship between temperature and carbon isotopes within GI8 thus aligns with the general stadial/interstadial pattern observed here where warmer waters correspond to lighter δ^{13}C and colder waters to heavier δ^{13}C. Due to the higher sedimentation rate during the GI8, these variations are consistent features over multiple samples. Presumably, periods of re-stratification and concomitant subduction of Atlantic Waters occurred during the periods of GI8 that are characterized by warmer water and lower δ^{13}C. On that note, the lower amplitude in negative δ^{13}C excursions within the interstadial compared to the stadial/interstadial pattern is consistent with younger waters which would be expected as these excursions are shorter. The general picture during GI8 is that a halocline with low salinity surface waters retreats or weakens compared to the preceding stadial. Periodically, it extends or strengthens to an intermediate phase isolating warmer subsurface waters from the atmosphere. As these fluctuations are not apparent in the Greenland isotope record (Figure 7.3.a) they were probably of local extent and without major effects on the sea ice distribution which has been shown to pose important controls on Greenland temperatures (Li et al., 2005; Sadatzki et al. in press).

δ^{18}O remains stable and relatively heavy through GI8 (Figure 7.3d) suggesting that saline Atlantic Water influences the study site, in agreement with the reasoning above. Such waters with higher salinity might cancel the effect of higher temperatures on δ^{18}O, thus creating a flatter record than Mg/Ca which is interpreted as a pure temperature signal. Rasmussen and Thomsen (2004) argue for an interstadial circulation system similar to the modern mode where Atlantic Waters enter the Nordic Seas in the surface that subsequently cool and cause open convection. Whether the Atlantic Water influx is due to an active NIIC (Figure 3.1) is unresolvable from this record alone and its importance over stadial/interstadials remains unexplored. An active NIIC introduces warm and saline surface waters to the study site in the modern setting (Våge et al., 2013) (Figure 3.1). On the other hand, because the NIIC introduces a small flux compared to the eastern inflows of Atlantic Waters to the Nordic Seas (Østerhus et al., 2005), the regional imprint of an active NIIC may be relatively muted. Future ocean model experiments may shed light on the importance of the NIIC over D-O cycles.

Higher input of IRD (Figure 7.3) during the interstadial suggests higher melt of icebergs in the region thus also potentially impacting the salinity of the near-surface waters and the stratification of the surface layers (Figure 7.3.b). In the modern setting, relatively low salinity surface water from the Arctic together with melt-water and sea ice is transported in the EGC. This produces a stratification in the western Denmark Strait where cold and fresh waters cap underlying saltier and warmer waters (Figure 3.2). The EGC and the separated branch (Figure 3.1) are variable in terms of position, strength and lateral extent (Våge et al., 2013; Köhl et al., 2007). I propose that a variable extent of cold and fresh surface waters in the EGC occasionally produced a strong local halocline in a narrower Denmark Strait that isolated warmer subsurface waters from the atmosphere thereby producing the interglacial variations in temperature and ventilation discussed above.

7.4.3 Transition into GI8

All proxies record a shift from stadial to interstadial conditions (Figure 7.3). The onset of the transition at about 38.6 ka b2k (kiloanni before A.D. 2000) is characterized by maximum temperatures and minimum δ^{18}O and δ^{13}C. Subsequently, subsurface temperatures drop and stable isotopes are enriched. Whereas the transition into GI8 occurs over decades on Greenland, the signal in the subsurface waters in the Denmark Strait changes over ~700 years with the onset centuries before abrupt warming on Greenland. Uncertainties in the age model needs to be considered here, potentially narrowing this gap, yet it is likely that the changes in the Denmark Strait were more gradual than on Greenland. The abruptness of warmings leading into GIs require changes in components and feedbacks of the climate system capable of rapid response time. Warming subsurface and intermediate waters in the Nordic Seas and the subsequent reorganization of the thermocline has been hypothesized to be causal agent of D-O warmings by the mechanism of abrupt release of stored oceanic heat to the atmosphere (Rasmussen and Thomsen, 2004) which forces stadial sea ice to diminish leading to reorganizations in atmospheric circulation (Dokken et al., 2013). This leads to more active deep water formation in the Nordic Seas through the GI. The more gradual near-surface changes in the Denmark Strait indicates that the oceanic heat release and sea ice diminution that led to the abruptness of change in the Greenland ice core record (Li et al., 2010) happened east of the site, as proposed by Dokken et al. (2013).

The data here indicate a reorganization of the thermocline over the transition, at large in agreement with the Rasmussen and Thomsen (2004) and Dokken et al. (2013). Two main features differentiate records from the Faeroe Shetland Channel (Dokken et al., 2013) and the records from the Denmark Strait: (1) a dramatic temperature “overshoot” occurring at the warm phase transition in the Faeroe Shetland Channel, and (2) the shorter time scale of the transition in the Faeroe Shetland Channel. The “overshoot” provides an argument for abrupt disruption of the thermocline by shoaling of warm subsurface water and the. Furthermore, the full amplitude change occurs over only ~200 years. The longer transitional phase and absence of a sudden overshoot in the data of this study suggest qualitative differences in the oceanographic conditions in the eastern and western entrance to the Nordic Seas during the transitional phase. It is here possible, however, that the time-scale of the transition may comprise uncertainties related to the constructed age model and that an overshoot was indeed present, but was too abrupt to be preserved in the sedimentary record at the site.

It is unlikely that the site is representative for the Nordic Seas as a whole. Ice sheets and a lower sea level probably narrowed the Denmark Strait (Andrews, 2007). Intensive southward fluxes of cold and fresh surface waters in the EGC in a narrowed Denmark Strait could maintain a fresh water lid locally despite an overall thermocline reorganization in the Nordic Seas during the transition into GI8. In the modern setting, the EGC transports Polar Water and sea ice from the Arctic Ocean along the Greenland Margin (Rudels et al., 2002) and a temperature gradient with warmer intermediate waters persists in the western Denmark Strait in the modern summer season (Figure 3.2.B). I would argue that there was a gradual thermocline reorganization during the transition into GI8 in the Denmark Strait influenced by warmer waters in the Nordic Seas basin and that the transition was prolonged in the Denmark Strait due to a continuous EGC influence. During HS4, however, a stratification was maintained from the Nordic Seas and into the North Atlantic, and the results here support a northward retreat of the stratification. A stratified surface would imply that Atlantic waters penetrating the Nordic Seas become less ventilated and remain warm due to little heat loss to the atmosphere. The gradual temperature decrease and increasing ventilation over the transition implies more presence of better ventilated Atlantic water consistently reaching the North Icelandic Shelf during the interstadial.

7.4.4 Comparison with Irminger Sea records

Mg/Ca reconstructed temperatures on *N. pachyderma* in the Irminger Sea (green dot in Figure 7.4) indicate that near-surface waters were relatively warm (~4-5°C) during HS4 together with lower $\delta^{13}C$ indicating poorer ventilation (Jonkers et al., 2010a). In the early GI8, water temperatures rise to ~8°C together with an increase in the relative abundance of Atlantic planktonic species. The site of the study is influenced by the Irminger Current in the modern setting which later splits and transports warm water into the Denmark Strait in the NIIC. Whether the NIIC was active during interstadial/stadial phases, and whether it exerted important influence on the heat budget of the Nordic Seas is uncertain. Nevertheless, temperatures recorded at the site in the Irminger Sea (Jonkers et al., 2010a) correspond well with the temperature evolution found in this study. If continuously insulated from heat loss to the atmosphere on its northward path (by a strong halocline and sea ice), subsurface waters remain warm from the Irminger Sea to the Denmark Strait during HS4. On the other hand, Atlantic waters gradually lose heat during GI8 before reaching the study site resulting in colder temperatures in the Denmark Strait.

7.4.5 GI9

The earliest part of the record, including GI9, is characterized by a different pattern in the proxy records (Figure 5.6 and 7.3). Temperatures rise during GI9 with heavier $\delta^{13}C$. Meanwhile, $\delta^{18}O$ are the lowest in the record. However, it may be important to note that temperatures rise together with an increase in Mn/Ca towards values of ~0.3 mmol/mol which is well above the 0.1 mmol/mol contamination threshold determined by Boyle (1983) (Figure 7.3). The temperature may therefore be overestimated due to contamination by Mn-rich phases. Some samples in this interval were noted to be covered by light-reflecting crystals under the microscope.

The main objective in this thesis is to investigate the transition from HS4 to GI8. Furthermore, GI9 is a relatively short interstadial with relatively low amplitude and with a more gradual onset than neighboring transitions (Rasmussen et al., 2014). GI9 is barely noticeable in proxies in the Faroe-Shetland Channel (Dokken et al., 2013). As the amplitude changes of the corresponding magnetic susceptibility record over this interval is low, the age model is poorly constrained over the older part of the record. For these reasons, I will not go further into the discussion about this part of the record here.

7.4.6 Implications for abrupt climate change

Rapid demise of sea ice in the Nordic Seas region has become the prominent hypothesis in explaining the abruptness of the oxygen isotopic signal on Greenland and the associated ocean changes (Gildor and Tziperman, 2003; Li et al., 2010; Dokken et al., 2013; Rasmussen and Thomsen, 2004). From the planktonic data here one may only infer changes in the sea ice extent as a continuation of the arguments for a strong halocline. Because *N. pachyderma* is known to avoid fresh surface waters (Carstens et al., 1997), approaches to reconstruct sea ice extent by geochemical or assemblage methods on planktonic foraminifera are inherently indirect. A signal from a strong halocline would presumably be quite indistinguishable from that of accompanying sea ice, despite the arguments following the lower $\delta^{18}O_{sw}$ during HS4. However, I find it likely that sea ice accompanied the halocline interpreted here during HS4. The EGC transports sea ice from the Arctic towards the study site in the modern setting and was presumably the main southward conduit of sea ice also during stadial and interstadial phases. Furthermore, fresher water in the surface as interpreted here to be a facet of the HS4 is more susceptible to freezing due to its lower salt-content and overall colder conditions. Reduced storminess during in the Nordic Seas during stadials, as suggested by Li et al. (2010) and Dokken et al. (2013), would further promote sea ice growth by reducing the potential for mixing in the surface. Moreover, light benthic $\delta^{18}O$ during the stadial from the same core studied here has in parts been interpreted as an effect of dense and isotopically light brines that are formed due to the presence of sea ice (Sessford et al., 2018) in agreement with previous studies (Dokken and Jansen, 1999; Dokken et al., 2013).

Recent studies that have used more direct sea ice proxies (such as IP_{25}) have indicated perennial sea ice in the Nordic Seas during Heinrich Stadials and abrupt retreat at the beginning of interstadials (Hoff et al., 2016; Sadatzki et al. in press). On the other hand, Wary et al. (2017) argue for an annual sea ice cover during *interstadials* based on dinocyst assemblages. Because a diminished Nordic Seas sea ice extent may convincingly explain the abruptness of the transition into interstadials, more direct data to validate sea ice variations over stadial/interstadial phases should be explored.

While there are major oceanographic differences in the HS4 and GI8 suggested by the results of this thesis, the warming recorded at Greenland is much more abrupt than in the records of this site. Following the rationale that sea ice diminution and abrupt release of heat from the Nordic Seas led to the timing and amplitude of the temperature record on Greenland, these changes should have occurred east of the study site. Periodically during GI8, heat was most likely released from surface waters in the Denmark Strait as well, but seemingly without dramatic effects on the NGRIP temperature (Figure 7.3).

Beyond having implications for the warming into GIs, warmer subsurface waters during stadial phases may contribute to maintaining a strong halocline by melting of buttressing ice shelves or even have implications for the dynamics leading into ice shelf collapse (Marcott et al., 2011; Bassis et al., 2017).

Modern observations from Antarctica indicate that a warm subsurface can cause a destabilization of ice sheets by reducing buttressing of ice-shelves leading to an acceleration of ice streams (Rignot and Jacobs, 2002; Pritchard et al., 2012; Park et al., 2013).

The modern vertical profile of the Arctic Ocean is similar to the Nordic Seas during the stadial phase as interpreted here; throughout larger parts of the Arctic Ocean, a cap of fresh and cold surface waters overlies warmer and saltier waters below (Rudels et al., 1996; Lind et al., 2018). The Artic is currently experiencing the strongest warming on the planet and Arctic sea ice has retreated dramatically over the last decades (Carmack et al., 2015). Furthermore, warming in the Atlantic water subsurface has been recorded in the Arctic Ocean which is thought to be associated with the recent decrease in the polar sea ice extent (Polyakov et al., 2010). A recent study by Lind et al. (2018) show increasing temperatures in the Barents Sea which they link to decreasing influx of sea ice and surface fresh water which disrupts the stratification and increases mixing of underlying warmer and more saline Atlantic waters to the surface that further inhibits sea ice formation. On the other hand, river discharge from the major Eurasian rivers to the Arctic Ocean has increased over the last century (Peterson et al., 2002) which may contribute to reinforce the stratification. Thus, similarly to D-O cycles, the interplay between a fresher surface layer and underlying warmer waters may be consequential in the current climatic shift in the Arctic.

7.4.7 Conclusions

The “Cd-cleaning” and “full-cleaning” methods yield similar records in terms of Mg/Ca. Yet, the “full-cleaning” method lowers elemental ratios of Mg/Ca, Fe/Ca, Al/Ca, Mn/Ca to different extents, with the most pronounced effect on Al/Ca. The effect of the “full-cleaning” method on Mg/Ca seems to be non-uniform over the record and its effect may be influenced by environmental conditions during sedimentary deposition. When deciding on which cleaning protocol to follow in future studies it is important to keep in mind that the “full-cleaning” method requires more sample material due to dissolution and more work compared to less rigorous cleaning methods.

The stable isotopes records in this study, together with data from records in the south-east Nordic Seas and Greenland, suggests that Mg/Ca temperature reconstruction is feasible in the Denmark Strait and that it records temperature changes over stadial/interstadial phases.

The geochemical results of this study suggests that the Denmark Strait during HS4 was characterized by a well-stratified surface water column where fresher polar surface waters overlies warmer Atlantic waters. Mn/Ca records may further suggest poor ventilation of bottom waters which would be coherent with a stratified surface and limited convection.

Further, the lower overall reconstructed temperatures and higher values of oxygen and carbon isotopes during GI8 together suggest that the period was characterized by increased ventilation and heat loss to the atmosphere due to a disrupted stratification. However, large temperature variations during GI8 indicate that the local conditions were unstable, likely due to periodic reintroduction of a stratified surface layer.

Finally, the transition between HS4 and GI8 seems to be too slow in the Denmark Strait to be directly involved in the stored heat release and sea ice diminution hypothesized to cause the abruptness of the temperature increase observed on Greenland.

References

Aagard, K., Coachman, L.K., Carmack, E. 1981. On the halocline of the Arctic Ocean. *Deep Sea Research Part A. Oceanographic Research Papers,* 28, 529-545.

Ahn, J., Brook, E.J. 2008. Atmospheric CO_2 and Climate on Millennial Time Scales During the Last Glacial Period. *Science,* 322, 83-85.

Ahn, J., Brook, E.J. 2014. Siple Dome ice reveals two modes of millennial CO_2 change during the last ice age. *Nature communications,* 5, 3723.

Alonso-Cantabrana, H., von Caemmerer, S. 2016. Carbon isotope discrimination as a diagnostic tool for C4 photosynthesis in C3–C4 intermediate species. Journal of Experimental Botany 67, 3109–3121.

Alvarez-Solas, J., Charbit, S., Ritz, C., Paillard, D., Ramstein, G., Christophe, D. 2010. Links between ocean temperature and iceberg discharge during Heinrich events. *Nature geoscience,* 3, 122-126.

Anand, P., Elderfield, H., Conte, M.H. 2003. Calibration of Mg/Ca thermometry in planktonic foraminifera from a sediment trap time series. *Paleoceanography*, 18, 1050.

Andrews, J.T. 2007. The role of the Iceland Ice Sheet in the North Atlantic during the late Quaternary: a review and evidence from the Denmark Strait. *Journal of Quaternary Science,* 23, 2-20.

Arbuszewski, J., deMenocal, P., Kaplan, A., Farmer, E.C. 2010. On the fidelity of shell-derived $\delta^{18}O$ seawater estimates. *Earth and Planetary Science Letters,* 300, 185-196.

Augustin, L. EPICA community members. 2004. Eight glacial cycles from an Antarctic ice core. *Nature,* 429, 623-638.

Barker, S., Elderfield, H., 2002. Foraminiferal calcification response to glacial-interglacial changes in atmospheric CO_2. *Science,* 297, 833–836.

Barker, S., Greaves, M., Elderfield, H. 2003. A study of cleaning procedures used for foraminiferal Mg/Ca Paleothermometry. *Geochemistry, Geophysics, Geosystems*, 4, 8407.

Barker, S., Cacho, I., Benway, H., Tachikawa, K. 2005. Planktonic foraminiferal Mg/Ca as a proxy for past oceanic temperatures: a methodological overview and data compilation for Last Glacial Maximum. *Quaternary Science Reviews* 24, 821-834.

Bassis, J. N., Petersen, S.V., Cathles, L.M. 2017. Heinrich events triggered by ocean forcing and modulated by isostatic adjustment. *Nature*, 542, 332-334.

Bauch, D., Carstens, J., Wefer, G. 1997. Bauch, D., Carstens, J., & Wefer, G. (1997). Oxygen isotope composition of living Neogloboquadrina pachyderma (sin.) in the Arctic Ocean. *Earth and Planetary Science Letters*, 146, 47–58.

Bé, A.W.H., Tolderund, D.S. 1971. Distribution and ecology of living planktonic foraminifera in surface waters of the Atlantic and Indian oceans. *In*: Funnell, B.M., Riedel, W.R. (eds.) *Micropaleontology of the Oceans*. London: Cambridge University Press.

Bentov S., Brownlee C., Erez J. 2009. The role of seawater endocytosis in the biomineralization process in calcareous foraminifera. *Proceedings of the National Academy of Sciences of the United States of America.* 106, 21500–21504.

Bernard, J.M., Ostermann, D.R., Williams, D.S., Blanks, J.K. 2006. Comparison of two methods to identify live benthic foraminifera: A test between Rose Bengal and CellTracker Green with implications for stable isotope paleoreconstructions. *Paleoceanography and Paleoclimatology*, 21, PA4210.

Blunier, T., Brook, E.J. 2001. Timing of millennial-scale climate change in Antarctica and Greenland during the last glacial period. *Science,* 291, 109-112.

Bond, G., Heinrich, H., Broecker, W., Labeyrie, L., Mcmanus, J., Andrews, J., Huon, S., Jantschik, R., Clasen, S., Simet, C. 1992. Evidence for massive discharges of icebergs into the North Atlantic Ocean during the last glacial period. *Nature*, 360, 245–249

Bond, G., Broecker, W., Johnsen, S., McManus, J., Labeyrie, L., Jouzel, J., Bonani, G. 1993. Correlations between climate records from the North Atlantic sediments and Greenland Ice. *Nature,* 365, 143-147.

Boyle, E.A., 1981. Cadmium, zinc, copper and barium in foraminifera tests. *Earth and Planetary Science Letters*, 53, 11-35.

Boyle, E.A. 1983. Manganese carbonate overgrowths on foraminifera tests. *Geochimica et Cosmochimica Acta,* 47, 1815-1819.

Boyle, E.A., Keigwin, L.D. 1985. Comparison of Atlantic and Pacific paleochemical records for the last 215,000 years: changes in deep ocean circulation and chemical inventories. *Earth and Planetary Science Letters,* 76, 135-150.

Broecker, W.S., Peteet, D. M., Rind, D. 1985. Does the ocean–atmosphere system have more than one stable mode of operation, *Nature,* 315, 21-26.

Broecker, W.S., Bond, G., Klas, M., Bonani, G., Wolfli, W. 1990. A salt oscillator in the glacial Atlantic? 1. The concept. *Paleoceanography and Paleoclimatology,* 5, 469-477.

Broecker, W.S., 1991. The Great Ocean Conveyor. *Oceanography,* 4, 79-89.

Broecker, W.S. 1994. Massive iceberg discharges as trigger for global climate change. *Nature,* 372, 421-424.

Brown, S.J., Elderfield, H. 1996. Variations in Mg/Ca and Sr/Ca ratios of planktonic foraminifera caused by post depositional dissolution: Evidence of shallow Mg-dependent dissolution. *Paleoceanography and Paleoclimatology*, 11, 543-551.

Calvert, S.E., Pedersen, T.F. 1996. Sedimentary Geochemistry of Manganese: Implications for the Environment of Formation of Manganiferous Black Shale. *Economic Geology,* 91, 36-47.

Carmack, E., Polyakov, I., Padman, L., Fer, I., Hunke, E., Hutchings, J, Jackson, J., Kelley, D., Kwok, R., Layton, C., Melling, H., Perovich, D., Ruddick, B., Timmermans, M.L., Toole, J., Ross, T., Vavrus, S., Winsor, P. 2015. Toward Quantifying the Increasing Role of Oceanic Heat in Sea Ice Loss in the New Arctic. *Bulletin of the American Meterological Society*, 96, 2079-2105.

Carstens, J., Habbeln, D., Wefer, G. 1997. Distribution of planktic foraminifera at the ice margin in the Arctic (Fram Strait). *Marine Micropaleontology,* 29, 257-269.

Clark, I.D., Fritz, P. 1997. *Environmental isotopes in hydrogeology,* Boca Raton, Lewis Publishers.

Clark, P. U., Archer, D., Pollard, D., Blum, J.D., Rial, J.A., Brovkin, V., Mix, A.C., Pisias, N.G., Roy. 2006. The middle Pleistocene transition: characteristics, mechanisms, and implications for long-term changes in atmospheric pCO_2. *Quaternary Science Reviews,* 25, 3150-3184.

Clarke, F.W., Wheeler, W.C. 1922. The Inorganic Constituents of Marine Invertebrates. *US Geological Survey Professional Paper 124*. Washington, DC. Department of the Interior.

Cronin, T. M. 2010. *Paleoclimates: understanding climate change past and present,* N.Y.: Columbia University Press.

Curry, W. B., Oppo, D.W. 1997. Synchronous, high-frequency oscillations in tropical sea surface temperatures and North Atlantic Deep Water production during the last glacial cycle, *Paleoceanography,* 12, 1 –14.

Dansgaard, W., Johnsen, S.J., Clausen H.B., Dahl-Jensen, D., Gundestrup, N.S., Hammer, C.U., Hvidberg, C.S., Steffensen, J.P., Sveinbjörnsdottir, A.E., Jouzel, J., Bond, G. 1993. Evidence for general instability of past climate from a 250-kyr Ice-core record. *Nature,* 364, 218-220.

Darling, K.F., Kucera, M., Wade, C.M. 2007. Global molecular phylogeography reveals persistent Arctic circumpolar isolation in a marine planktonic protist. *Proceedings of the National Academy of Sciences of the United States of America,* 104, 5002-5007.

Dekens, P.S., Lea, D.W., Pak, D.K., Spero, H.J. 2002. Core top calibration of Mg/Ca in tropical foraminifera: Refining paleotemperature estimation. *Geochemistry, Geophysics, Geosystems*, 3, 1-29.

Dickson, R. R., Lazier, J., Meincke, J., Rhines, P., Swift, J. 1996. Long-term co-ordinated changes in the convective activity of the North Atlantic, *Progress in Oceanography,* 38, 241-295

Dieckmann, G., Spindler, M., Lange, M. A., Ackley, S. F., Eicken, H. 1991. Antarctic sea ice: a habitat for the foraminifer *Neogloboquadrina pachyderma*, *Journal of Foraminiferal Research,* 21, 182-189

Dokken, T. M., Jansen, E. 1999. Rapid changes in the mechanism of ocean convection during the last glacial period, *Nature,* 401, 458–461.

Dokken, T., Nisancioglu, K.H., Li, C, Battisti, D.S., Kissel, C. 2013. Dansgaard-Oeschger cycles: Interactions between ocean and sea ice intrinsic to the Nordic seas. *Paleoceanography,* 28, 491-502.

Dunn, S. 2016. Gas Source Mass Spectrometry: *Stable Isotope Geochemistry* [Online]. Available: https://serc.carleton.edu/research_education/geochemsheets/techniques/gassourcemassspec.html [Accessed 01.11.2018].

Duplessy, J.C., Laberyrie, L., Arnold, M., Paterne, M., Duprat, J., van Weering, T.C.R. 1992. Changes in surface salinity of the North Atlantic Ocean during the last deglaciation. *Nature*, 358, 485-488.

Elderfield, H., Ganssen, G.M. 2000. Past temperature and $\delta^{18}O$ of surface ocean waters inferred from foraminiferal Mg/Ca ratios. *Nature*, 405, 442-445.

Elderfield, H., Vautravers, M., Cooper, M. 2002. The relationship between shell size and Mg/Ca, Sr/Ca, $\delta^{18}O$, and $\delta^{13}C$ of species of planktonic foraminifera. *Geochemistry, Geophysics, Geosystems,* 3, 1-13.

Emiliani, C. 1955. Pleistocene Temperatures. *The Journal of Geology,* 63, 538-578.

Epstein, S., Buchsbaum, R., Lowenstam, H. A. & Urey, H. C. 1953. Revised carbonate-water isotopic temperature scale. *Geological Society of America Bulletin*, 64.

Erez, J. 2003. The source of ions for biomineralization in foraminifera and their implications for paleoceanographic proxies. *Reviews in Mineralogy and Geochemistry,* 54, 115-149.

Eynaud, F. 2011. Planktonic foraminifera in the Arctic: Potentials and issues regarding modern quaternary populations. IOP Conference Series, *Earth and Environmental Science,* 14, 012005.

Ezat, M.H., Rasmussen, T.L., Groeneveld, J. 2016. Reconstruction of hydrographic changes in the southern Norwegian Sea during the past 135 kyr and the impact of different foraminiferal Mg/Ca cleaning protocols. *Geochemistry, Geophysics, Geosystems,* 17, 3420-3436.

Ezat, M.H., Rasmussen, T.L., Hönisch, B., Groeneveld, J., deMenocal, P. 2017. Episodic release of CO_2 from the high-latitude North Atlantic Ocean during the last 135 kyr. *Nature communications*, 6, 14498.

Faure, G. 1986. *Principles of isotope geology,* N.Y.: Wiley; 2nd edition.

Flückiger, J., Blunier, T., Stauffer, B., Chappellaz, J., Spahni, R., Kawamura, K., Schwander, J., Stocker, T. F., Dahl-Jensen, D. 2004. N_2O and CH_4 variations during the last glacial epoch: Insight into global processes. *Global Biogeochemical Cycles*, 18, GB1020.

Galbraith, E.D., Kwon, E.Y., Bianchi, D., Hain, M.P., Sarmiento, J.L. 2015. The impact of atmospheric pCO_2 on carbon isotope ratios of the atmosphere and ocean. *Global Biogeochemical Cycles,* 29, 307-324.

Ganopolski, A., Rahmstorf, S. 2001. Rapid changes of glacial climate simulated in a coupled climate model. *Nature*, 409, 153-158.

Garrels, R.M., Christ, C.L. 1965. *Solutions, minerals and equilibria.* N.Y.: Harper & Row.

Gebby, G., Peterson, C.D., Lisiecki, L.E., Spero, H.J. 2015. Global-mean marine $\delta^{13}C$ and its uncertainty in a glacial state estimate. *Quaternary Science Reviews,* 125, 144-159.

Genty, D., Blamart, D., Ouahdi, R., Gilmour, M., Baker, A., Jouzel, J., Van-Exter, S. 2003. Precise dating of Dansgaard–Oeschger climate oscillations in western Europe from stalagmite data, *Nature,* 421, 833-837.

Gildor, H., Tziperman, E. 2003. Sea-ice switches and abrupt climate change. *Philosophical Transactions. Series A, Mathematical, physical and engineering sciences,* 361, 1935-1944.

Godwin, H. 1962. Half-life of radiocarbon. *Nature*, 195, 984.

Gonneea, M, E., Paytan, A. 2006. Phase associations of barium in marine sediment. *Marine Chemistry*, 100, 124-135.

Greaves, M. et al. 2008. Interlaboratory comparison study of calibration standards for foraminiferal Mg/Ca thermometry. *Geochemistry, Geophysics, Geosystems*, 9, 1525-2027.

Griffith, E.M., Paytan, A. 2012. Barite in the ocean- occurrence, geochemistry and palaeoceanographic applications. *Sedimentology,* 59, 1817-1835.

Guillevic, M., Bazin, L., Landais, A., Stowasser, C., Masson-Delmotte, V., Blunier, T., Eynaud, F., Falourd, S., Michel, E., Minster, B., Prié, F., Vinther, B.M. 2014. Evidence for a three-phase sequence during Heinrich Stadial 4 using a multiproxy approach based on Greenland ice core records. *Climate of the Past*, 10, 2115-2133.

Haley, B.A., Klinkhammer, G.P. 2002. Development of a flow-through system for cleaning and dissolving foraminiferal tests. *Chemical Geology,* 185, 51-69.

Hansen, B., Østerhus, S. 2000. North Atlantic-Nordic Seas exchanges. *Progress in Oceanography*, 45, 109-208.

Hansen, B., Østerhus, S., Quadfasel, D., Turrell, W. 2004. Already the day after tomorrow? *Science,* 305, 953–954.

Hasenfratz, A.P., Martínez-García, A., Jaccard, S.L., Vance, D., Wälle, M., Greaves, M., Haug, G.H. 2017. Determination of the Mg/Mn ratio in foraminiferal coatings: An approach to correct for Mg/Ca temperatures for Mn-rich contaminant phases. *Earth and Planetary Science Letters,* 457, 335-347.

Hasum, K., Hald, M. 2012. Arctic planktic foraminiferal assemblages: Implications for subsurface temperature reconstructions. *Marine Micropaleontology,* 96-97, 38-47.

Heinrich, H. 1988. Origin and consequences of cyclic ice rafting in the Northeast Atlantic Ocean during the past 130,000 years. *Quaternary Research,* 29, 142-152.

Hemming, S.R. 2004. Massive late Pleistocene detritus layers of the North Atlantic and their global climate imprint. *Reviews in Geophysics,* 42, RG1005

Hewitt, G. 2000. The genetic legacy of the Quaternary ice ages. *Nature,* 405, 907-913.

Hoefs, J. 2009. *Stable Isotope Geochemistry*. Berlin, Springer Berlin Heidelberg; 6th edition.

Hoefs, J. 2018. *Stable isotope Geochemistry*. Springer International Publishing, 8th edition.

Hoff, U., Rasmussen, T.L., Stein, R., Ezat, M.M., Fahl, K. 2016. Sea ice and millennial-scale climate variability in the Nordic seas 90 kyr to present. *Nature communications,* 7, 12247.

Hoogakker, B.A.A., Elderfield, H., Schmiedl, G., McCave, I.N., Rickaby, R.E.M. 2015. Glacial–interglacial changes in bottom-water oxygen content on the Portuguese margin. *Nature geoscience,* 8, 40-43.

Hopkins, T.S. 1991. The GIN Sea- A synthesis of its physical oceanography and literature review 1972-1985. *Earth Science Reviews,* 30, 175-318

Horner, T.J., Pryer, H.V., Nielsen, S.G., Crockford, P.W., Gauglitz, J.M., Wing, B.A., Ricketts, R.D. 2017. Pelagic barite precipitation at micromolar ambient sulfate. *Nature communications*, 8, 1342.

Huber, C., Leuenberger, M., Spahni, R., Flückiger, J., Schwander, J., Stocker, T.F., Johnsen, S., Landais, A., Jouzel, J. 2006. Isotope calibrated Greenland temperature record over Marine Isotope Stage 3 and its relation to CH_4. *Earth and Planetary Science Letters*, 243, 504-519.

Hurrell, J.W., Kushnir, Y., Ottesen, G., Visbeck, M. 2003. *The North Atlantic Oscillation. Climatic Significance and Environmental Impact,* 134. Washington D.C: American Geophysical Union.

Imbrie, J., Berger, A., Boyle, E. A., Clemens, S. C., Duffy, A., Howard, W. R., Kukla, G., Kutzbach, J., Martinson, D. G., Mcintyre, A., Mix, A. C., Molfino, B., Morley, J. J., Peterson, L. C., Pisias, N. G., Prell, W. L., Raymo, M. E., Shackleton, N. J. & Toggweiler, J. R. 1993. On the structure and origin of major glaciation cycles 2. The 100,000-year cycle. *Paleoceanography*, 8, 699-735.

IAEA. 1995. *NBS 18, Calcite* [Online]. Available: https://nucleus.iaea.org/rpst/referenceproducts/referencematerials/Stable_Isotopes/13C18and7Li/NBS_18.htm (Accessed 13.11.2017)

IPCC, 2013: Annex III: Glossary [Planton, S. (ed.)]. In: Climate Change 2013: The Physical Science Basis. Contribution of Working Group I to the Fifth Assessment Report of the Intergovernmental Panel on Climate Change [Stocker, T.F., D. Qin, G.-K. Plattner, M. Tignor, S.K. Allen, J. Boschung, A. Nauels, Y. Xia, V. Bex and P.M. Midgley (eds.)]. Cambridge University Press, Cambridge, United Kingdom and New York, NY, USA.

Isachsen, P.E., Sørlie, S.R., Mauritzen, C., Lydersen, C., Dodd, P., Kovacs, K.M. 2014. Upper-ocean hydrography of the Nordic Seas during the International Polar Year (2007-2008) as observed by instrumental seals and Argo floats. *Deep Sea Research Part 1: Oceanographic Research Papers,* 93, 41-59.

Jaccard, S.L., Galbraith, E.D., Martínez-García, A., Anderson, R.F. 2016. Covariation of deep Southern Ocean oxygenation and atmospheric CO_2 through the last ice age. *Nature,* 530, 207-210.

Jensen, M.F., Nisancioglu, K.H., Spall, M.A. 2018. Large Changes in Sea Ice Triggered by Small Changes in Atlantic Water Temperature. Journal of Climate, 31, 4847-4863.

Johannessen, T., Janse, E., Flatøy, A., Ravelo, A.C. 1994. The relationship between surface water masses, oceanographic fronts and paleoclimatic proxies in surface sediments of the Greenland, Iceland, Norwegian Seas. In: Zahn, R., Pedersen, T.F., Kaminski, M.A., Labeyrie, L.D (eds.) *Carbon Cycling in the Glacial Ocean: Constraints on the Ocean's Role in Global Change*. NATO ASI Series, 17, 61-84.

Jonkers, L., Moros, M., Prins, M.A., Dokken, T., Dahl, C.A., Dijkstra, N., Perner, K., Brummer, G.J.A. 2010a. A reconstruction of sea surface warming in the northern North Atlantic during MIS 3 ice-rafting events. *Quaternary Science Reviews,* 29, 1791-1800.

Jonkers, L., Brummer, G. J. A., Peeters, F. J. C., Van Aken, H. M. & De Jong, M. F. 2010b. Seasonal stratification, shell flux, and oxygen isotope dynamics of left-coiling *N. pachyderma* and *T. quinqueloba* in the western subpolar North Atlantic. *Paleoceanography,* 25, PA2204.

Jonkers, L., Jiménez-Amat, P., Mortyn, G.P., Brummer, G.J.A. 2013. Seasonal Mg/Ca variability of *N. pachyderma* (s) and *G. bulloides*: Implications for seawater temperature reconstruction. *Earth and Planetary Science Letters,* 476, 137-144.

Jónsson, S., Valdimarsson, H., 2005. The flow of Atlantic water to the North Icelandic Shelf and its relation to the drift of cod larvae. *ICES Journal of Marine Science*, 62, 1350-1359.

Jouzel, J., Masson-Delmotte, V., Cattani, O., Falourd, S., Stievenard, M., Stenni, B., Longinelli, A., Johnsen, S.J., Steffensen, J.P., Petit, J.R., Schwander, J., Souches, R., Barkov, N.I. 2001. A new 27 ky high resolution East Antarctic climate record. *Geophysical Research Letters,* 28, 3199-3202.

Jouzel, J., Masson-Delmotte, V., Cattani, O., Dreyfus, G., Falourd, S., Hoffmann, G., Minster, B., Nouet, J, ., Barnola, J.M., Chappellaz, J., Fischer, H., Gallet, J.C., Johnsen, S., Leuenberger, M., Loulergue, L., Luethi, D., Oerter, H., Parrenin, F., Raisbeck, G., Raynaud, D., Schwander, J., Spahni, R., Souchez, R., Selmo, E., Schilt, A., Steffensen, J.P., Stenni, B., Stauffer, B., Stocker, T., Tison, J.-L., Werner, M., Wolff, E.W. 2007a. Orbital and millennial Antarctic climate variability over the last 800,000 years. *Science* 317, 793–796.

Jouzel, J., Stiévenard, M., Johnson, S.J., Laindais, A., Masson-Delmotte, V., Sveinbjornsdottir, A., Vimeux, F., von Grafenstein, U., White, J.W.C. 2007b. The GRIP deuterium-excess record. *Quaternary Science Reviews,* 26, 1-17.

Katz, A. 1973. The interaction of magnesium with calcite during crystal growth at 25–90°C and one atmosphere. *Geochimica et Cosmochimica Acta*, 37, 1563-1578.

Katz, M.E., Cramer, B.S., Franzese, A., Hönisch, B., Miller, K.G., Rosenthal, Y., Wright, J.D. 2010.Traditional and emerging geochemical proxies in foraminifera. *Journal of Foraminiferal Research*, 40, 165-192.

Kimoto, K. 2015. Planktonic Foraminifera. *In*: Ohtsuka S., Suzaki T., Horiguchi T., Suzuki N., Not F. (eds.) *Marine Protists.* Tokyo: Springer.

Kisakürek, B., Eisenhauer, A., Bohm, F., Garbe-Schonberg, Erez, J. 2008. Controls on shell Mg/Ca and Sr/Ca in cultured planktonic foraminifera, Globigerionoides ruber (white). *Earth and Planetary Science Letters,* 273, 260-269.

Kissel, C., Laj, C., Labeyrie, L., Dokken, T., Voelker, A.H.L., Blamart, D. 1999. Rapid climatic variations during marine isotopic stage 3: magnetic analysis of sediments from Nordic Seas and North Atlantic, *Earth and Planetary Science Letters*, 171, 489-502.

Kohfeld, K.E., Fairbanks, R.G., Smith, S.L., Walsh, I.D. 1996. Neogloboquadrina pachyderma (sinistral coiling) as paleoceanographic tracers in polar oceans: Evidence from Northeast Water Polynya plankton tows, sediment traps, and surface sediments. *Paleoceanography,* 11, 679-699.

Köhl, A., Käse, R.H., Stammer, D., Serra, N. 2007. Causes of Changes in the Denmark Strait Overflow. *Journal of Physical Oceanography*, 37, 1678-1696.

Kozdon, R., Ushikubo, T., Kita, N.T., Spicuzza, M., Valley, J.W. 2009. Intratest oxygen isotope variability in the planktonic foraminifer *N. pachyderma*: Real vs. apparent vital effects by ion microprobe. *Chemical Geology*, 258, 327-337.

Koziol, A.M., Newton, R.C. 1995. Experimental determination of the reactions magnesite + quartz=periclase +CO_2 and the enthalpies of formation of enstatite and magnesite. *American Mineralogist*, 80, 1252- 1260.

Krauss, W. 1986. The North Atlantic Current. *Journal of Geophysical Research,* 91, 5061-5074.

Kuhlbrodt, T., Griesel, A., Montoya, M., Levermann, A., Hofmann, M. & Rahmstorf, S. 2007. On the driving processes of the Atlantic meridional overturning circulation. *Reviews of Geophysics*, 45, RG2001.

Kucera, M. 2007. Planktonic Foraminifera as Tracers of Past Oceanic Environments. *In*: Hillaire-Marcel, C. & De Vernal, A. (eds.) *Developments in Marine Geology: Proxies in Late Cenozoic Paleoceanography*. Burlington: Elsevier Science.

Laj, C. 2003. Paleomagnetic of sediment core PS2644-5, doi: https://doi.org/10.1594/PANGAEA.118604.

Laskar, J., Robutel, P., Joutel, F., Gastineau, M., Correia, A.C.M., Levrard, B. 2004. A long-term numerical solution for the insolation quantities of the Earth. *Astronomy and Astrophysics,* 428, 261-285.

Lea, D.W., Boyle, E.A. 1993. Determination of carbonate-bound barium in foraminifera and corals by isotope dilution plasma-mass spectrometry. *Chemical Geology*, 103, 74-84.

Lea, D.W., Mashiotta, T.A., Spero, H.J. 1999. Controls on magnesium and strontium uptake in planktonic foraminifera determined by live culturing. *Geochimica et Cosmochimica Acta,* 63, 2369-2379.

Lea, D.W., Pak, D.K., Spero, H.J., 2000. Climate impact of late Quaternary equatorial Pacific sea surface temperature variations. *Science,* 289, 1719–1724.

Lea, D.W. 2014. Elemental and Isotopic Proxies of Past Ocean Temperatures. *In*: Holland H.D. and Turekian K.K. (eds.) *Treatise on Geochemistry*, 2nd Edition, 8, 373-397. Oxford: Elsevier.

Leduc, G., Vidal, L., Kazuyo, T., Rostek, F., Sonzogni, C., Beufort, L., Bard, E. 2007. Moisture transport across Central America as a positive feedback on abrupt climatic changes. *Nature,* 445, 908–911.

Li, C., Battisti, D.S., Schrag, D.P., Tziperman, E. 2005. Abrupt climate shifts in Greenland due to displacements of the sea ice edge. *Geophysical Research Letters,* 32*,* LI19702.

Li, C., Battisti, D.S. 2008. Reduced Atlantic Storminess during Last Glacial Maximum: Evidence from a Coupled Climate Model. Journal of Climate, 21, 3561-3579.

Li, C., Battisti, D.S., Bitz, C.M. 2010. Can North Atlantic sea ice anomalies account for Dansgaard-Oeschger climate signals?, *Journal of Climate,* 23, 5457–5475.

Lind, S., Ingvaldsen, R.B., Furevik, T. 2018. Arctic warming hotspot in the northern Barents Sea linked to declining sea-ice import. *Nature climate change,* 8, 634-639.

Lisiecki, L.E., Raymo, M.E. 2005. A Pliocene-Pleistocene stack of 57 globally distributed benthic δ^{18}O records. *Paleoceanography and Paleoclimatology,* 20, PA1003.

Loeng, H. 1991. Features of the physical oceanographic conditions of the Barents Sea. *Polar Research*, 10, 5-18.

Logemann, K., Harms, I. 2006. High resolution modelling of the North Icelandic Irminger Current (NIIC). *Ocean Science*, 2, 291-304.

Lüthi, D., Le Floch, M., Bereiter, B., Blunier, T., Barnola, J-M., Siegenthaler, U., Raynaud, D., Jouzel, J., Fischer, H., Kawamura, K., Stocker, T.S. 2008. High-resolution carbon dioxide concentration record 650,000–800,000 years before present. *Nature*, 453, 379-382.

Lynch-Stieglitz, J., Stocker, T.F., Broecker, W.S., Fairbanks, R.G. 1995. The influence of air-sea exchange on the isotopic composition of oceanic carbon: Observations and modeling. *Global biogeochemical cycles*, 9, 653-665.

Macayeal, D. R. 1993. Binge/purge oscillations of the Laurentide ice sheet as a cause of the North Atlantic's Heinrich events. *Paleoceanography,* 8, 775-784.

Macdonald, R.W., Paton, D.W., Carmack W.C., Omstedt, A. 1995. The freshwater budget and under-ice spreading of Mackenzie River water in the Canadian Beaufort Sea based on salinity and ^{18}O/^{16}O measurements in water and ice. *Journal of Geophysical Research*, 100C, 895-919.

Macrander, A., Valdimarsson, H., Jónsson, S. 2014. Improved transport estimate of the East Icelandic Current 2002–2012. *Journal of Geophysical Research: Oceans,* 119, 3407-3424.

Marcott, S.A., Clark, P.U., Padman, L., Klinkhammer, G.P., Springer, S.R., Liu, Z., Otto-Bliesner, B.L., Carlson, A.E., Ungerer, A., Padman, J., He, F., Cheng, J., Schmittner, A. 2011. Ice-shelf collapse from subsurface warming as a trigger for Heinrich events. *Proceedings of the National Academy of Sciences of the United States of America,* 108, 13415-13419.

Martin, P.A., Lea, D.W. 2002. A simple evaluation of cleaning procedures on fossil benthic foraminiferal Mg/Ca. Geochemistry, Geophysics, Geosystems, 3, 1-8.

Mashiotta, T.A., Lea, D.W., Spero, H.J. 1999. Glacial-interglacial changes in Subantarctic sea surface temperature and d^{18}O- water using foraminiferal Mg. *Earth and Planetary Science Letters,* 170, 417-432.

Masson-Delmotte, V., Jouzel, J., Landais, A., Stievenard, M., Johnsen, S.J., White, J.W., Werner, M., Sveinbjornsdottir, A., Fuhrer, K. 2005. GRIP deuterium excess reveals rapid and orbital-scale changes in Greenland moisture origin. *Science*, 309, 118-121.

Mathien-Blard, E., Bassinot, F. 2009. Salinity bias on the foraminifera Mg/Ca thermometry: Correction procedure and implications for past ocean hydrographic reconstructions. *Geochemistry, Geophysics, Geosystems,* 10, Q12011.

McManus, J.F., Oppo, D.W., Cullen, J.L. 1999. A 0.5-Million-Year Record of Millennial-Scale Climate Variability in the North Atlantic. *Science*, 283, 971-957.

Meland, M. Y., Jansen, E., Elderfield, H. 2005. Constraints on SST estimates for the northern North Atlantic/Nordic Seas during the LGM. *Quaternary Science Reviews,* 24, 835-852.

Meland, M.Y., Jansen, E., Elderfield, H., Dokken, T.M., Olsen, A., Bellerby, R.G.J. 2006. Mg/Ca ratios in the planktonic foraminifer *Neogloboquadrina pachyderma (sinistral)* in the northern North Atlantic/Nordic Seas. *Geochemistry, Geophysics, Geosystems,* 7, Q06P14.

Milankovitch, M. 1941. Kanon der Erdbestrahlung und seine Andwendung auf das Eiszeiten-problem. *Royal Serbian Academy*: Belgrade. (Canon of insolation and the ice-age problem, English translation by Israel Program for Scientific Translations, Jerusalem, 1969).

Mook, Q.G., Bommerson, J.C., Staverman, W.H. 1974. Carbon isotope fractionation between dissolved bicarbonate and gaseous carbon dioxide. *Earth and Planetary Science Letters,* 22, 169-176.

Mucci, A. 1987. Influence of temperature on composition of magnesian calcite overgrowth precipitated from seawater. *Geochimica et Cosmochimica Acta,* 51, 1977-1984.

Nave, S., Labeyrie, L., Gherardi, J., Caillon, N., Cortijo, E., Kissel, C., Abrantes, F. 2007. Primary productivity response to Heinrich events in the North Atlantic Ocean and Norwegian Sea. *Paleoceanography,* 22, PA3216.

Nürnberg, D., 1995. Magnesium in tests of Neogloboquadrina pachyderma (sinistral) from high northern and southern latitudes. *Journal of Foraminiferal Research,* 25, 350–368.

Nürnberg, D., Bijma, J., Hemleben, C., 1996. Assessing the reliability of magnesium in foraminiferal calcite as a proxy for water mass temperatures. *Geochimica et Cosmochimica Acta*, 60, 803–814.

Olsen, A., Key, R.M., van Heuven, S., Lauvset, S.K., Velo, A., Lin, X., Schirnick, C., Kozyr, A., Tanhua, T., Hoppema, M., Jutterström, S., Steinfeldt, R., Jeansson, E., Ishii, M., Pérez, F.F., Suzuki, T. 2016. The Global Ocean Data Analysis Project version 2 (GLODAPv2) – an internally consistent data product for the world ocean. *Earth System Science Data,* 8, 297-323.

Omoori, T., Kaneshima, H. Maezato, T. 1987. Distribution coefficient of Mg^{2+} ions between calcite and solution at 10-50°C. *Marine Chemistry*, 20, 327-336.

Park, J. W., Gourmelen, N., Shepherd, A., Kim, S.W., Vaughan, D. G., Wingham, D. J. 2013. Sustained retreat of the Pine Island Glacier. *Geophysical Research Letters*, 40, 2137-2142.

Pausata, F.S.R., Li, C., Wettstein, J.J., Kageyama, M., Nisancioglu, K.H. 2011. The key role of topography in altering North Atlantic atmospheric circulation during the last glacial period. *Climate of the Past*, 7, 1089-1101.

Paytan, A., Mearon, S., Cobb, K., Kastner, M. 2002. Origins of marine barite deposits: Sr and S isotope characterization. *Geology,* 30, 747-750.

Pena, L, D., Calvo, E., Cacho, I., Eggins, S., Pelejero, C. 2005. Identification and removal of Mn-Mg-rich contaminant phases on foraminiferal tests: Implications for Mg/Ca past temperature reconstructions. *Geochemistry, Geophysics, Geosystems*, 6, Q09P02.

Pena, L.D., Cacho, I., Calvo, E., Pelejero, C., Eggins, S., Sadekov, A. 2008. Characterization of contaminant phases in foraminifera carbonates by electron microprobe mapping. *Geochemistry, Geophysics, Geosystems, 9,* Q07012.

Peterson, B.J., Holmes, R.M., McClelland, J.W., Vörösmarty, C.J., Lammers, R.B., Shiklomanov, A.I., Shiklomanov, I.A., Rahmsorf, S. 2002. Increasing River Discharge to the Arctic Ocean. *Science,* 298, 2171-2173.

Pflaumann, U., Duprat, J., Pujol, C. & Labeyrie, L. D. 1996. SIMMAX: A modern analog technique to deduce Atlantic sea surface temperatures from planktonic foraminifera in deep-sea sediments. *Paleoceanography,* 11, 15-36.

Pflaumann, U., Sartnthein, M., Chapman, M., d'Abreu, L., Funnell, B., Huels, M., Kiefer, T., Maslin, M., Schulz, H., Swallow, J., van Kreveld, S., Vautravers, M., Vogelsang, E., Weinelt, M. 2003. Glacial North Atlantic: Sea surface conditions reconstructed by GLAMAP 2000. *Paleoceanography and Paleoclimatology*, 18, 1065.

Phleger, F.B. 1939. Foraminifera of submarine cores from the continental slope. *GSA Bulletin,* 50, 1395-1422.

Polyakov, I.V., Tomoknov, L.A., Alexeev, V.A., Bacon, S., Dmitrenko, I.A., Fortier, I.E., Gascard, J-C., Hansen, E., Ivanov, V.V., Laxon, S., Mauritzen, C., Perovich, D.,Shimada, K., Simmons, H.L., Sokolov, V.T., Steele, M., Toole, J. 2010. Arctic Ocean Warming Contributes to Reduced Polar Ice Cap. *Journal of Physical Oceanography*, 40, 2743-2756.

Pritchard, H.D., Ligtenberg, S.R.M., Fricker, H.A., Vaughan, D.G., van den Broecke, M.R., Padman, L. 2012. Antarctic ice-sheet loss driven by basal melting of ice shelves. *Nature, 484,* 502-505.

Rasmussen, S.O., Bigler, M., Blockley, S.P., Blunier, T., Buchardt, S.L., Clausen, H.B., Cvijanovic, I., Dahl-Jensen, D., Johnsen, S.J., Fischer, H., Gkinis, V., Guillevic, M., Hoek, W.Z., Lowe, J.J., Pedro, J.B., Popp, T., Seierstad, I.K., Steffensen, J.P., Svensson, A.M., Vallelonga, P., Vinther, B.M., Walker, M.J.C., Wheatley, J.J., Winstrup, M. 2014. A stratigraphic framework for abrupt climatic changes during the Last Glacial period based on three synchronized Greenland ice-core records: refining and extending the INTIMATE event stratigraphy. *Quaternary Science Reviews*, 106, 14-28.

Rasmussen, T.L., Thomsen, E., van Weering, T.C.E., Labeyrie, L. 1996. Rapid changes in surface and deep water conditions at the Faeroe Margin during the last 58,000 years. *Paleoceanography and Paleoclimatology,* 11, 757-771.

Rasmussen, T.L., Thomsen, E. 2004. The role of then North Atlantic Drift in the millennial timescale glacial climate fluctuations. *Palaeogeography, Palaeoclimatology, Palaeoecology,* 210, 101-116.

Rasmussen, T.L., Thomsen, E. 2009. Ventilation changes in intermediate water on millennial time scales in the SE Nordic seas, 65-14 kyr BP. Geophysical Research Letters, 36, L01601.

Ravelo, A.C., Hillaire-Marcel, C. 2007. The use of Oxygen and Carbon isotopes of Foraminifera in Paleoceanography. *In*: Hillaire-Marcel, C. & De Vernal, A. (eds.) *Developments in Marine Geology: Proxies in Late Cenozoic Paleoceanography*. Burlington: Elsevier Science.

Raymo, M.E., Ganley, K. G., Carter, S., Oppo, D.W., McManus, J. 1998. Millennial-scale climate instability during the early Pleistocene epoch. *Nature,* 392, 699-702.

Regenberg, M., Nürnberg, D., Schönfeld, J., Reichart, G.J. 2007. Early diagenetic overprint in Caribbean sediment cores and its effect on the geochemical composition of planktonic foraminifera. *Biogeosciences*, 4, 957-973.

Regenberg, M., Regenberg, A., Garbe-Schönberg, Lea, D.W. 2014. Global dissolution effects on planktonic foraminiferal Mg/Ca ratios controlled by the calcite-saturation state of bottom waters. *Paleoceanography,* 19, 127-142.

Reimer, P.J., Baillie, M.G.L., Bard, E., Bayliss, A., Beck, J.W., Blackwell, P.G., Ramsey, C.B., Buck, C.E., Burr, G.S., Edwards, R.L., Friedrich, R.L., Grootes, P.M., Guilderson, T.P., Hajdas, I., Heaton, T.J., Hogg, A.G., Hughen, K.A., Kaiser, K.F., Kromer, B., McCormac, F.G., Manning, S.W., Reimer, R.W., Richards, D.A., Southon, J.R., Talamo, S., Turney, C.S.M., van der Plicht, J., Weyhenmeyer, C.E. 2009. IntCal09 and Marine09 Radiocarbon Age Calibration Curves, 0-50,000 Years cal BP. *Radiocarbon,* 51, 1111-1150.

Rignot, E., Jacobs, S.S. 2002. Rapid Bottom Water Widespread near Antarctic Ice Sheet Grounding Lines. *Science,* 296, 2020-2023.

Riveiros, N.V., Govin, A., Waelbroeck, C., Mackensen, A., Michel, E., Moreira, S., Bouinot, T., Caillon, N., Orgun, A., Brandon, M. 2016. Mg/Ca thermometry in planktic foraminifera: Improving paleotemperature estimations for G. bulloides and N. pachyderma left. *Geochemistry, Geophysics, Geosystems,* 17, 1249-1264.

Rohling, E. J., Cooke, S. 1999. Modern foraminifera: Stable oxygen and carbon isotopes in foraminiferal carbonate shells. *In*: Sen Gupta, B.K. (ed.) *Modern Foraminifera*. Dordrecht: Kluwer.

Rohling E.J. 2013. Oxygen Isotope Composition of Seawater. *The Encyclopedia of Quaternary Science*, 2, 915-922.

Romanek, C.S., Grossman, E.L., Morse, J.W. 1992. Carbon isotopic fractionation in synthetic aragonite and calcite: Effects of temperature and precipitation rate. *Geochimica et Cosmochimica Acta,* 56, 419-430.

Rosenthal, Y., Boyle, E.A. 1993. Factors controlling the fluoride content of planktonic foraminifera: an evaluation of its paleoceanographic applicability. *Geochimica et Cosmochimica Acta*, 57, 335-346.

Rosenthal, Y., Boyle E.A., Slowey, N. 1997. Temperature control on the incorporation of magnesium, strontium, fluorine, and cadmium into benthic foraminiferal shells from Little Bahama Bank: Prospects for thermocline paleoceanography, *Geochimica et Cosmochimica Acta*, 61, 3633–3643.

Rosenthal, T., Field, M.P., Sherrell, R.M. 1999. Precise Determination of Element/Calcium Ratios in Calcareous Samples Using Sector Field Inductively Coupled Plasma Mass Spectrometry. *Analytical Chemistry,* 71, 3248-3253.

Rosenthal, Y., Lohmann, G.P., Lohmann, K.C., Sherrell, R.M., 2000. Incorporation and preservation of Mg in Globigerinoides sacculifer: implications for reconstructing the temperature and O-18/O-16 of seawater. *Paleoceanography*, 15, 135–145.

Ruddiman, W. F. 1977. Late Quaternary deposition of ice-rafted sand in the subpolar North Atlantic (lat 40 degrees to 65 degrees N). *Geological Society of America Bulletin*, 88, 1813-1827.

Rudels, B., Anderson, L.G., Jones, E.P. 1996. Formation and evolution of the surface mixed layer and halocline of the Arctic Ocean. *Journal of geophysical research,* 101, 8807-8821.

Rudels, B., Fahrbach, E., Meincke, J., Budéus, G. & Eriksson, P. 2002. The East Greenland Current and its contribution to the Denmark Strait overflow. *ICES Journal of Marine Science,* 59, 1133-1154.

Sadatzki, H., et al. In press. Sea ice variability in the southern Norwegian Sea during glacial Dansgaard-Oeschger climate cycles. *Science Advances.*

S. Bates, pers. Com 2016 (personal communication)

Schiebel, R. & Hemleben, C. 2005. *Modern planktic foraminifera*. Paläontologische Zeitschrift*, 79, 135-148.*

Schneider, T., Bischoff, T., Haug, G.H. 2014. Migrations and dynamics of the intertropical convergence zone. *Nature,* 513, 45-53.

Schmittner, A., Brook, E.J., Ahn, J. 2007. Past States and Millennial Variability. *In:* Schmittner, A., Chiang, J.C.H., Hemming, S.R. (eds.) *Ocean Circulation: Mechanisms and Impacts- Past and Future Changes of Meridonal Overturning.* Washington D.C.: American Geophysical Union.

Schmittner, A., Galbraith, E.D. 2008. Glacial greenhouse-gas fluctuations controlled by ocean circulation changes. *Nature,* 456, 373-367.

Schmittner, A., Gruber, N., Mix, A.C., Key, R.M., Tagliabue, A., Westberry, T.K. 2013. Biology and air-sea gas exchange controls on the distribution of carbon isotope ratios ($\delta^{13}C$) in the ocean. *Biogeosciences*, 10, 5793-5816.

Schlitzer, R. 2018, Ocean Data View. https://odv.awi.de.

Schulz, H., von Rad, U.U., Erlenkeuser, H. 1998. Correlation between Arabian Sea and Greenland climate oscillations of the past 110,000 years, *Nature*, 393, 54 –57.

Seager, R., Battisti, D.S., Yin, J., Gordon, N., Naik, N., Clement, A.C., Cane, M.A. 2002. Is the Gulf Stream responsible for Europe's mild winters? *Quarterly Journal of the Royal Meteorological Society*, 128, 2563-2585.

Sebille, E., Scussolini, P., Durgadoo, J.V., Peeters, F.J., Biastoch, A., Weijer, W., Turney, C., Paris, C.B., Zahn, R. 2015. Ocean currents generate large footprints in marine paleoclimate proxies. *Nature Communications,* 6, 6521.

Sessford, E, G., Tisserand, A.A., Risebrobakken, B., Andersson, C., Dokken, T., Jansen, E. 2018. High resolution benthic Mg/Ca temperature record of the intermediate water in the Denmark Strait across D-O stadial-interstadial cycles. *Paleoceanography and Paleoclimatology*, doi: 10.1029/2018PA003370

Shackleton, N. 1967. Oxygen Isotope Analyses and Pleistocene Temperatures Re-assessed. *Nature*, 215, 15-17.

Shackleton, N. J. 1974. Attainment of isotopic equilibrium between ocean water and the benthonic foraminifera genus Uvigerina: isotopic changes in the ocean during the last glacial. *Colloques Internationaux du C.N.R.S.,* 219, 203-209.

Shaffer, G., Olsen, S.M., Bjerrum, C.J. 2004. Ocean subsurface warming as a mechanism for coupling Dansgaard- Oeschger climate cycles and ice-rafting events. *Geophysical Research Letters,* 31, L24202.

Sicre, M.A., Jacob, J., Ezat, U., Rousse, S., Kissel, C., Yiou, P., Eríksson, J., Knudsen, K.L., Jansen, E., Turon, J.L. 2008. Decadal variability of sea surface temperatures off North Iceland over the last 2000 years. Earth and Planetary Science Letters, 268, 137-142.

Siegenthaler, U., Heimann, M., Oeschger, H. 1980. ^{14}C Variations Caused by Changes in the Global Carbon Cycle. *Radiocarbon,* 22, 177-191.

Simstich, J., Sarnthein, M. & Erlenkeuser, H. 2003. Paired $\delta^{18}O$ signals of *Neogloboquadrina pachyderma (s)* and *Turborotalita quinqueloba* show thermal stratification structure in Nordic Seas. *Marine Micropaleontology,* 48, 107-125

Stocker, T.F., Johnsen, S.J. 2003. A minimum thermodynamic model for the bipolar seesaw. *Paleoceanography and Paleoclimatology,* 18, 1087.

Stuvier, M. 1961. Variations in Radiocarbon Concentrations and Sunspot Activity. *Journal of Geophysical Research*, 66, 273-276.

Stuvier, M., Quay, P.D. 1981. Atmospheric ^{14}C changes resulting from fossil fuel CO_2 release and cosmic ray flux variability. *Earth and Planetary Science Letters*, 53, 349-362.

Svensson, A., Andersen, K.K., Bigler, M., Clausen, H.B., Dahl-Jensen, D., Davies, S.M., Johnsen, S.J., Muscheler, R., Parrenin, F., Rasmussen, S.O., Röthlisberger, R., Seierstad, I., Steffensen, J.P., Vinther, B.M. 2008. A 60 000 year Greenland stratigraphic ice core chronology, *Climate of the Past*, 4, 47-57.

Swift, J.H., Aagaard, K. 1981. Seasonal transitions and water mass formation in the Iceland and Greenland seas. *Deep Sea Research Part A. Oceanographic Research Papers*, 28, 1107-1129.

Tanhua, T., Olsson, K.A., Jeansson, E. 2005. Formation of Denmark Strait overflow water and its hydro-chemical composition. *Journal of Marine Systems*, 57, 264-288.

Toggweiler, J.R., Samuels, B. 1993. New radiocarbon constraints on the upwelling of abyssal water to the ocean's surface. *In:* Heiman, M. (ed.) *The Global Carbon Cycle*. NATO ASI Series (Series 1: Global Environmental Change), 15, Berlin: Springer.

Urey, H. C. 1947. The thermodynamic properties of isotopic substances. *Journal of the Chemical Society*, 0, 562-581.

Vellinga, M., Wood, R.A. 2002. Global climatic impacts of a collapse of the Atlantic thermohaline circulation. Climatic Change, 54, 251-267.

Voelker, A. H. L., Sarnthein, M., Grootes, P.M., Erlenkeuser, H., Laj, C., Mazaud, A., Nadeau, M-J., Schleicher, M. 1998. Correlation of Marine 14C Ages from the Nordic Seas with the GISP2 Isotope Record: Implications for ^{14}C Calibration Beyond 25 ka BP, *Radiocarbon*, 40, 517-534.

Voelker, A. H.L., Grootes, P.M., Nadeau, M.J., Sarnthein, M. 2000. Radiocarbon levels in the Iceland Sea from 25-53 kyr and their link to the Earth's magnetic field intensity, *Radiocarbon*, 42, 437-452.

Voelker, A. H. L. 2002. Global distribution of centennial-scale records for Marine Isotope Stage (MIS) 3: A database. *Quaternary Science Reviews,* 21, 1185–1212.

Voelker, A. H. L., Haflidason, H. 2015. Refining the Icelandic tephrachronology of the last glacial period – The deep-sea core PS2644 record from the southern Greenland Sea*, Global and Planetary Change,* 131, 35-62.

Våge, K., Pickart, R.S., Spall, M.A., Moore, G.W.K., Valdimarsson, H., Torres, D.J., Erofeeva, S.Y., Nilsen, J.W.Ø. 2013. Revised circulation scheme north of the Denmark Strait. *Deep Sea Research Part 1: Oceanographic Research Papers,* 79, 20-39.

Våge, K., Papritz, L., Håvik, L., Spall, M.A., Moore, G.W.K. 2018. Ocean convection linked to the recent ice edge retreat along east Greenland. *Nature communications*, 9, 1287.

Wallmann, K., Aloisi, G. 2012. The global carbon cycle: geological processes. *In:* Knoll, A.H. (ed.) *Fundamentals of Geobiology*. Chichester, West Sussex: John Wiley & Sons.

Wary, M., Eynaud, F., Rossignol, L., Zaragosi, S., Sabine, M., Castera, M-H., Billy, I. 2017. The southern Norwegian Sea during the last 45 ka: hydrographical reorganizations under changing ice-sheet dynamics. *Journal of Quaternary Science,* 32, 908-922.

Waelbroeck, C., Labeyrie, L., Michel, E., Duplessy, J.C., McManus, J.F., Lambeck, K., Balbon, E., Labracherie, M. 2002. Sea-level and deep water temperature changes derived from benthic foraminifera isotopic records. *Quaternary Science Reviews,* 21, 295-305.

Wolff, E.W., Chappelaz, J., Blunier, T., Rasmussen, S.O, Svensson, A. 2010. Millennial-Scale variability during the last glacial: The ice core record. *Quaternary Science Reviews*, 29, 2828-2838.

Zhang, X., Knorr, G., Lohmann, G., Barker, S. 2017. Abrupt North Atlantic circulation changes in response to gradual CO_2 forcing in a glacial climate state. *Nature Geoscience*, 10, 518-523.

Østerhus, S., Turrell, W.R., Jónsson, S., Hansen, B. 2005. Measures volume, heat, and salt fluxes from the Atlantic to the Arctic Mediterranean. *Geophysical Research Letters*, 32, L07601.

Appendix

Appendix A

Cleaning Protocol for Mg/Ca analysis

Clean the tip of the pipette between every sample in 10% nitric acid (HNO_3) and rinse the tip in Milli-Q water to avoid cross contamination. Change tip regularly for the same reason.

Clay removal

Clay particles are removed by suspending them into a liquid that is subsequently removed by a pipette. Here, Milli-Q water is used before the same procedure is repeated with methanol. The lower viscosity of methanol enables further disaggregation of clay particles. Sample vials are put in an ultrasonification bath to further aid disaggregation of clay.

1. Water rinse:
    a. Add approximately 500 µl of Milli-Q water to vials containing the sample.
    b. Ultrasonicate for 1 minute.
    c. Tap and invert vials to center sample in the bottom of the vials.
    d. Remove overlying water that includes suspended clay particles by pipette.
    e. Repeat 5 times or more until there is no visible clay in suspension.
2. Methanol rinse
    a. Add 250 µl of trace select grade methanol:
    b. Ultrasonicate for 1 minute
    c. Tap and invert vials to center sample in the bottom of the vials.
    d. Remove overlying water that includes suspended clay particles by pipette.
    e. Repeat twice.
3. Water rinse to remove remaining methanol
    a. Add approximately 500 µl of Milli-Q water to vials containing the sample.
    b. Ultrasonicate for 1 minute.
    c. Tap and invert vials to center sample in the bottom of the vials.
    d. Remove overlying water that includes suspended clay particles by pipette.
    e. Remove as much water as possible.

Metal oxide removal (reductive step)

Ferro-manganese oxide coatings are removed by reduction in a solution of hydrazine-ammonium citrate.

The reducing solution is made by 10 ml ~25-35% Trace select grade ammonium hydroxide (NH_3), 10 ml of citric acid ammonia mixture and 750 µl analytical reagent grade hydrazine (N_2H_4). The citric acid ammonia mixture is composed of 25 g ACS reagent grade citric acid powder ($C_6H_8O_7$) dissolved in 500 ml of ~25-35% Trace select grade ammonium hydroxide.

Samples in the hydrazine-ammonium citrate solution is put in hot water to enhance reactions and subjected to an ultrasonification bath to stir reagent into contact with all sample and to avoid re-precipitation of dissolved oxides. The procedure is kept under a fume hood.

4. Reductive step:
    a. Add 100 µl of the hydrazine-ammonium citrate to each vial and cap lids tightly
    b. Place the rack with vials in a hot water bath (70-90°C) for 30 minutes.
    c. Ultrasonicate every two minutes.
    d. After 30 minutes, remove vials from the hot water bath and carefully remove reagent with pipette.
5. Water rinse to remove remaining reagent
    a. Fill vials and caps with ~500 µl Milli-Q water
    b. Tap and invert vials to remove bubbles and let sample settle in the bottom of the vial.
    c. Remove overlying water by pipette.
    d. Repeat steps a. to c. 3 times.

Organic matter removal (Oxidative step)

Organic matter oxidized by a solution of hydrogen peroxide (H_2O_2) and sodium hydroxide (NaOH) solution. The solution consists of 30 ml 0.1M chemical reagent grade carbonate free NaOH mixed with 100 µl 30% Ultrapur H_2O_2 solution. CO_2 is produced from the reaction and is let escape. Impurities are suspended and are removed with the solution after the treatment and during subsequent water rinses.

6. Oxidative step:
    a. Add 250 µl of oxidative agent to each vial
    b. Clamp an acrylic sheet over the lids in order to avoid for them to pop open during the reaction.
    c. Place the rack with the vials in a hot water bath (70-90°C) for 10 minutes.

   d. After 5 minutes, remove the rack from the hot water bath and firmly tapped against the table on all sides to remove gas bubble that keep sample from reagent and to settle all sample material in the bottom of the vials.
   e. After 10 minutes, tap vials gently to remove bubbles and to let sample settle.
   f. Centrifuge vials for 1.30 minutes at 10000 rpm.
   g. Remove reagent with pipette.
7. Water rinse:
   a. Fill vials and caps with ~500 µl Milli-Q water
   b. Tap and invert vials to remove bubbles and let sample settle in the bottom of the vial.
   c. Remove overlying water by pipette.
   d. Repeat steps a. to c. once.

Sample split

The samples are split to have one part of the sample prepared for barite removal and the other omitting this step to be ready for acid leaching. Samples that are prepared directly for acid leaching are put into clean acid leached vials. This is done to avoid contamination on the surfaces if the original vials that has been absorbed during the cleaning process (Boyle and Keigwin, 1985).

The splitting is performed by adding ~100 µl of Milli-Q water to the original vials that contain the full sample. Squirt water into the vial to suspend the sample and draw it into the pipette and transfer into the new vial. This procedure may have to be repeated several times to make sure that the split is uniform. Clean the tip three times in Milli-Q water and 10% HNO_3 between samples to avoid cross-contamination and change tip routinely.

Barite removal

A solution of diethylenetriaminepentaacetic acid (DTPA) or pentetic acid, $C_{14}H_{23}N_3O_{10}$, is used to remove barite contamination.

16 g of Organics reagent grade DTPA powder was dissolved in 200 Milli-Q water to make a 0.002M DTPA solution. 0.1M Chemical reagent grade carbonate free Sodium Hydroxide (NaOH) was added to the solution until the solution was pH-neutral as tested with indicator paper. DTPA dissolves $CaCO_3$ in addition to barite by chelating metal ions so this procedure must be performed with care. A neutral solution limits calcite dissolution. To further limit calcite dissolution, ammonium hydroxide is added to neutralize the solution directly after the reaction. Subsequently, contaminants and dissolved calcite is removed with the solution and rinsed with water.

8. Barite removal:
    a. Add 50 µl of DTPA solution to each vial.
    b. Place the rack with the vials in a hot water bath (70-90°C) for 10 minutes.
    c. Every two minutes:
        1. Tap and invert vials to remove bubbles and to keep reagent in contact with sample.
        2. Tap vials to let samples settle to the bottom of the vials.
    d. Immediately fill vials with 450 µl of 25-25% Suprapur reagent grade ammonium hydroxide to neutralize solution.
    e. Remove solution with pipette.
9. Water rinse:
    a. Fill vials with ~500 µl Milli-Q water.
    b. Tap and invert vials to remove bubbles and let sample settle in the bottom of the vial.
    c. Remove overlying water by pipette.
    d. Repeat steps a. to c. twice.

Sample transfer

Transfer the sample into new vials by the procedure described above before the acid leach.

Acid leach. (Dilute acid rinse)

Samples are finally treated with nitric acid (0.001M HNO_3) to remove remaining absorbed contaminants on the sample. This treatment may be very aggressive, and care must therefore be taken, and the procedure modified depending on sample size.

10. Acid leach:
    a. Add 250 µl 0.001M ultra-pure nitric acid to each vial.
    b. Tap to remove bubbles and to keep sample in contact with the acid.
    c. Ultrasonicate for 30 seconds.
    d. Remove acid by pipette.
11. Water rinse:
    a. Fill vials with ~500 µl Milli-Q water.
    b. Cap, tap and invert vials to remove bubbles and let sample settle in the bottom of the vial.
    c. Remove overlying water by pipette.

    d. Repeat steps a. to c. once.

Dissolution

Samples that have been subjected to the cleaning protocol are prepared for measurement. The samples are fully dissolved in 0.1M trace metal pure nitric acid (HNO_3). After dissolution, samples are centrifuged to aid removal of remaining particles that have been unaltered by the cleaning, i.e. silicates and sulfides. It is important to be careful in pipetting from this stage to ensure that dilutions are accurate. Elemental leaching may occur during dissolution if the samples dissolve slowly. Therefore, the samples are ultrasonicated to aid faster dissolution and the samples are routinely tapped to remove bubbles that keep the sample separated from the acid.

12. Dissolution:
    a. Add 350 µl of 0.1M HNO_3 to each vial.
    b. Ultrasonicate until samples are completely dissolved.
    c. Centrifuge the dissolved samples for 10 minutes at 10000 rpm.
    d. Transfer 300 µl of the solution to stock solution vials. Keep the pipette-tip away from the bottom of the vial to avoid residue particles in the stock solution.

Appendix B

Oxygen and carbon isotope measurements from the interval 285 cm to 340 cm.

Table B.1: Mean values of stable isotope measurements.

Average sample depth (cm)	**$^{18}O/^{16}O$ Mean**	**$^{13}C/^{12}C$ Mean**
0.25	3.50	0.28
0.75	3.53	0.26
285.25	4.69	0.16
285.75	4.64	0.30
286.25	4.52	0.30
286.75	4.74	0.21
287.25	4.58	0.07
287.75	4.31	0.15
288.25	4.29	0.16
288.75	4.18	0.06
289.25	4.13	0.02
289.75	4.12	0.00
290.25	4.01	-0.02
290.75	4.08	0.08
291.25	4.06	-0.05
291.75	3.95	-0.03
292.25	4.15	0.21
292.75	4.20	0.14
293.25	3.99	0.15
293.75	3.95	0.05
294.25	4.12	0.11
294.75	4.34	0.12
295.25	4.12	0.17
295.75	4.09	-0.01
296.25	4.10	0.06
296.75	3.92	0.04
297.25	4.00	-0.13
297.75	4.15	0.13
298.25	4.08	0.13
298.75	4.10	0.12
299.25	3.90	-0.09
299.75	3.94	0.00
300.25	3.83	-0.01
300.75	4.19	0.23
301.25	4.08	0.11
301.75	4.33	0.09
302.25	4.16	0.14
302.75	4.05	0.16
303.25	4.13	0.07

303.75	4.06	0.02
304.25	4.12	0.23
304.75	4.13	0.06
305.75	4.11	0.10
306.25	4.28	0.22
306.75	4.11	0.18
307.25	4.21	0.12
307.75	4.14	0.19
308.25	4.07	0.17
308.75	4.05	0.15
309.25	4.05	0.18
309.75	4.41	0.18
310.25	3.78	0.07
310.75	4.61	0.12
311.25	4.40	0.11
311.75	4.18	0.15
312.25	3.73	-0.01
312.75	3.98	0.06
313.25	3.84	0.11
313.75	3.88	0.19
314.25	3.82	0.11
314.75	3.59	0.09
315.25	3.38	-0.09
315.75	3.62	-0.11
316.25	3.32	-0.08
316.75	3.45	-0.04
317.25	3.05	-0.19
317.75	3.14	-0.18
318.25	3.24	-0.07
318.75	3.30	0.10
319.25	3.03	-0.02
319.75	3.14	-0.08
320.25	2.68	-0.09
322.75	3.15	-0.07
323.25	3.03	-0.03
323.75	3.63	0.05
324.25	3.56	0.07
324.75	3.53	-0.07
325.25	3.99	0.00
325.75	3.08	-0.06
326.25	3.05	-0.12
326.75	2.94	-0.10
327.25	3.49	0.08
327.75	3.68	0.08
328.25	3.82	0.15

328.75	4.20	0.22
329.25	5.42	0.09
329.75	4.59	0.03
330.25	4.17	0.13
330.75	4.27	0.25
331.25	4.30	0.08
331.75	4.38	0.22
332.25	5.25	0.23
332.75	4.40	0.34
333.25	4.36	0.21
333.75	4.52	0.16
334.25	4.99	0.10
334.75	4.53	0.26
335.25	4.15	0.13
335.75	4.33	0.19
336.25	4.01	0.10
336.75	3.86	0.09
337.25	3.98	0.03
337.75	4.08	-0.20
338.25	4.10	0.02
338.75	4.25	0.25
339.25	4.37	0.19
339.75	3.86	0.02

Appendix C

Element measurements.

Table C.1. Data after the “Cd-cleaning” method.

Lab ID	**Average depth (cm)**	**Ca conc.**	**Mg/Ca**	**Fe/Ca**	**Mn/Ca**	**Al/Ca**	**Ba/Ca**
TEL18-0259	0.75	39.033	0.842	0.015	0.004	0.539	0.090
TEL18-0086	285.25	38.557	0.525	0.046	0.041	0.838	0.001
TEL18-0139	285.75	40.917	0.635	0.117	0.034	0.865	0.004
TEL18-0087	286.25	40.776	0.416	0.036	0.022	0.626	0.001
TEL18-0140	286.75	40.614	0.512	0.151	0.026	0.882	0.001
TEL18-0088	287.25	38.181	0.430	0.045	0.008	0.625	0.002
TEL18-0141	287.75	39.543	0.606	0.215	0.032	1.209	0.001
TEL18-0089	288.25	41.677	0.447	0.039	0.044	0.280	0.001
TEL18-0142	288.75	42.680	0.514	0.083	0.082	0.792	0.001
TEL18-0090	289.25	42.525	0.528	0.042	0.123	0.455	0.001
TEL18-0143	289.75	40.658	0.591	0.079	0.145	0.832	0.001
TEL18-0091	290.25	40.879	0.579	0.035	0.141	0.470	0.003
TEL18-0144	290.75	41.057	0.750	0.094	0.152	0.887	0.001
TEL18-0092	291.25	40.595	0.566	0.042	0.147	0.516	0.002
TEL18-0145	291.75	41.815	0.516	0.066	0.123	0.729	0.001
TEL18-0093	292.25	40.146	0.495	0.251	0.103	0.288	0.001
TEL18-0146	292.75	40.708	0.575	0.098	0.106	0.850	0.001
TEL18-0094	293.25	43.103	0.488	0.052	0.089	0.466	0.001
TEL18-0147	293.75	39.940	0.558	0.077	0.074	0.949	0.003
TEL18-0095	294.25	41.030	0.491	0.032	0.097	0.430	0.001
TEL18-0148	294.75	42.711	0.571	0.094	0.075	0.838	0.002
TEL18-0096	295.25	38.801	0.541	0.251	0.078	0.461	0.001
TEL18-0149	295.75	42.300	0.508	0.065	0.079	0.781	0.022
TEL18-0097	296.25	38.861	0.500	2.286	0.077	0.443	0.001
TEL18-0150	296.75	40.969	0.486	0.064	0.052	0.831	0.029
TEL18-0098	297.25	42.304	0.419	0.016	0.055	0.492	0.001
TEL18-0151	297.75	42.064	0.557	0.065	0.101	0.723	0.001
TEL18-0099	298.25	38.477	0.761	0.097	0.073	0.703	0.012
TEL18-0152	298.75	44.726	0.567	0.056	0.110	0.695	0.013
TEL18-0100	299.25	41.611	0.582	0.030	0.110	0.422	0.003
TEL18-0153	299.75	43.082	0.591	0.112	0.131	0.785	0.002
TEL18-0101	300.25	40.283	0.520	0.031	0.105	0.454	0.002
TEL18-0154	300.75	42.279	0.623	0.092	0.121	0.831	0.012
TEL18-0102	301.25	41.339	0.492	0.024	0.109	0.450	0.002
TEL18-0155	301.75	46.296	0.518	0.060	0.099	0.392	0.002
TEL18-0103	302.25	41.278	0.543	0.024	0.089	0.496	0.002
TEL18-0156	302.75	39.326	0.550	0.155	0.082	0.813	0.005
TEL18-0104	303.25	40.093	0.539	0.044	0.069	0.505	0.002
TEL18-0105	304	39.837	0.498	0.038	0.061	0.426	0.002

TEL18-0157	304.75	38.622	0.536	0.060	0.040	0.782	0.002
TEL18-0158	305.75	38.810	0.551	0.088	0.029	0.762	0.002
TEL18-0106	306.25	42.707	0.446	0.022	0.024	0.456	0.007
TEL18-0159	306.75	36.153	0.477	0.059	0.016	0.815	0.002
TEL18-0107	307.25	40.605	0.522	0.052	0.017	0.798	0.010
TEL18-0160	307.75	37.015	0.687	0.086	0.017	0.893	0.004
TEL18-0108	308.25	39.201	0.520	0.069	0.010	0.433	0.003
TEL18-0109	309.25	39.252	0.643	0.073	0.006	0.452	0.003
TEL18-0161	309.75	37.548	0.602	0.079	0.027	0.894	0.001
TEL18-0110	310.25	40.752	0.560	0.061	0.006	0.560	0.002
TEL18-0162	310.75	36.988	0.512	0.068	0.031	0.844	0.705
TEL18-0111	311.25	38.222	0.628	0.068	0.034	0.577	0.002
TEL18-0163	311.75	37.210	0.549	0.076	0.015	0.834	0.002
TEL18-0112	312.25	40.752	0.562	0.054	0.013	0.554	0.002
TEL18-0164	312.75	36.668	0.527	0.079	0.017	0.844	0.001
TEL18-0113	313.25	38.695	0.970	0.094	0.024	0.681	0.001
TEL18-0165	313.75	37.306	0.573	0.055	0.019	0.867	0.002
TEL18-0114	314.25	39.187	0.630	0.075	0.047	0.550	0.001
TEL18-0166	314.75	39.193	0.530	0.063	0.049	0.815	0.001
TEL18-0115	315.25	38.662	0.591	0.055	0.052	0.465	0.001
TEL18-0167	315.75	37.517	0.593	0.072	0.092	0.867	0.001
TEL18-0116	316.25	39.190	0.633	0.040	0.121	0.461	0.004
TEL18-0168	316.75	40.980	0.689	0.083	0.140	0.819	0.001
TEL18-0117	317.25	39.924	0.842	0.957	0.133	0.574	0.003
TEL18-0169	317.75	39.140	0.731	0.073	0.152	0.860	0.001
TEL18-0118	318.25	38.859	0.939	0.078	0.155	0.622	0.001
TEL18-0170	318.75	39.688	0.691	0.079	0.174	0.853	0.025
TEL18-0119	319.25	37.723	0.742	0.070	0.136	0.501	0.082
TEL18-0171	319.75	39.015	0.707	0.085	0.184	0.917	0.004
TEL18-0120	320.25	39.575	0.684	0.076	0.149	0.512	0.001
TEL18-0172	322.75	38.242	0.617	0.069	0.137	0.866	0.001
TEL18-0121	323.25	41.589	0.601	0.058	0.133	0.505	0.001
TEL18-0173	323.75	38.814	0.637	0.072	0.149	0.525	0.000
TEL18-0122	324.25	40.258	0.609	0.114	0.140	0.515	0.001
TEL18-0174	324.75	39.750	0.615	0.060	0.139	0.503	0.004
TEL18-0123	325.25	40.535	0.685	0.064	0.137	1.898	0.001
TEL18-0175	325.75	37.135	0.741	0.072	0.152	0.521	0.001
TEL18-0124	326.25	40.195	0.639	0.038	0.147	0.782	0.001
TEL18-0176	326.75	39.366	0.644	0.072	0.152	0.241	0.000
TEL18-0125	327.25	39.196	0.695	0.090	0.152	0.549	0.001
TEL18-0177	327.75	40.372	0.578	0.054	0.138	0.465	0.000
TEL18-0126	328.25	38.214	0.598	0.084	0.139	0.430	0.001
TEL18-0221	328.75	39.071	0.616	0.041	0.131	0.429	0.002
TEL18-0127	329.25	40.567	0.795	0.077	0.292	0.442	0.001
TEL18-0222	329.75	39.514	0.600	0.064	0.172	0.452	0.001

TEL18-0128	330.25	41.739	0.617	0.053	0.125	0.488	0.001
TEL18-0223	330.75	40.724	0.659	0.118	0.162	0.672	0.020
TEL18-0129	331.25	37.878	0.719	0.044	0.093	0.470	0.001
TEL18-0224	331.75	45.601	0.621	0.055	0.163	0.462	0.224
TEL18-0130	332.25	40.844	0.692	0.064	0.350	0.448	0.002
TEL18-0225	332.75	39.684	0.667	0.082	0.240	0.533	0.226
TEL18-0131	333.25	39.421	0.701	0.064	0.295	0.438	0.001
TEL18-0226	333.75	40.721	0.656	0.058	0.189	0.391	0.000
TEL18-0132	334.25	39.781	0.593	0.075	0.170	0.678	0.004
TEL18-0227	334.75	39.218	0.594	0.047	0.155	0.430	0.009
TEL18-0133	335.25	42.598	0.566	0.060	0.080	0.594	0.000
TEL18-0228	335.75	40.595	0.561	0.053	0.113	0.453	0.005
TEL18-0134	336.25	42.418	0.486	0.042	0.068	0.656	0.000
TEL18-0229	336.75	40.382	0.471	0.044	0.053	0.389	0.000
TEL18-0135	337.25	44.742	0.523	0.046	0.058	0.664	0.001
TEL18-0230	337.75	42.280	0.621	0.052	0.070	0.416	0.000
TEL18-0136	338.25	45.107	0.491	0.053	0.070	0.665	0.000
TEL18-0231	338.75	40.479	0.476	0.041	0.041	0.410	0.000
TEL18-0137	339.25	48.955	0.519	0.063	0.061	0.647	0.001
TEL18-0232	339.75	38.723	0.590	0.044	0.029	0.473	0.102
TEL18-0138	340.25	39.899	0.478	0.054	0.047	0.711	0.002

Table C.2: Data after the “Full-Cleaning” method.

Lab ID	**Average depth (cm)**	**Ca conc.**	**Mg/Ca**	**Fe/Ca**	**Mn/Ca**	**Al/Ca**	**Ba/Ca**
TEL18-0233D	0.25	38.795	0.493	0.057	0.034	0.498	0.001
TEL18-0234D	0.75	38.632	0.686	0.050	0.020	0.573	0.017
TEL18-0086D	285.25	38.186	0.401	0.046	0.005	0.767	0.002
TEL18-0139D	285.75	38.119	0.522	0.202	0.038	0.568	0.001
TEL18-0087D	286.25	39.592	0.582	0.042	0.109	0.463	0.001
TEL18-0140D	286.75	40.328	0.636	0.048	0.126	0.587	0.007
TEL18-0088D	287.25	41.362	0.599	0.033	0.128	0.498	0.002
TEL18-0141D	287.75	38.952	0.600	0.040	0.090	0.537	0.001
TEL18-0089D	288.25	38.073	0.620	0.050	0.083	0.507	0.001
TEL18-0142D	288.75	39.406	0.538	0.023	0.082	0.433	0.006
TEL18-0090D	289.25	40.545	0.566	0.059	0.060	0.448	0.001
TEL18-0143D	289.75	38.581	0.557	0.043	0.056	0.515	0.001
TEL18-0091D	290.25	39.401	0.492	0.041	0.052	0.526	0.001
TEL18-0144D	290.75	38.711	0.614	0.033	0.100	0.440	0.003
TEL18-0092D	291.25	39.197	0.644	0.045	0.094	0.451	0.002
TEL18-0145D	291.75	40.192	0.573	0.049	0.095	0.405	0.002
TEL18-0093D	292.25	41.422	0.642	0.026	0.075	0.446	0.002
TEL18-0146D	292.75	40.155	0.581	0.028	0.063	0.400	0.002
TEL18-0094D	293.25	38.677	0.547	0.017	0.052	0.448	0.002
TEL18-0147D	293.75	39.014	0.501	0.019	0.018	0.469	0.001
TEL18-0095D	294.25	38.460	0.526	0.052	0.012	0.450	0.002
TEL18-0148D	294.75	39.111	0.517	0.027	0.007	0.566	0.005
TEL18-0096D	295.25	40.410	0.469	0.047	0.007	0.443	0.001
TEL18-0149D	295.75	38.463	0.554	0.145	0.011	0.647	0.002
TEL18-0097D	296.25	39.970	0.487	0.075	0.011	0.475	0.002
TEL18-0150D	296.75	39.939	0.552	0.061	0.018	0.507	0.001
TEL18-0098D	297.25	40.029	0.487	0.054	0.034	0.426	0.001
TEL18-0151D	297.75	41.229	0.563	0.051	0.045	0.453	0.002
TEL18-0099D	298.25	40.462	0.530	0.056	0.103	0.465	0.001
TEL18-0152D	298.75	38.015	0.599	0.059	0.122	0.468	0.001
TEL18-0100D	299.25	37.877	0.625	0.062	0.144	0.469	0.005
TEL18-0153D	299.75	39.112	0.633	0.070	0.148	0.317	0.025
TEL18-0101D	300.25	40.284	0.575	0.074	0.131	0.485	0.001
TEL18-0154D	300.75	40.849	0.544	0.057	0.126	0.441	0.001
TEL18-0102D	301.25	41.826	0.569	0.058	0.124	0.418	0.001
TEL18-0155D	301.75	43.365	0.622	0.062	0.131	0.459	0.001
TEL18-0103D	302.25	42.674	0.589	0.062	0.145	0.420	0.001
TEL18-0156D	302.75	43.258	0.575	0.059	0.131	0.432	0.001
TEL18-0104D	303.25	39.864	0.669	0.035	0.253	0.496	0.001
TEL18-0105D	304	40.396	0.533	0.024	0.117	0.510	0.003
TEL18-0157D	304.75	38.641	0.662	0.141	0.320	0.662	0.003
TEL18-0158D	305.75	40.446	0.576	0.024	0.230	0.521	0.001
TEL18-0106D	306.25	38.088	0.553	0.049	0.166	0.506	0.010

TEL18-0159D	306.75	37.592	0.529	0.045	0.076	0.419	0.020
TEL18-0107D	307.25	36.396	0.461	0.174	0.059	0.439	0.002
TEL18-0160D	307.75	37.376	0.407	0.035	0.045	0.449	0.083
TEL18-0108D	308.25	37.819	0.492	0.035	0.054	0.367	-0.001
TEL18-0109D	309.25	38.213	0.465	0.039	0.051	0.451	0.000
TEL18-0161D	309.75	38.763	0.469	0.032	0.042	0.497	0.001
TEL18-0110D	310.25	37.767	0.388	0.072	0.025	0.498	0.000
TEL18-0162D	310.75	36.611	0.432	0.065	0.018	0.674	0.008
TEL18-0111D	311.25	38.451	0.511	0.062	0.014	0.631	0.000
TEL18-0163D	311.75	39.233	0.510	0.057	0.071	0.491	0.063
TEL18-0112D	312.25	39.495	0.586	0.071	0.124	0.387	0.000
TEL18-0164D	312.75	42.515	0.609	0.040	0.138	0.439	0.005
TEL18-0113D	313.25	40.122	0.483	0.056	0.110	0.553	0.009
TEL18-0165D	313.75	41.661	0.480	0.048	0.094	0.484	0.011
TEL18-0114D	314.25	39.209	0.439	0.082	0.065	0.450	0.000
TEL18-0166D	314.75	40.481	0.471	0.050	0.062	0.425	0.001
TEL18-0115D	315.25	38.721	0.442	0.047	0.065	0.409	0.000
TEL18-0167D	315.75	40.759	0.465	0.050	0.041	0.418	0.000
TEL18-0116D	316.25	38.884	0.492	0.047	0.091	0.417	0.000
TEL18-0168D	316.75	39.255	0.537	0.058	0.103	0.445	0.001
TEL18-0117D	317.25	42.595	0.547	0.052	0.117	0.404	0.001
TEL18-0169D	317.75	41.560	0.522	0.056	0.107	0.431	0.000
TEL18-0118D	318.25	39.122	0.542	0.042	0.091	0.153	0.002
TEL18-0170D	318.75	39.563	0.491	0.049	0.073	0.434	0.019
TEL18-0119D	319.25	39.467	0.513	0.050	0.033	0.398	0.192
TEL18-0171D	319.75	39.455	0.513	0.030	0.024	0.418	0.011
TEL18-0120D	320.25	38.654	0.462	0.064	0.013	0.587	0.099
TEL18-0172D	322.75	38.031	0.449	0.029	0.013	0.425	0.000
TEL18-0121D	323.25	38.455	0.503	0.047	0.020	0.413	0.001
TEL18-0173D	323.75	37.011	0.466	0.056	0.021	0.575	0.001
TEL18-0122D	324.25	37.706	0.405	0.034	0.009	0.423	0.080
TEL18-0174D	324.75	36.679	0.596	0.054	0.014	0.518	0.000
TEL18-0123D	325.25	37.372	0.528	0.035	0.018	0.443	0.001
TEL18-0175D	325.75	39.200	0.442	0.033	0.038	0.422	0.001
TEL18-0124D	326.25	40.496	0.545	0.056	0.077	0.220	0.000
TEL18-0176D	326.75	37.807	0.633	0.066	0.121	0.408	0.001
TEL18-0125D	327.25	37.923	0.635	0.061	0.130	0.492	0.001
TEL18-0177D	327.75	37.545	0.734	0.069	0.167	0.529	0.005
TEL18-0126D	328.25	38.694	0.608	0.054	0.160	0.403	0.000
TEL18-0221D	328.75	39.454	0.561	0.055	0.133	0.226	0.260
TEL18-0127D	329.25	41.600	0.585	0.057	0.131	0.460	0.000
TEL18-0222D	329.75	40.784	0.582	0.053	0.130	0.432	0.227
TEL18-0128D	330.25	40.241	0.616	0.066	0.133	0.429	0.610
TEL18-0223D	330.75	38.679	0.720	0.064	0.140	0.433	0.106
TEL18-0129D	331.25	39.577	0.614	0.058	0.132	0.466	0.021

TEL18-0224D	331.75	38.459	0.482	0.030	0.113	0.356	0.247
TEL18-0130D	332.25	39.331	0.526	0.033	0.155	0.383	0.001
TEL18-0225D	332.75	39.234	0.520	0.032	0.141	0.416	0.347
TEL18-0131D	333.25	38.567	0.560	0.031	0.147	0.359	0.002
TEL18-0226D	333.75	42.425	0.586	0.037	0.216	0.381	0.271
TEL18-0132D	334.25	40.351	0.660	0.035	0.175	0.359	0.008
TEL18-0227D	334.75	41.914	0.529	0.034	0.125	0.354	0.011
TEL18-0133D	335.25	40.528	0.454	0.029	0.104	0.367	0.129
TEL18-0228D	335.75	40.140	0.445	0.041	0.048	0.398	0.014
TEL18-0134D	336.25	39.634	0.466	0.035	0.054	0.392	0.032
TEL18-0229D	336.75	39.997	0.405	0.034	0.034	0.373	0.002
TEL18-0135D	337.25	39.050	0.434	0.021	0.026	0.447	0.009
TEL18-0230D	337.75	37.594	0.692	0.024	0.004	0.395	0.005
TEL18-0136D	338.25	36.972	0.773	0.159	0.007	0.528	0.038
TEL18-0231D	338.75	40.321	0.491	0.029	0.065	0.407	0.034
TEL18-0137D	339.25	37.359	0.508	0.060	0.006	0.442	0.000
TEL18-0232D	339.75	38.780	0.573	0.040	0.123	0.383	0.061
TEL18-0138D	340.25	40.438	0.509	0.029	0.081	0.356	0.864

Table C3: Replicated samples.

Lab ID	Average depth (cm)	Ca conc.	Mg/Ca	Fe/Ca	Mn/Ca	Al/Ca	Ba/Ca
TEL18-0259D	0.75	40.307	0.869	0.024	0.004	0.539	0.090
TEL18-0237	290.75	43.797	0.615	0.036	0.122	0.639	0.001
TEL18-0238	297.75	42.904	0.581	0.024	0.069	0.593	0.007
TEL18-0239	298.25	43.206	0.612	0.028	0.081	0.617	0.002
TEL18-0240	313.25	39.883	0.773	0.069	0.010	0.786	0.003
TEL18-0241	317.25	43.983	0.633	0.020	0.107	0.503	0.002
TEL18-0242	318.25	43.666	0.589	0.019	0.143	0.444	0.001
TEL18-0243	329.25	40.059	0.827	0.027	0.245	0.454	0.123
TEL18-0244	337.75	38.584	0.470	0.019	0.026	0.614	0.762
TEL18-0245D	292.25	39.034	0.535	0.022	0.058	0.505	0.558
TEL18-0246D	293.25	39.148	0.442	0.025	0.054	0.511	0.002
TEL18-0247D	295.25	40.350	0.435	0.041	0.041	0.224	0.001
TEL18-0248D	296.25	40.569	0.568	0.091	0.026	0.286	0.004
TEL18-0249D	300.25	40.896	0.508	0.017	0.091	0.432	0.022
TEL18-0250D	326.75	39.814	0.567	0.033	0.112	0.418	0.101
TEL18-0251D	329.25	40.604	0.670	0.017	0.237	0.424	0.002
TEL18-0252D	332.25	40.471	0.730	0.048	0.312	0.442	0.029
TEL18-0253D	333.75	40.848	0.481	0.014	0.120	0.379	0.001
TEL18-0254D	338.25	40.763	0.456	0.011	0.030	0.445	0.001
TEL18-0255D	338.75	39.966	0.468	0.012	0.015	0.500	0.072
TEL18-0256D	311.75	39.628	0.598	0.050	0.008	0.650	0.002